A Study of Pion Photoproduction on Helium-4 in the Delta Resonance Region Using Polarised and Unpolarised Photons.

Thesis

Submitted by

Jason F. Arneil

for the degree of

Doctor of Philosophy

Department of Physics and Astronomy
University of Edinburgh
1998

Abstract

Measurements of the $(\gamma, \pi^+ n)$ reaction on a ^{4}He target have been carried out using both unpolarised and polarised photons. This work is the latest in a series of experiments conducted by the Edinburgh University Nuclear Physics group in collaboration with the Universities of Glasgow and Tübingen. The experiment was carried out using the 855 MeV MAMI-B electron accelerator at the Institut für Kernphysik, Mainz, between March and August of 1996.

The 855 MeV electrons from the accelerator were directed either, on to a 4 μm Nickel foil to produce unpolarised photons or on to a 0.1 mm Diamond to produce polarised photons. These photons were then tagged with a resolution of 2 MeV using a spectrometer. The photons then impinged on a ^{4}He cryotarget.

Two sets of detectors were used to detect the reaction products. PiP, a plastic scintillator hodoscope, was used to detect the positive pions; and TOF a time-of-flight array, was used to detect the neutrons. Data was analysed for unpolarised photon energy regions centred at E_γ=260,300,340 and 380 MeV and two polarised regions centred at E_γ=258 and 338 MeV. PiP provided a pion angular coverage of $50° \leq \theta_\pi \leq 130°$, $-23° \leq \phi_\pi \leq 23°$ with an energy acceptance of E_π=20-180 MeV. The TOF array covered an angular range of $10° \leq \theta_n \leq 150°$, $160° \leq \phi_n \leq 200°$ with an energy threshold E_n^{min}=15 MeV. The overall missing energy resolution of the experiment was $\sim$10 MeV.

The unpolarised data is presented as double and triple differential cross sections while the polarised data is presented as photon asymmetries of the corresponding double differential cross section. A comparison is made with Plane Wave Impulse Approximation (PWIA) calculations by Louis Wright, both with and without final state interaction corrections. It is concluded that for the unpolarised data a more sophisticated treatment of the final state interactions is required while for the polarised data reasonable agreement is found between experiment and theory.

Acknowledgements

I would like to thank all members of the Edinburgh Nuclear Physics group who have provided help and encouragement over the last three years. I am grateful to my supervisor Derek Branford for his guidance and eternal optimisim. I am also indebted to my second supervisor Alan Shotter and Phil Woods who both provided my initial spark of enthusiam for nuclear physics. A really special thanks must also go to John MacKenzie in whose footsteps I have been fortunate enough to walk part of the way in. Cheers also to Steven Morrow for proofreading the thesis and to William Bradfield-Smith for being an amusing distraction. The experiments have been performed by a large collaboration too numerous to mention but cheers to everyone at Glasgow & Tübingen for all the help and the many shared nightshifts!

" I have yet to see any problem, however complicated, which when you looked at it in the right way did not become still more complicated."

-Paul Anderson

Contents

List of Figures

Chapter 1

Introduction

1.1 Overview

It has long been stated that the physics of the 20th century has been primarily concerned with the quantal structure of matter [Sha74]. Each system, whether an atom, a nucleus or a hadron, studied by physicists has exhibited the same properties, a ground state and a spectrum of excited states that are specified by a set of internal quantum numbers and their energy.

In nuclear physics the shell model in which protons and neutrons move independently in a mean field potential accounts well for many nuclear properties and reactions. There does however appear to be an inherent contradiction in the shell model. How can nucleons that interact via the strong nuclear force behave independently? The answer to this dilemma was found to lie in both the short range nature of the nucleon-nucleon interaction and the Pauli exclusion principle, which reduces the amount of states nucleons can scatter into.

In parallel to the pragmatic approach of the shell model are microscopic theories of the nucleus. These are based on the direct application of the nucleon-nucleon potential to the many body Schrödinger equation. Because microscopic theories include mesonic degrees of freedom and the fact that various coupling constants, form factors and propagators are used as inputs they can help in explaining the underlying dynamics of nuclear properties.

It is in all of this that intermediate energy photonuclear reactions have a role to

play. It has been shown that the explicit inclusion of meson exchange currents is required to describe adequately some photonuclear reactions. Another important factor in intermediate energy photonuclear reactions is the role of the Δ (1232) resonance which again can only be answered through microscopic theories.

Integral to this is nuclear pion photoproduction. It incorporates three basic fields of research: the elementary production mechanism on a nucleon, the underlying dynamics and the pion-nucleus interaction. Thus by fully understanding the free pion photoproduction case and by being able to describe the interactions that the produced particles undergo upon leaving a nucleus, it should be possible to gain an understanding into medium modifications and in particular how the Δ may be modified inside the nuclear environment.

The remainder of this chapter reviews the previous experimental work in this field.

1.2 Previous Data

The inclusive A (γ, π^+) B pion photoproduction reaction, where B is in a well defined state and no nucleon emission has occured, has been studied extensively over the past decade. These reactions are very sensitive to the nuclear transition structure of the target nuclei which tends to obscure the underlying dynamics of the photoproduction process. For a full discussion of this area see [Nag91].

In the exclusive A $(\gamma, \pi^+ \mathrm{n})$ B case where at least one nucleon is emitted in addition to the pion, this sensitivity to the nuclear structure diminishes and generally what is being probed is the modification of the free pion production process inside the nuclear medium. There have been fewer experiments done in this area. Prior to the previous experiments done by the PiPTOF collaboration at Mainz in 1993, the data tended to suffer from low resolution or restricted kinematics. A brief review of the previous experiments now follows.

1.2.1 The Bonn Data

The 500 MeV Bonn synchrotron was used by Arends *et al.* to perform pion photoproduction experiments on numerous nuclei [Are82, Are91]. The photons covered an energy range from 225 to 450 MeV and were tagged with a resolution of 10 MeV. The hadronic detection system consisted of two components, a magnetic spectrometer ($\Delta\,\Omega$ =63msr) which recorded data for positive and negative pions, and a scintillation counter arrangement for the detection of coincident charged or neutral particles. The data were presented as various double differential cross sections and compared to results obtained using PIKI an intranuclear cascade monte carlo calculation, which assumes the pion production process is a quasi-free reaction followed by final state interactions. As shown in figure 1.1 a reasonable agreement was obtained between the calculation and the experiment.

1.2.2 The MIT-Bates Data

The MIT-Bates experiment performed by Pham *et al.* made $(\gamma, \pi^- \mathrm{p})$ measurements on an ^{16}O target [Pha92]. The experiment used a bremsstrahlung photon beam with an end point energy of E_γ =360 MeV. Pions were detected in the 5.1msr

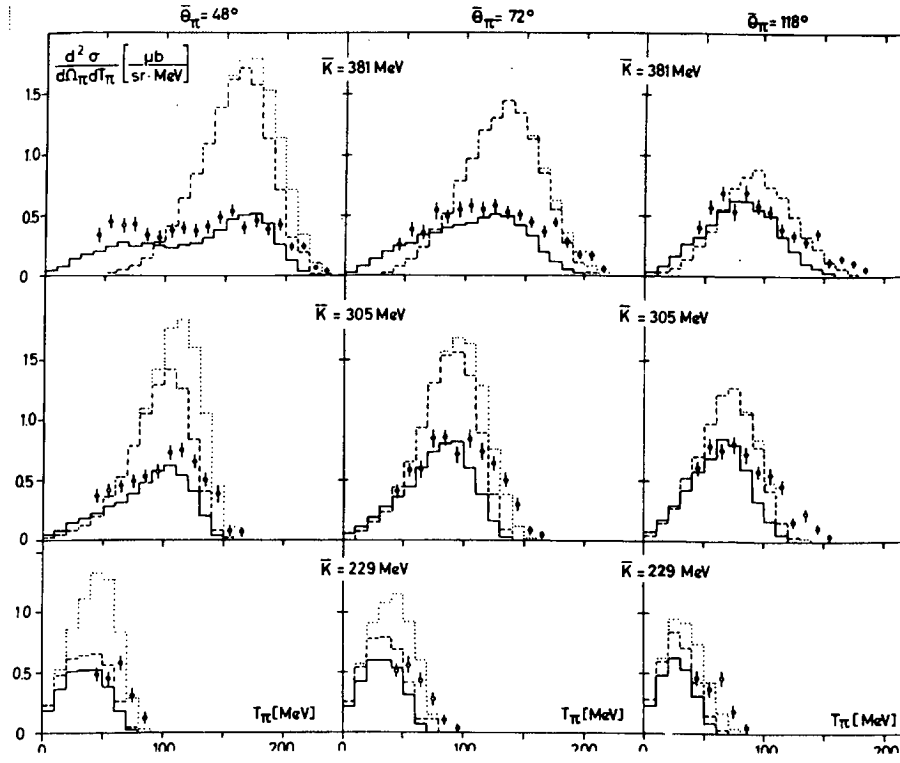

Figure 1.1: *A selection of Bonn data compared with the PIKI code (solid line)*

Bigbite magnetic spectrometer, which was positioned at two pion detection angles $\theta_\pi = 64°$ and $120°$. Protons were detected by an array of plastic scintillators which measured the proton energy and out of plane angle, these were placed at two angular settings of θ_p =40° and 20° respectively. The resolution of the system was sufficient enough to allow reactions to the ground state and the 6.2 MeV state in ^{15}O to be resolved. The data was presented as double differential cross sections $\frac{d^2\sigma}{d\Omega_\pi d\Omega_p}$ as a function of out-of-plane proton angle. Despite the cross sections being integrated over pion and proton energies, the data still has low statistics. The data also suffers due to complexities in the bremsstrahlung beam. The data is shown in figure 1.2, where it is compared to calculations made using the Distorted Wave Impulse Approximation (DWIA) code of Li, Wright & Benhold (LWB) [Li93]. The interesting feature is that the reduction in strength of the cross section at forward angles requires a reduction in the Δ mass to make the DWIA calculation agree at both forward and backward angles.

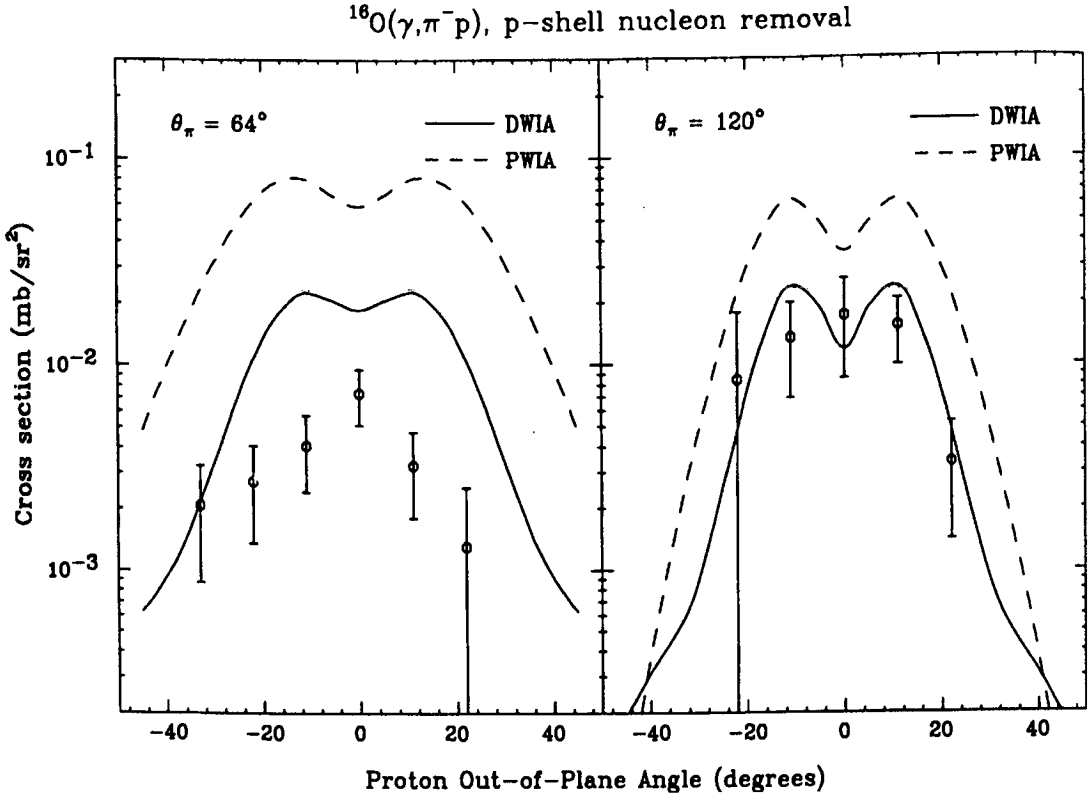

Figure 1.2: *Comparison of MIT-Bates and DWIA calculation*

1.2.3 The Tomsk Data

A higher quality data set than that previously mentioned was published by Glavanokov *et al.* [Gla79a, Gla79b, Gla89, Ana90]. They used the bremsstrahlung photon beam produced at the Tomsk electron synchrotron with three end point energies of E_γ = 350,370 and 390 MeV. An exclusive (γ, π^-p) measurement on Carbon-12 was carried out. The coincident pions and protons were detected using a double-arm spectrometer set-up. The pion energies were determined by measuring their range in a copper absorber and proton energies by time of flight measurements. The pion energy acceptance was 40-180 MeV while the proton acceptance was 50-190 MeV. The experiment was performed at one pion angle of 120° and a proton angle of 20° . Both detectors were in the reaction plane. The data was presented as triple differential cross sections $\frac{d^3\sigma}{dT_p d\Omega_\pi d\Omega_p}$ as a function of proton energy. The data was split into two sets corresponding to residual nucleus excitation energy, corresponding to removal from the $p_{3/2}$ and the $s_{1/2}$ shells. The

data has been compared favourably to calculations made by LWB as shown in figure 1.3. In particular while the PWIA calculation considerably overestimates the data the non-local DWIA gives a relatively good fit to the data, although some problems remain with the $s_{1/2}$ shell.

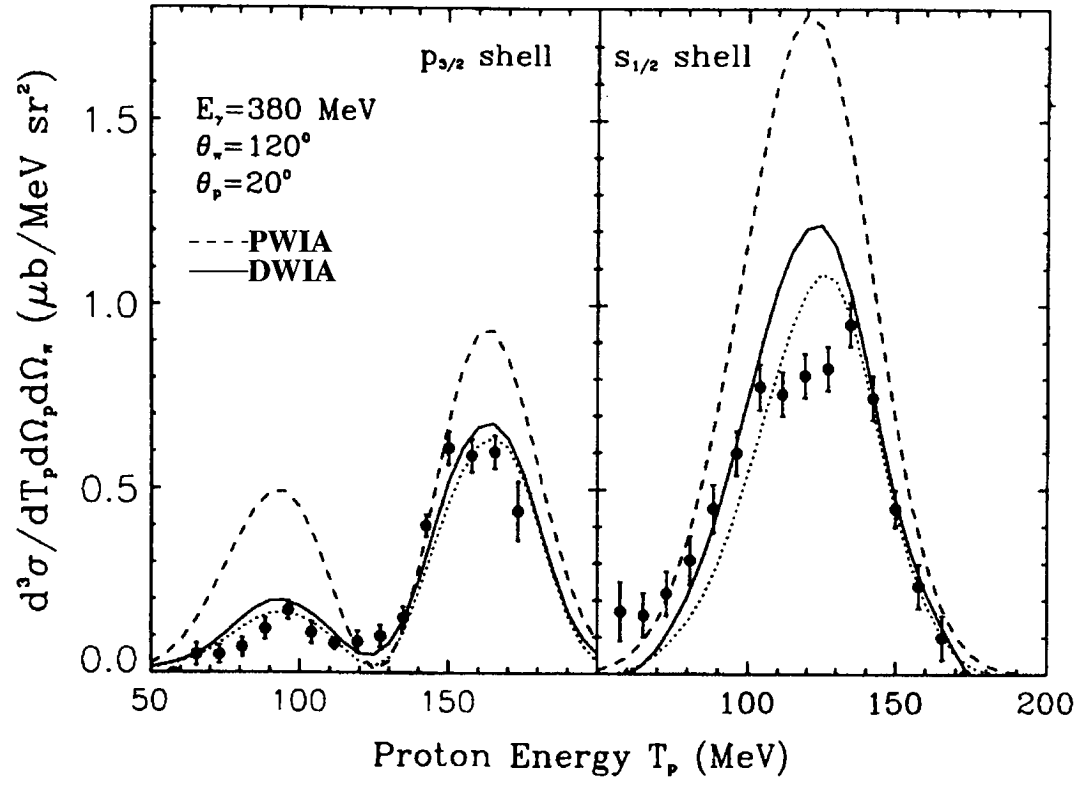

Figure 1.3: *Comparison of Tomsk data and DWIA calculation (solid line)*

1.2.4 1993 Edinburgh Data

This was a previous set of experiments performed by the PiPTOF collaboration at Mainz. The setup was similar to the present experiment and has the same extensive coverage of both photon energy and angular range. The resolution is also of similar size. This enabled an extensive survey to be undertaken of both $(\gamma, \pi^+ \mathrm{n})$ and $(\gamma, \pi^+ \mathrm{p})$ exclusive reactions on several nuclei including ^{6}Li, ^{12}C, and ^{40}Ca over a large region of phase space. The results were presented as double differential cross sections against neutron angle and triple differential cross sections

plotted against pion energy [Mac95, Mac96a, Joh95]. The data has been compared with a DWIA calculation generated by the code THREEDEE [Cha77] as in figure 1.4 and with the microscopic theory of Carrasco [Car92a, Car92b, Car92c, Car94]. It has also recently compared favourably to a DWIA calculation by LWB.

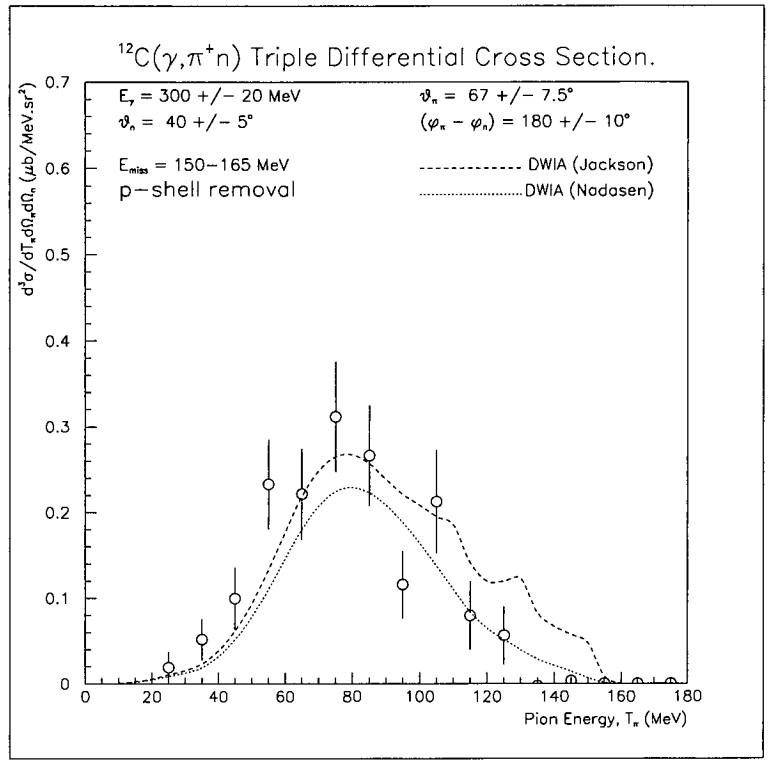

Figure 1.4: *Comparison of 1993 Edinburgh data and THREEDEE calculation*

1.2.5 The LEGS Data

This was the first pion photoproduction photon asymmetry on a nucleus to be published. It was performed by Hicks *et al.* [Hic97] The reaction $^{16}O(\vec{\gamma}, p\pi^-)$ was measured at the Laser Electron Gamma Source (LEGS) located at the Brookhaven National Laboratory. Linearly polarised photons between 210 and 330 MeV were produced by backscattering ultraviolet light from 2.6 GeV electrons. The photon energy was tagged with a resolution of 5 MeV. Pions were detected in CsI detectors at angles of 35° to 135° in steps of 20° , except at 95° where several thick plastic scintillators were used. Protons were detected in two layers of plastic scintillator

bars at in-plane angles of 20° to 140° in 8° steps. The data was presented as a photon asymmetry as a function of proton angle at the photon energy $E_\gamma = 293 \pm 20$ MeV and at various pion angles, it is compared with PWIA calculations by LWB, see figure 1.5

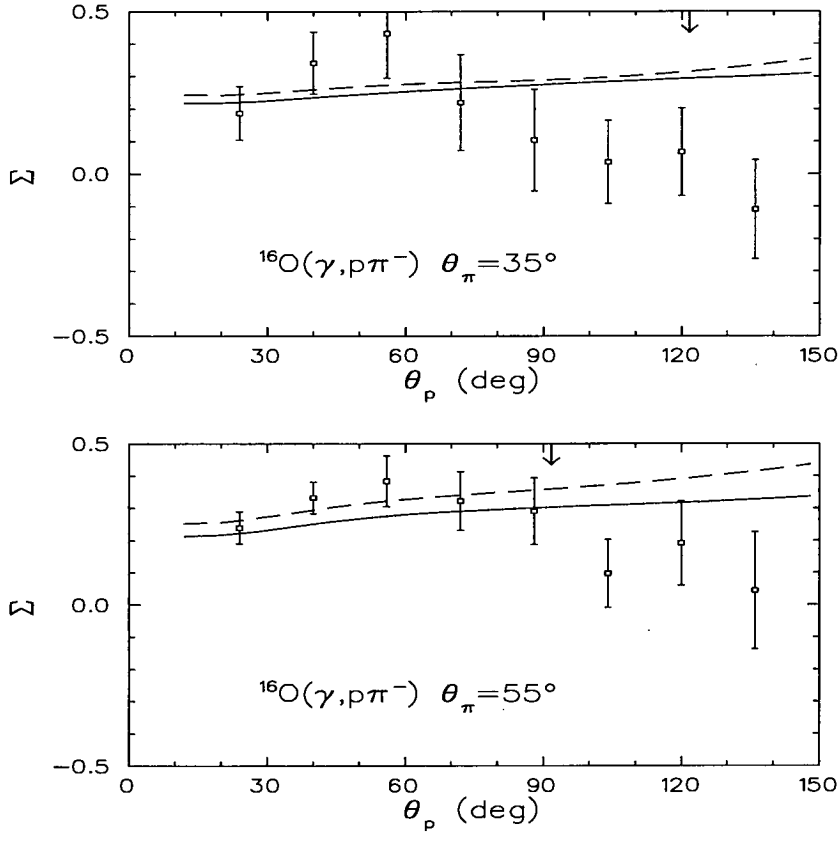

Figure 1.5: *Comparison of Legs data and PWIA calculation*

1.2.6 Present Experiment

The present experiment constitutes a natural progression of the 1993 Edinburgh experiments. It offers a measurement of the ^{4}He$(\gamma, \pi^+ n)$ reaction over a wide region of phase space.Unpolarised photons in the range 150-800 MeV, tagged with a 2 MeV resolution allow a survey over the whole Δ resonance region. Polarised photons in two regions at $E_\gamma = 258 \pm 20$ MeV and $E_\gamma = 338 \pm 20$ MeV allow a determination of the photon asymmetry.

Chapter 2

Theoretical Framework

2.1 The Interaction of Photons with Nuclei

The electromagenetic interaction is well understood through Quantum Electrodynamics (QED), and as it is a relatively weak interaction, a photon beam is able to probe the entire nuclear volume. These properties make it an excellent probe of the nucleus. This is in sharp contrast to hadronic (protons,pions etc.) probes which interact through the less well understood strong interaction, and are prone to being absorbed on the nuclear surface [Koc84]. There is, of course, a downside to electromagnetic probes. Because the cross sections for photo-reactions are considerably smaller, to obtain good statistics in an experiment with them requires a longer counting time.

Shown in figure 2.1 is how the total photoabsorption cross section varies with photon energy. All nuclei with mass numbers ranging from 10 to more than 200 obey the same fundamental σ/A curve [Gaa91]. There are several different responses of the nuclear sytem to photoabsorption, depending on the photon energy involved. At low energies below particle emission threshold, are sharp resonances corresponding to the excitation of bound excited nuclear states. Above particle emission threshold at photon energies of around 10 to 30 MeV the dominant feature is the giant dipole resonance, which can be described as a collective nuclear mode. Increasing the energy into the so called intermediate energy region we are interested in, between 100 MeV $\leq E_\gamma \leq$ 1 GeV you can essentially probe single or

small clusters of nucleons. The Δ isobar excitation of the nucleon is responsible for the properties of the curve in the energy region between 200 and 400 MeV.

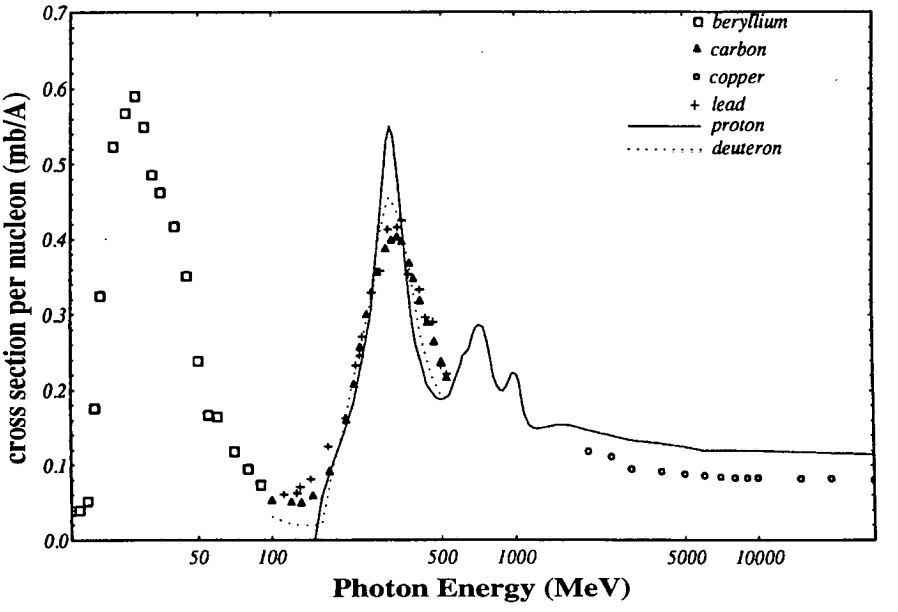

Figure 2.1: *Total photoabsorption cross section*

Due to the weakness of the interaction it is possible to use perturbation theory to describe the photoabsorption process. From Fermi's golden rule the transition rate from an initial state Ψ_i to a final state Ψ_f is given by [Mer70]:

$$w_{i\to f} = \frac{2\pi}{\hbar}|\langle\Psi_f|\mathcal{H}|\Psi_i\rangle|^2\rho_f \tag{2.1}$$

where ρ_f is the density of final states and $\mathcal{H}$ is the interaction operator:

$$\mathcal{H} = \int \vec{j}(\vec{r},t)\cdot\vec{A}(\vec{r},t)d\vec{r} \tag{2.2}$$

$\vec{A}(\vec{r},t)$ is the electromagnetic potential operator while $\vec{j}(\vec{r},t)$ is the transition current. As initial state Ψ_i and final state Ψ_f can both involve nucleons, mesons and resonances, so the transition current can be written in terms of a sum involving these:

$$J = J^{nucleons} + J^{mesons} + J^{resonances} \tag{2.3}$$

Thus photoabsorption experiments can be used to gain an understanding of the nuclear current and the associated underlying nuclear dynamics.

It is common to replace the current operator J with an effective operator J^{eff} which is defined in the subspace of the nucleons only [Gar81]. This enables the effective operator to be written in terms of a sum of one-body, two-body, etc. terms:

$$J^{eff} = J^{eff}_{one-body} + J^{eff}_{two-body} + \cdots \tag{2.4}$$

Diagramatically the different contributions to the one-body and two-body interactions can be visualised as in figure 2.2. One body terms are processes whereby the photon interacts with a single nucleon with the rest of the nucleus acting as a spectator. The two body terms involve the photon being absorbed on a correlated pair of nucleons. Crucial in this is the role of meson exchange.

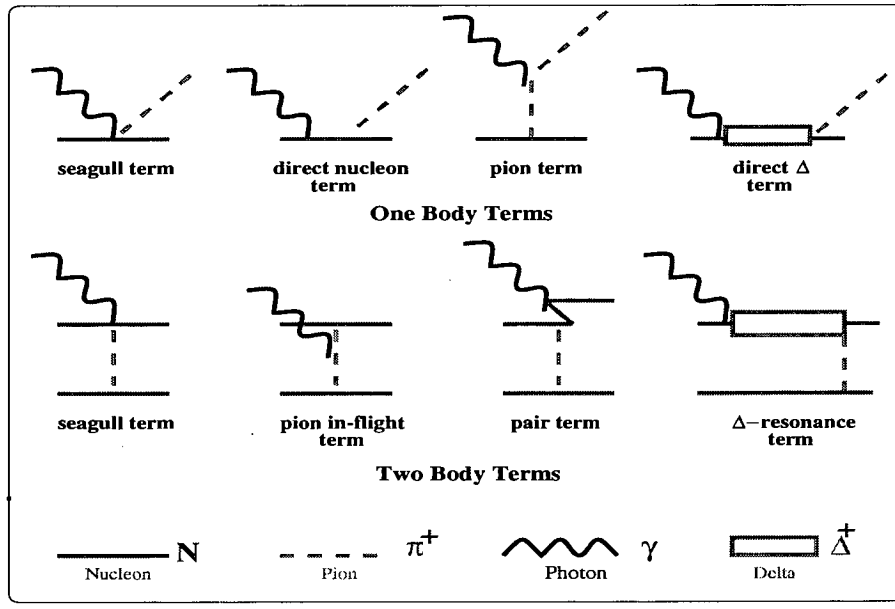

Figure 2.2: *One and two-body terms in photoabsorption*

In the Δ resonance region there is a large momentum mismatch between the photon and the nucleon. This causes a suppression in the one-body terms for nucleon knockout while, on the other hand, pion photoproduction suffers no such problem as the produced pion can take up the required momentum. This makes (γ,pN) and (γ, πN) excellent reactions for gaining information on the relative contributions of one and two-body mechanisms.

2.2 Free Pion Photoproduction

Before discussing pion photoproduction on a nucleus we must look at pion production on a nucleon. This gives us an understanding of the elementary process of meson production which will subsequently be embedded in the nuclear environment to study pion production on nuclei.

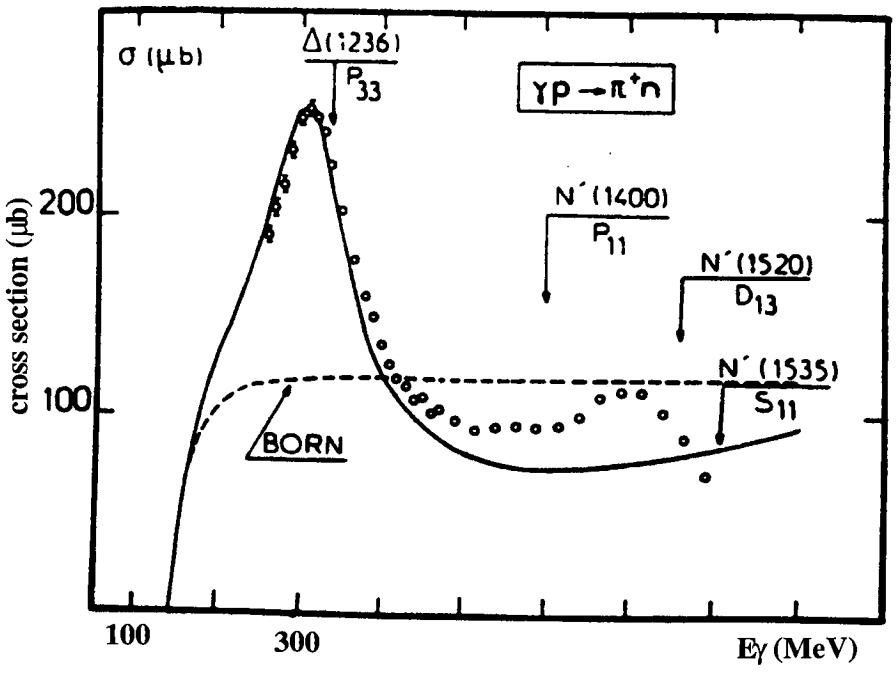

Figure 2.3: *Free charged Pion Photoproduction cross section*

The cross section for the reaction $(\gamma, \pi^+\mathrm{n})$ on the proton, as a function of photon energy, is shown in 2.3. It rises from threshold at the pion mass ($\sim$ 140 MeV) to a peak at the Δ resonance at $\mathrm{E}_\gamma \sim 330$ MeV. It then flattens out with other resonances being unresolved due to their large widths.

2.2.1 Kinematics

The kinematics of pion photoproduction are shown in 2.4. They are characterised by the four-momentum vectors $\mathrm{k}^\mu = (\mathrm{E}_\gamma, \overline{k})$ for the photon, $p_i^\mu = (\mathrm{E}_i, \overline{p}_i)$ for the initial nucleon, $q^\mu = (\mathrm{E}_\pi, \overline{p}_\pi)$ for the produced pion and $p_f^\mu = (\mathrm{E}_f, \overline{p}_f)$ for the final nucleon. The photon is also characterised by its polarisation state ε^μ.

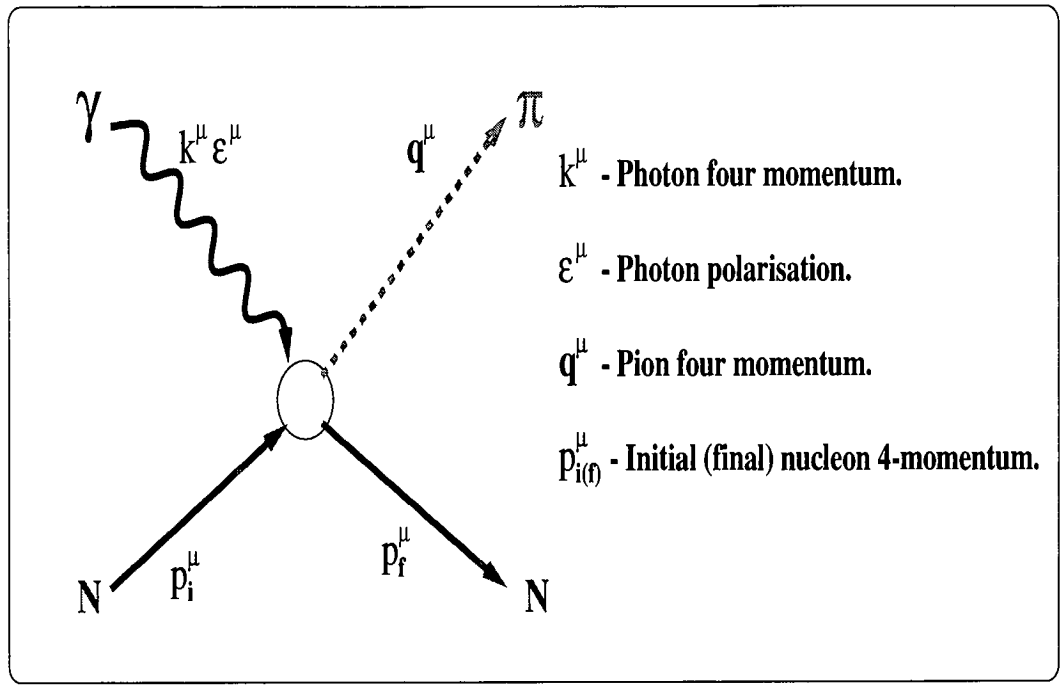

Figure 2.4: *Pion photoproduction kinematics*

These quantities are related by the following:

$$k^\mu + p_i^\mu = q^\mu + p_f^\mu \tag{2.5}$$

$$(p_i^\mu)^2 = (p_f^\mu)^2 = -m_N^2 \tag{2.6}$$

$$(q^\mu)^2 = -m_\pi^2 \tag{2.7}$$

$$(k^\mu)^2 = 0 \tag{2.8}$$

While the mandelstam variables [Byc73] are given by the following:

$$s = (k^\mu + p_i^\mu)^2 = (q^\mu + p_f^\mu)^2 \tag{2.9}$$

$$t = (q^\mu - k^\mu)^2 = (p_f^\mu - p_i^\mu)^2 \tag{2.10}$$

$$u = (p_i^\mu - q^\mu)^2 = (p_f^\mu - k^\mu)^2 \tag{2.11}$$

The S-matrix is defined as [Ber68]:

$$S_{fi} = \delta_{fi} - \frac{i}{(2\pi)^2}\delta^4(p_f^\mu + q^\mu - k^\mu - p_i^\mu)\sqrt{\frac{m_N^2}{4E_\gamma E_\pi E_i E_f}}T_{fi} \tag{2.12}$$

, where T_{fi} is the transition matrix element given by:

$$T_{fi} = \varepsilon^{\mu} \langle u_f(p_f)\pi(q)|J_{\mu}|u_i(p_i)\rangle \tag{2.13}$$

, with $u_i(p_i)$ and $u_f(p_f)$ representing the initial and final nucleon wavefunctions while $\pi(q)$ represents the produced pion's wavefunction.

The above leads to a derivation of the differential cross section in the centre of mass frame [Van95], where there is a sum over final spin states and an average over the initial spin states and also an average over photon polarisation states.

$$\left(\frac{d\sigma}{d\Omega_{\pi}}\right)_{cm} = \frac{1}{s}\frac{1}{(4\pi)^2}\frac{|\overline{p}_{\pi}|}{|\overline{k}|}E_i E_f \frac{1}{2}\sum_{s_i}\sum_{s_f}\frac{1}{2}\sum_{\lambda=\pm 1}|T_{fi}|^2 \tag{2.14}$$

The properties of pion photoproduction can then be deduced from an evaluation of the matrix elements T_{fi}. This matrix element can be separated into two separate parts. The first of these are known as the Born terms shown in 2.5 which are dominant at low energy and still provide 50% of the cross section for charged pion photoproduction in the Δ resonance region, while the other part involves the inclusion of resonant and multiparticle intermediate states, shown in 2.6. The most important of these non-Born contributions for $E_{\gamma} \leq 500$ MeV is the Δ resonance.

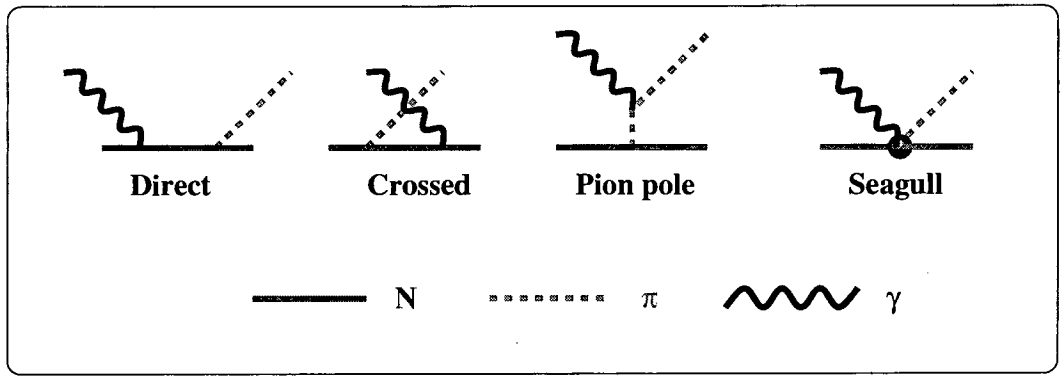

Figure 2.5: *Born terms in the free pion photoproduction amplitude*

There are essentially three main approaches and we now briefly discuss these.

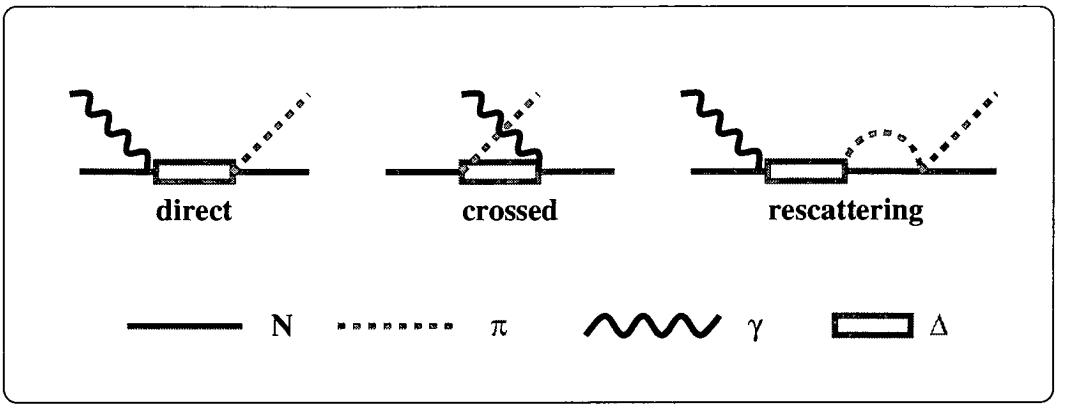

Figure 2.6: Δ *resonance terms in the free pion photoproduction amplitude*

2.2.2 Dispersion Relations

Of the various approaches used to study pion photoproduction the dispersion relations technique has by far the longest history. They were pioneered by Chew, Goldberger, Low and Nambu [Che57] (CGLN) and further developed by Berends *et al.* [Ber68]. This states that the most general form of the transition operator can be expressed as the following:

$$t_{fi} = \varepsilon^{\mu} J_{\mu}^{fi} \tag{2.15}$$

$$= \sum_{i} A_i M_i \tag{2.16}$$

This is a linear combination of the Lorentz invariant matrices M_i, which are formed from the particle four-momenta, the Dirac γ-matrices [Bjo64] and the photon polarisaton ε^{μ}. While the coefficients A_i can be written in terms of the mandelstam variables and the total center of mass energy.

CGLN were then able to perform a non-relativistic reduction in the barycentric frame to give the differential cross section in terms of:

$$\frac{d\sigma}{d\Omega} = \frac{q}{k} |\langle f|\mathcal{F}|i\rangle|^2 \tag{2.17}$$

, where the transition operator takes the form:

$$\mathcal{F} = i\sigma \cdot \hat{\epsilon} F_1 + \frac{\sigma \cdot q \sigma \cdot k \times \hat{\epsilon}}{|q||k|} F_2 + i \frac{\sigma \cdot k q \hat{\epsilon}}{|q||k|} F_3 + i \frac{\sigma \cdot q q \hat{\epsilon}}{q^2} F_4 \tag{2.18}$$

where $F_{1..4}$ are functions of photon energy and pion angle.

This angular dependence can be expressed in terms of Legendre polynomials thus expressing the amplitude as a multipole expansion,

$$F_1 = \sum_{l=0}^{\infty}[lM_{l+} + E_{l+}]P'_{l+1}(x) + [(l+1)M_{l-} + E_{l-}]P'_{l-1}(x) \quad (2.19)$$

$$F_2 = \sum_{l=1}^{\infty}[(l+1)M_{l+} + lM_{l-}]P'_l(x) \quad (2.20)$$

$$F_3 = \sum_{l=1}^{\infty}[E_{l+} - M_{l+}]P''_{l+1}(x) + [E_{l-} + M_{l-}]P''_{l-1}(x) \quad (2.21)$$

$$F_4 = \sum_{l=2}^{\infty}[M_{l+} - E_{l+} - M_{l-} - E_{l-}]P''_l(x) \quad (2.22)$$

where $x = cos(\theta_\pi)$ and P'_l represent derivatives of the Legendre polynomials.

The amplitude is now decomposed into a series of electric multipoles $E_{l\pm}$, and magnetic multipoles $M_{l\pm}$. The leading multipoles are given below in table 2.1 [Han97].

Multipole	l	J	radiation	remarks
E_{0+}	0	$\frac{1}{2}$	E1	threshold, S_{11} (1525)
E_{1+}	1	$\frac{3}{2}$	E2	P_{33} (1232)
M_{1+}	1	$\frac{3}{2}$	M1	P_{33} (1232)
M_{1-}	1	$\frac{1}{2}$	M1	P_{11} (1440)

Table 2.1: The leading multipoles for pion photoproduction.

The orbital angular momentum of the pion-nucleon system is l and the $\pm$ sign denotes whether the angular momentum and spin are parallel or antiparallel ($J = l \pm \frac{1}{2}$). The electromagnetic type of radiation is also given as well as the corresponding excited state of the nucleon.

Assuming causality, analyticity, unitarity and crossing symmetry it is possible, after a multipole projection to write a dispersion relation at fixed t as:

$$Re\mathcal{M}_l(W) = \mathcal{M}_l^P(W) + \frac{1}{\pi}\sum_{l'}\mathcal{P}\int_{thr}^{\infty} K_{ll'}(W,W')Im\mathcal{M}_{l'}(W')dW' \quad (2.23)$$

This is a system of integral equations coupled by the kernels $K_{ll'}$ which are known but complicated functions of the centre of mass system energy. Omnès [Omn58] cast the above equation in the form:

$$\begin{aligned} \mathcal{M}_l(W) &= \mathcal{M}_l^P(W) + \frac{1}{\pi}\int_{thr}^{\infty} \frac{h_l^*(W')\mathcal{M}_l(W')}{W' - W - i\varepsilon} dW' \\ &+ \frac{1}{\pi}\sum_{l'}\int_{thr}^{\infty} K_{ll'}(W, W')h_l^*(W')\mathcal{M}_l(W')dW' \end{aligned} \tag{2.24}$$

with:

$$\mathcal{M}_l = |\mathcal{M}_l|e^{i\Phi_l} \tag{2.25}$$

$$h_l = \sin\Phi_l e^{i\Phi_l} \tag{2.26}$$

Where $\mathcal{M}_l$ stands for any of the multipoles $E_{l\pm}$ or $M_{l\pm}$ and $\mathcal{M}_l^P$ denotes contributions from the Born terms. The first integral, known as the rescattering term, arises from intermediate two or more particle states in the s-channel while the second integral, known as the crossed term arises from intermediate two or more particle states in both the s and u channels.

The real and imaginary parts of the amplitudes are related by unitarity in the form of Watson's theorem [Wat54], which states that the phase of the multipole amplitude is that of pion scattering. Which is expressed as:

$$Im\mathcal{M}_l = Re\mathcal{M}_l \tan\delta_l \tag{2.27}$$

Where δ_l is the corresponding πN phase shift. All the observables including differential cross section $d\sigma/d\Omega$ and the photon asymmetry Σ can be defined in terms of these multipoles [Han97].

The dispersion relations approach works well in the case of free pion photoproduction, but runs into problems when applied to the case of nuclear pion photoproduction. Inside the nucleus the nucleons have Fermi motion and a frame invariant approach is generally required. However the multipoles are defined in the barycentric frame and these must be transformed into an invariant form. This transformation is mathmatically complex and leads to a loss of physical insight.

2.2.3 Effective Lagrangians

The second theoretical approach is the so called Effective Lagrangian method. Which involves explicitly evaluating the Feynman diagrams that include intermediate state particles, in particular the Δ , ρ and ω particles. This was first explored by Peccei [Pec69] and further developed by Olsson [Ols74]. The starting point is obtaining an effective Lagrangian that describes the interacting fields of the nucleon (ψ_N), delta (ψ^{μ}_{Δ}), pion (ϕ), ρ-meson (ρ^{μ}), ω-meson (ω^{μ}) and photon (A^{μ}).

The Lagrangian of the interaction is expressed as:

$$\mathcal{L}_{int} = \mathcal{L}_{PV} + \mathcal{L}_{\rho\omega} + \mathcal{L}_{\Delta} \tag{2.28}$$

The first term, $\mathcal{L}_{PV}$, describes the psuedo-vector coupling of the pion photoproduction mechanism, which is required by chiral symmetry and has the form:

$$\mathcal{L}_{PV} = \mathcal{L}_{\pi NN} + \mathcal{L}_{\gamma NN} + \mathcal{L}_{\gamma\pi\pi} + \mathcal{L}_{\gamma\pi NN} \tag{2.29}$$

The second term of equation (2.28), $\mathcal{L}_{\rho\omega}$, describes the interactions involving vector mesons. This involves the following:

$$\mathcal{L}_{\rho\omega} = \mathcal{L}_{\rho NN} + \mathcal{L}_{\omega NN} + \mathcal{L}_{\rho\pi\gamma} + \mathcal{L}_{\omega\pi\gamma} \tag{2.30}$$

The final term of equation (2.28), $\mathcal{L}_{\Delta}$, involves the Δ excitation and is given by:

$$\mathcal{L}_{\Delta} = \mathcal{L}_{\pi N\Delta} + \mathcal{L}_{\gamma N\Delta} \tag{2.31}$$

All the above terms can be written in terms of the interacting fields, the dirac γ matrices and the appropriate coupling constants, as an example the $\mathcal{L}_{\pi NN}$ has the form:

$$\mathcal{L}_{\pi NN} = -\frac{f_{\pi NN}}{m_{\pi}}\overline{\psi}_N(x)\gamma_5\gamma_{\mu}\tau\psi_N(x)\cdot\partial^{\mu}\phi(x) \tag{2.32}$$

, where $f_{\pi NN}$ is the coupling constant of the strong interaction, while τ is an isopin operator. The coupling constants, the Δ mass and width Γ are extracted from pion scattering data. Using these coupling constants the various Feynman diagrams can then be calculated and the cross section and other observables obtained.

Final state rescattering must still be accounted for by using Watson's theorem, i.e. each multipole must be given the correct phase as stated by πN scattering. This is complicated by the fact that each multipole may contain non-resonant (Born) terms and an explicit resonant part.

The effective Lagrangian approach can be said to have a less physical basis than the dispersion relations technique but does have the advantage of being easier to use in the extension to nuclear calculations.

2.2.4 The Hamiltonian Approach

The Hamiltonian approach, first pioneered by Nozawa *et al.* [Noz90], is the third of the pion photoproduction models we will look at. The model is similar to the effective Lagrangian approach in that the Δ is treated as an explicit degree of freedom to be added to the Hamiltonian of the process.

The interaction is expressed as a direct sum of the pion-nucleus scattering and the photon coupling subspaces. The complete Hilbert space is written as:

$$\mathcal{H} = S \oplus \gamma N \tag{2.33}$$

$$S = \sum_{B=N,\Delta} \pi N \oplus \Delta \tag{2.34}$$

$$\tag{2.35}$$

, where the subspace S describes the pion-nucleus scattering without coupling to photons, but does include Δ contributions.

The overall Hamiltonian is then a sum of the Hamiltonian of subspace S, H_s and the electromagnetic interaction:

$$H = H_s + H_o^{em} + H_I^{em} \tag{2.36}$$

Where H_o^{em} is the free photon Hamiltonian and H_I^{em} is given by:

$$H_I^{em} = \int dx A^{\mu}(x) J_{\mu}(x) \tag{2.37}$$

Where again the H_I^{em} terms involve the Δ resonance.

The above is then used to derive scattering equations for the $\gamma N \longrightarrow \pi N$ process. The real advantage of the Hamiltonian approach over both the Effective

Lagrangian and dispersion relations techniques is in the treatment of πN final state scattering. The Hamiltonian approach reproduces on-shell πN scattering phase-shifts and has a natural extension off-shell, whereas the other two methods rely on Watson's theorem which is only defined on-shell.

The Hamiltonian approach could thus prove invaluable in nuclear calculations if off-shell effects are of particular importance.

2.3 Nuclear Structure Properties of ^{4}He

Before proceeding with a review of the theoretical models of nuclear pion photoproduction we give a brief discription of the ^{4}He nucleus.

As already stated, the majority of nuclear properties can be discussed in terms of the independent particle motion of the nucleons in a mean field, i.e. the shell model. In the shell model the state's available to nucleons are described in spectroscopic notation, nL_j, where n is the principal quantum number, L is the letter that denotes the state's angular momentum l and j is the total angular momentum, where $j = l \pm 1/2$. Each state has a degeneracy of (2j+1) so in ^{4}He the $1S_{1/2}$ states are completely filled, as in figure 2.7. The ground state of ^{4}He has a spin and parity, $J^\pi = 0^+$.

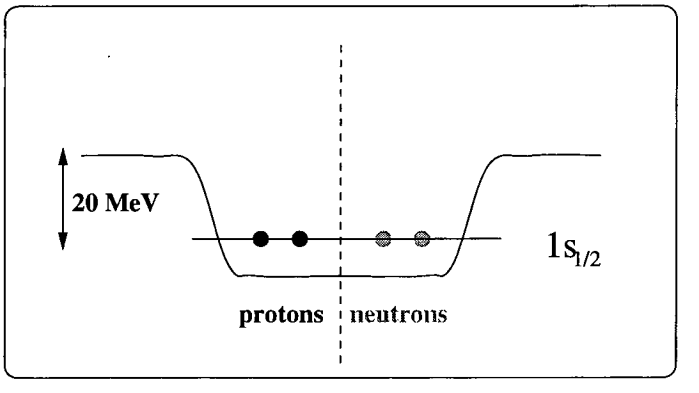

Figure 2.7: *Shell structure of ^{4}He*

In the ^{4}He $(\gamma, \pi^+ n)$ reaction, a proton is removed from the Helium nucleus to leave, in the absence of final state interactions leading to the breakup channel, the Triton ^{3}H nucleus.

2.4 Nuclear Pion Photoproduction

Nuclear pion photoproduction has been long perceived as being of particular interest as it incorporates three basic fields of research, the elementary production mechanism on a nucleon, the nuclear dynamics and the pion-nucleus interaction. We have already seen the various approaches to the first and we can now look at the effects which modify nuclear pion photoproduction compared to the free case. These so called medium modifications will be discussed below as will a review of the various theoretical models used to describe nuclear pion photoproduction.

2.4.1 Medium Effects

The first effect is that, in contrast to free pion photoproduction, the nucleons inside the nuclear environment are in motion. This so called Fermi motion produces a kinematical effect where by the observed cross sections are smeared out. This can make theoretical predictions sensitive to the wavefunction used for the initial nucleus.

The second effect is the so called Pauli blocking. The Pauli exclusion principle states that no two identical fermions can occupy the same state. Protons and neutrons are both fermions and therefore must obey the Pauli exclusion principle. This means the pion photoproduction process cannot lead to states in which the Pauli principle is broken. This Pauli blocking results in a reduced cross section.

The most interesting medium modification is in the delta resonance region. In the free pion photoproduction case a produced Δ will decay to a nucleon and a pion with a branching ratio of 100% and has a decay time expressed as its width $\Gamma = 110\text{MeV}$ ($\sim 10^{-23}$s). In the nuclear medium however the Δ decay becomes more complex. There is now a new decay channel open to the Δ , i.e. $\Delta N \longrightarrow NN$, these are purely nucleonic decays and are shown in figure 2.8. This tends to broaden the resonance and reduce the pion production cross section. However Pauli blocking reduces the states available to the decay products which tends to narrow the width of the resonance.

An interesting question relating to the in-medium resonance is whether or not the peak position is shifted. While there is certainly some evidence [Bia94] for a

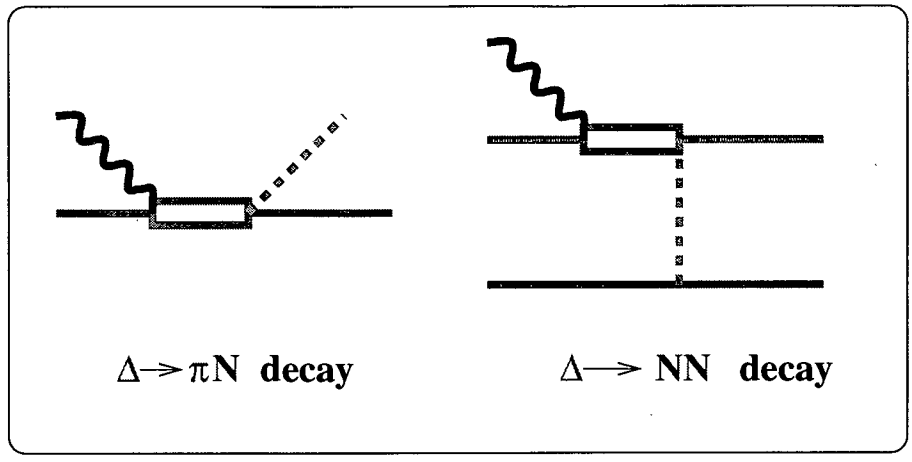

Figure 2.8: *Decay modes of the Delta in the nuclear medium.*

small shift in the in-medium resonance energy relative to the free nucleon value, the shift is however not as prominent as that found in pion absorption. This is thought to arise due to the different nature of the pion and photon absorption processes

The final nuclear medium effect we discuss is the occurence of final state interactions (FSI). These occur after the reaction of interest and involves interactions of the produced particles with the residual nucleus. In particular the reaction products can undergo scattering by the residual nuclear medium, or be reabsorbed by it. This will show up as a reduction in the reaction cross section. This is one of the advantages in measuring the photon asymmetry, Σ, which, as it is a ratio of cross sections, allows the cancellation of FSI effects.

The normal technique for dealing with FSI is by using optical potentials. The plane wave of the exiting particle is distorted by the potential, reproducing the effect of in medium scattering while the imaginary part of the potential brings about a damping of the wave and reduces its flux, which reflects the absorption of the outgoing particles. Optical potentials are energy dependent and are parametrised from scattering data [Sch82, Car82]. Optical potentials are however only really appropriate for medium and heavy nuclei.

2.4.2 Distorted Wave Impulse Approximation (DWIA)

This model has as its starting point the Impulse Approximation, i.e. a single particle model of the nucleus. The incident photon penetrates the nucleus and couples to an individual nucleon via its charge and/or magnetic moment and produces a pion, while the residual nucleus acts as a spectator. The produced particles then subsequently rescatter from the residual nucleus on their way from it. This is called quasi-free pion photoproduction and is depicted in figure 2.9.

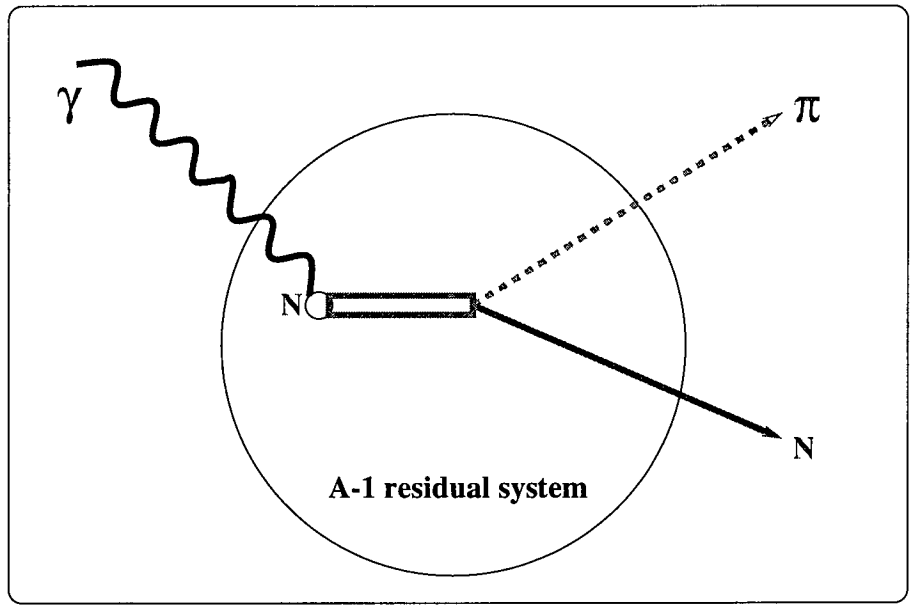

Figure 2.9: *The quasi-free nature of nuclear pion photoproduction*

The first application of the DWIA formalism to A(γ, π^+n) B* was by Laget [Lag72]. The transition operator, T, was taken to be the sum of the free transition operator, t(γ, π) over all the nucleons in the nucleus, that is:

$$T = \sum_{nucleons} t(\gamma, \pi) \tag{2.38}$$

FSI were taken care of by distorting the outgoing waves with optical potentials for the residual system. Blomquist and Laget [Blo77] then improved this by computing the non-relativistic limit of the PV Lagrangian of free pion photoproduction. This gave a convenient transition operator which was valid in any frame of reference thus proving easy to use in nuclear calculations [Sin81]. The

factorised DWIA cross sections can be written as:

$$\frac{d^3\sigma}{dT_\pi d\Omega_\pi d\Omega_n} = k\sigma^{cm}_{\gamma p\to\pi n}|\Psi_l^D|^2 \tag{2.39}$$

Where k is a kinematical factor, $\sigma^{cm}_{\gamma p\to\pi n}$ is the elementary free pion photoproduction cross section in the centre of mass system and Ψ_l^D is the distorted momentum distribution given by:

$$\Psi_l^D = S\int \chi_{\pi^+}^{-(*)}\chi_n^{-(*)}e^{ik_\gamma\cdot r}\phi_i(r)dr \tag{2.40}$$

Where $\chi^{-(*)}$ represents the distorted outgoing pion and nucleon waves, ϕ_i is the bound state wavefunction and S is the spectroscopic factor. The above approach is essentially a local one.

Li *et al.* [Li93] extended this approach by carrying out a fully non-localised DWIA calculation. The expression for the cross section was not factorised and was written as:

$$\frac{d^3\sigma}{dE_\pi d\Omega_\pi d\Omega_N} = k\overline{\sum}|M_{fi}|^2 \tag{2.41}$$

Where k is again a kinematical factor and $\overline{\sum}$ means sum over final spins and average over initial spins. This matrix element in the impulse approximation is given by:

$$\overline{\sum}|M_{fi}|^2 = \frac{1}{2(2J_i+1)}\sum_{\alpha\lambda m_s}\frac{S_\alpha}{2j+1}|T(\alpha,\lambda,m_s)|^2 \tag{2.42}$$

Where J_i is the spin of the target, α = {nljm} is the quantum number of the bound nucleon, λ is the photon polarisation, m_s is the spin projection of the outgoing nucleon and S_α is the spectroscopic factor. The single particle matrix element T is given by:

$$T(\alpha,\lambda,m_s) = \int d^3p'd^3q'\Psi^{(+)}_{m_s}(p',p)\phi^{(+)}_\pi(q',q)t_{\gamma\pi}(\lambda,k,p_i,q',p')\Psi_\alpha(p_i) \tag{2.43}$$

Where $p_i = p' + q' - k$ is the momentum of the bound nucleon. The pion production operator $t_{\gamma\pi}$ is the full Blomquist-Laget operator. The above operator is non-local which Li *et al.* claim to be of importance when comparing with experimental results.

If the distorted pion and neutron wavefunctions are replaced with plane waves. the matrix element takes the simple form:

$$T^{PWIA}(\alpha,\lambda,m_s) = \chi^\dagger_{m_s}t_{\gamma\pi}\Psi_\alpha(p_i) \tag{2.44}$$

Which is the production operator multiplied by the Fourier transform of the single particle bound wavefunction. This is called the Plane Wave Impulse Approximation (PWIA) and is compared with the data presented in this thesis.

2.4.3 The Δ-Hole Model

The Δ-hole model assumes the produced Δ to be the dominant initial process, this produced Δ and its associated hole then propagate through the target nucleus and the resulting medium effects are accounted for. The Δ-hole model has its origins in pion-nucleus scattering and the Isobar-Doorway model of Kisslinger [Kis73]. As the same Δ-propagator should apply to the photonuclear case as well as the pion-nucleus interaction, Sato and Takaki [Sat93] applied the Δ-hole model to A $(\gamma, \pi^+ \mathrm{n})$ B reactions.

The resonant (delta) part of the transition amplitude is given by:

$$t_\Delta = F^\dagger_{\pi N\Delta} \frac{1}{D(E)} \hat{F}_{\gamma N\Delta} \tag{2.45}$$

Where the F terms are vertex functions relating to the absorption of a photon, $\hat{F}_{\gamma N\Delta}$, and the emission of a pion, $F^\dagger_{\pi N\Delta}$. The resonance denominator has the Breit-Wigner from:

$$D(E) = E - E_R + \frac{1}{2} i\Gamma(E) \tag{2.46}$$

To incorporate the effects of the nuclear medium on the resonant production the function D(E) is replaced by the many-body Green's function:

$$G^{-1}_{\Delta\, h} = D(E - H_\Delta) - W_\pi - \delta W - V_{sp} \tag{2.47}$$

W_π is a rescattering term that takes into account coherent π^0 production and subsequent charge exchange. Pauli blocking of the delta decay inside the nucleus is taken into account via the term δW, while V_{sp} is a phenomenological spreading potential that takes into account intermediate coupling of the delta-hole state to more complicated configurations, mainly pion absorption, which is determined from pion-nucleus scattering.

The resonance term is evaluated at $E - H_\Delta$ which is the internal energy of the resonant πN system. The Δ-Hamiltonian, H_Δ is given by:

$$H_\Delta = T_\Delta + H_{A-1} + V_\Delta \tag{2.48}$$

Where T_Δ is the kinetic energy of the delta, V_Δ is a binding potential for the delta and H_{A-1} takes into account the hole energy. The resonant production operator thus becomes:

$$\tau_\Delta = F^\dagger_{\pi N\Delta} G^{-1}_{\Delta\, h} \hat{F}_{\gamma N\Delta} \tag{2.49}$$

To obtain the full amplitude a non-resonant (background) contribution has to be added to the above $M_{1+}(3/2)$ resonant term. A further contribution from the pion-pole contribution has also to be added to the production amplitude giving:

$$t = t_{M_{1+}(3/2)} + t_{pion-pole} + t_{b.g.} \tag{2.50}$$

The full amplitude in the Δ -hole model becomes:

$$T = < \psi_p^{(-)} \phi_\pi^{(-)}; h | \tau_\Delta + t_{b(3/2)} + t_{pion-pole} + t_{b.g.} | k; 0 > \tag{2.51}$$

Where $|0>$ and $|h>$ denote the nuclear ground state and the one-hole state, while $|k>$ denotes the incident photon with momentum k. $\psi_p^{(-)}$ and $\phi_\pi^{(-)}$ represent distorted proton and pion waves.

Sato and Takiki compared their calculations with the MIT data which again compared well at backward pion angles but considerably overestimated the data at forward pion angles.

2.4.4 Full Microscopic Model

The final nuclear pion photoproduction model we will look at was developed by Carrasco, Oset and collaborators [Car92a, Car92b, Car94]. They used the basic interaction between photons, pions, nucleons and isobars expressed in terms of coupling constants, form factors, and propagators to calculate the photon self energy diagrams of figure 2.10 by applying field theoretical methods.

In infinite nuclear matter a photon, due to its interaction with the nucleons acquires a self-energy given by:

$$\Pi(k, \rho) = 2\mathrm{E}_\gamma \, V_{opt} \tag{2.52}$$

The imaginary part of the self-energy represents the loss of photon flux in the medium, at a rate given by:

$$\Gamma = -2ImVopt = -\frac{1}{|k|} Im\Pi(k, \rho) \tag{2.53}$$

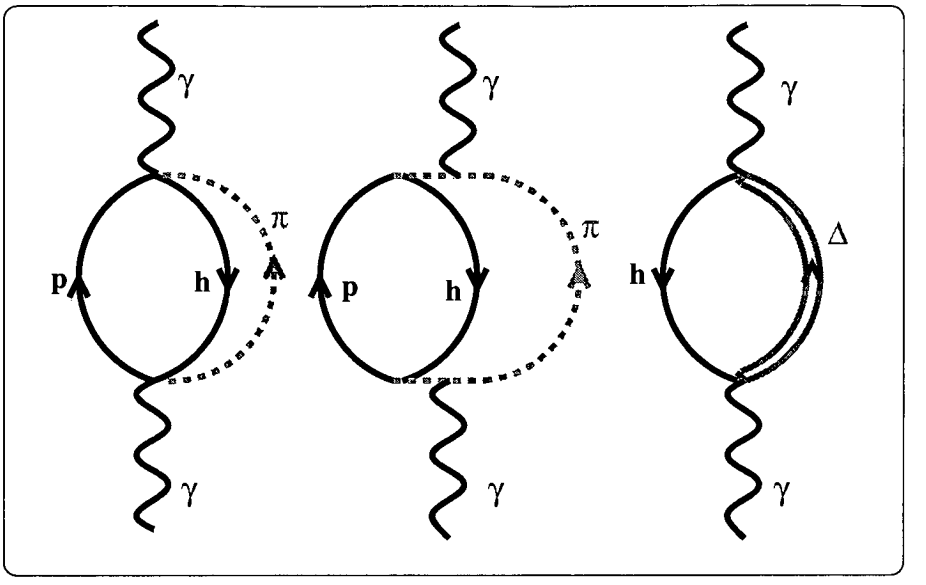

Figure 2.10: *Typical photon self-energy Feynman diagrams*

, where k is the photon momentum. Because of the weak nature of the electromagnetic interaction a volume integral is applied to the above to give an expression for the cross section on a finite nucleus:

$$\sigma = -\left(\frac{1}{|k|}\right) \int d^3r Im\Pi(k, \rho(r)) \tag{2.54}$$

,where the Local Density Approximation (LDA), $\rho \rightarrow \rho(r)$ provides the connection between finite and infinite nuclear matter. The above expression is useful in that it allows us to evaluate σ on any nucleus while only knowing the experimental nuclear density, ρ. Final State Interactions within the nuclear medium are treated semi-classically by means of monte carlo type simulation.

The main advantage of the above approach is in its ability to differentiate between the various reaction channels, that is the absorption of the photon can be separated into direct and indirect absorption. In the direct absorption case the photon is assumed to be absorbed by one or two nucleons, while the indirect case is a two step process. Carrasco *et al.* suggest a study of these two processes will give valuable information regarding pion propagation in nuclei.

The main drawback in applying the above method is that it lacks any nuclear structure input. As it is derived from nuclear matter calculations, no shell

model structure effects are present in the model. While this has proved acceptable for inclusive calculations it causes significant problems when applied to exclusive experiments.

Chapter 3

Experimental Equipment

3.1 Introduction

The pion photoproduction results presented in this thesis were obtained using the facilities at the Insitut für Kernphysik at Mainz. The Mami Microtron (MAMI-B), which delivered its first continuous electron beam in 1990, has facilitated many new high quality photonuclear experiments.

The different experimental areas are each operated by separate collaborations, in particular the A2 collaboration studies reactions involving tagged real photons. Within the A2 collaboration there exists several sub-groups each associated with specific areas of research. The Universities of Glasgow, Edinburgh and Tübingen form what is known as the PiP-TOF collaboration. The present experiment is the latest in a series of experiments performed by the PiP-TOF group which are aimed at gaining an understanding of the photoabsorpion mechanism by studying (γ,pN) and (γ, π^+n) reactions. The group takes its name from the two main detector systems which are used in these experiments, PiP, a scintillator hodoscope designed to detect protons and positive pions, and TOF, a large scintillator time-of-flight array designed for charged and neutral particle detection. Also crucial to the experiments in the A2 hall is the Glasgow Tagger. There are also associated Δ E detectors which are used for triggering and particle identification. Each of the above elements will be discussed below, as will the electronic and computing systems required for triggering, data acquisition and online analysis.

3.2 MAMI-B

The MAMI-B facility is shown in figure 3.1. A 100 keV gun is followed by three linac sections which inject 3.5 MeV electrons into the 20 turn Race Track Microtron (RTM1), this increases the electron energy to 14 MeV. The electrons are then transported to the 51 turn RTM2 which accelerates the electrons to 180 MeV. This formed the basis of the MAMI-A system [Boe95].

MAMI-A was upgraded to MAMI-B in 1990 with the addition of the 450 tonne RTM3 third stage. This has 90 turns and produces a final electron beam of 855 MeV, with a resolution of 120 keV and a 100% duty factor. It is a high quality, highly stable beam with a maximum current of 100 μA and a low emittance. Once extracted from RTM3 the beam can be transported to any number of experimental halls, shown in the plan. Photonuclear reactions take place in the A2 hall where a radiator and the Glasgow tagger system are installed.

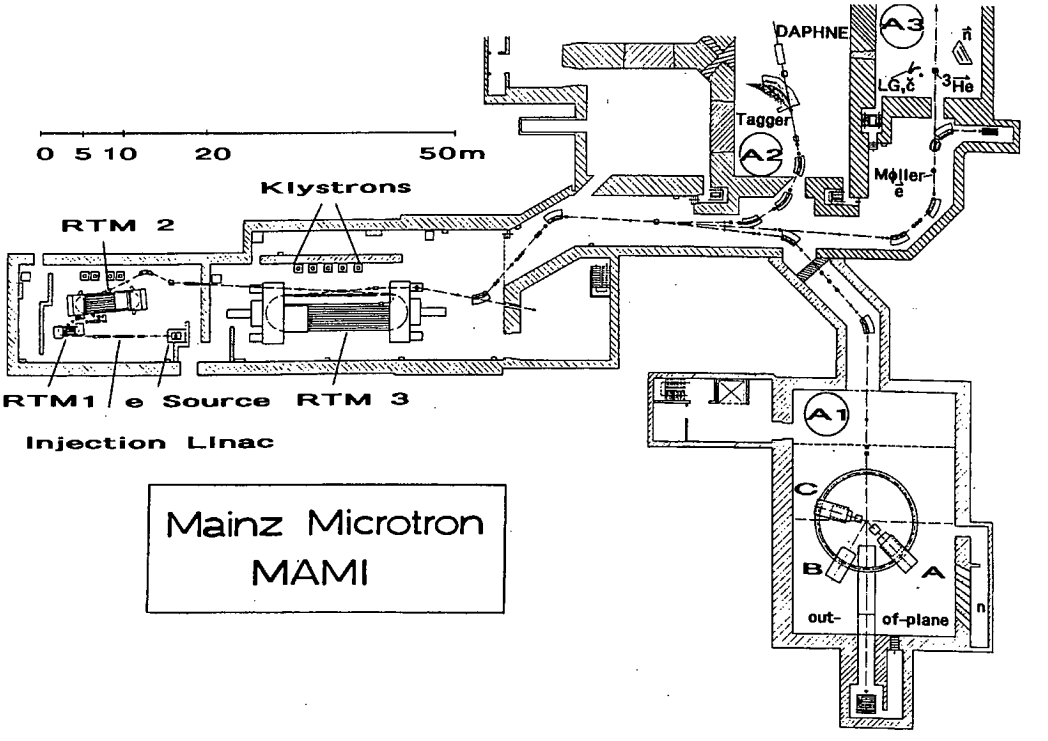

Figure 3.1: *The Mainz Microtron, MAMI*

3.2.1 Race Track Microtrons

Each of the three race track microtrons consists of a linear accelerating section (linac), two bending magnets and a collection of return pipes which lead to its characteristic race track shape, as shown in figure 3.2.

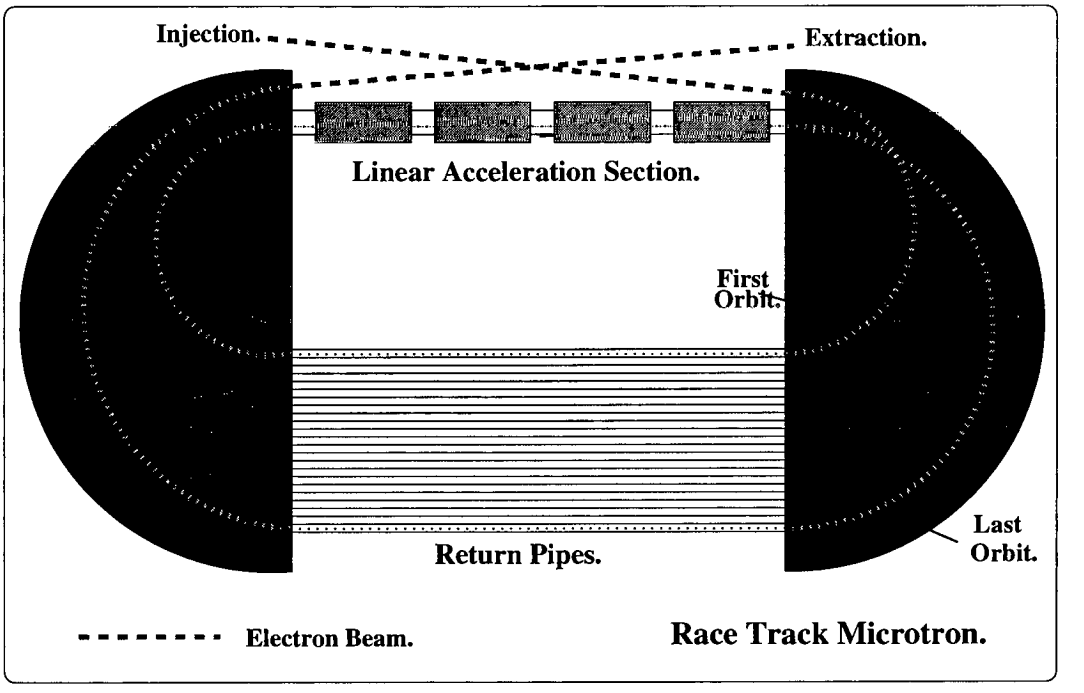

Figure 3.2: *A Race Track Microtron*

Electrons are injected into the linac of the microtron and gain a certain amount of energy. The electrons are deflected by 180° at each of the bending magnets. Every time an electron passes through the linac it gains more energy and the track through which it is travelling widens, this is repeated until the electron has gained enough energy to encounter the extraction magnet which allows it to leave the microtron.

Because each electron is recirculated many times, the energy gain each pass through the linac can be relatively low. This allows the linac to be operated in continuous wave (c.w.) mode to produce a beam with a 100% duty factor. This is of vital importance in coincidence experiments, for two systems with the same average current the rate of accidental coincidences will be less with a system with a continuous beam than one with a pulsed one. This allows higher currents to be

used, thus the higher duty factor allows quicker and more accurate collection of data.

3.3 Bremsstrahlung Photon Production

To produce a photon beam the electrons from MAMI-B are focussed on to a radiator in the A2 hall. When the radiator is the 4μm Ni foil, unpolarised photons are produced as the electron decelerates in the presence of the Ni nuclei. These bremsstrahlung photons radiate in a forward cone of average semi-angle m_e/E_e where m_e is the mass of the electron and E_e is the electron kinetic energy and have an energy distribution approximately proportional to $1/E_\gamma$ [Bet34].

When the radiator is the 0.1mm diamond crystal the production of linearly polarised photons becomes possible. In contrast to the smooth incoherent $1/E_\gamma$ bremsstrahlung spectrum, the coherent bremsstrahlung spectrum shows a peak, the position of which depends on the orientation of the crystal with respect to the electron beam. The photons in this peak are mostly linearly polarised. This is shown in figure 3.3. The lower part of this figure shows the relative intensity of coherent radiation, that is the diamond spectrum normalised to the incoherent contribution (Ni). This shows a number of peaks which are the contributions from different reciprocal lattice vectors.

The kinematics of the coherent bremsstrahlung process are shown in figure 3.4. The energy & momentum of the incoming electron is denoted as (E_0, p_0), while (E, p) is the energy & momentum of the outgoing electron, k is the energy of the produced photon which has polarisation ϵ, while q is the momentum transferred to the crystal. The fractional photon energy is defined as $x = k/E_0$.

Production of coherent bremsstrahlung is governed by the momentum transfer q, which has to fullfill the so called momentum "pancake" condition [Lo94]:

$$\delta \leq q_l \leq 2\delta \tag{3.1}$$

$$0 \leq q_t \leq 2x \tag{3.2}$$

Where q_l & q_t are the longitudinal and transverse components of q. $\delta = q_l^{min}$ is the minimum longitudinal momentum transfer.

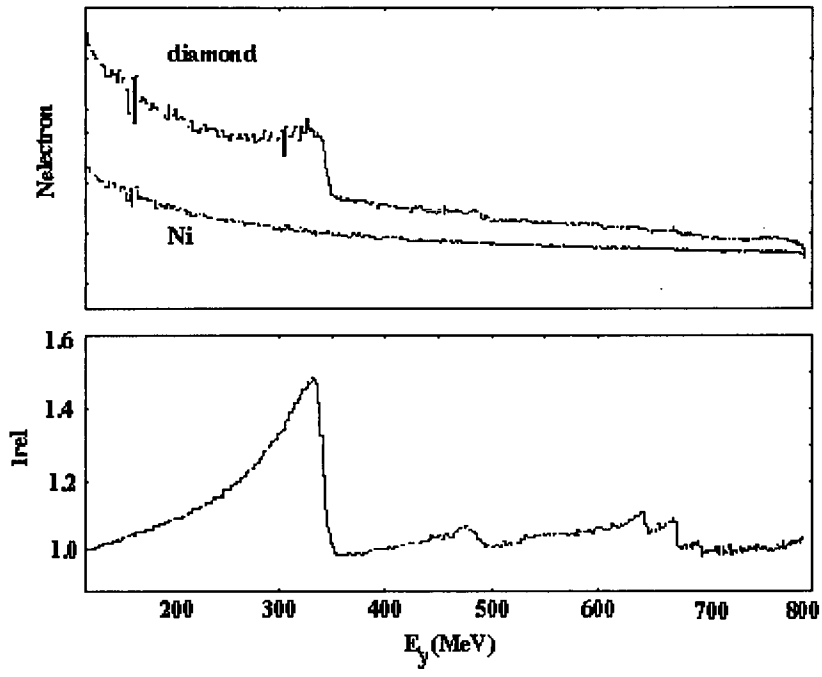

Figure 3.3: *Bremsstrahlung spectra*

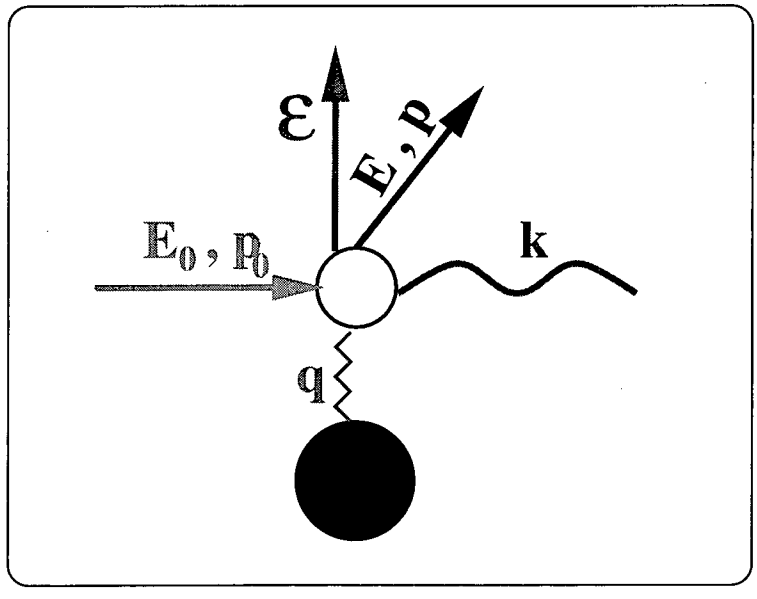

Figure 3.4: *Kinematics of the Bremsstrahlung process*

Maximum linear polarisation occurs when the momentum "pancake" is on only 1 reciprocal lattice point [Lo94]. This is shown in figure 3.5 in which the pancakes in the reciprocal lattice space of the diamond are shown for two different photon energies. This leads to a region of photons, around 50 MeV in width, which have a high degree of polarisation. The diamond was flipped periodically by 90^o to produce both parallel and perpendicularly polarised photons.

By using the Tagger it is possible to survey and adjust the diamond crystal. To obtain the correct orientation of the diamond, which is mounted in a goniometer, it is vital to have an accurate knowledge of its original position. To this end a three dimensional plot was made of the relative intensities of coherent bremsstrahlung as a function of photon energy and the orientation of the horizontal goniometer axis, Φ_H. This plot, shown in figure 3.6, can be made in a short space of time, shows the symmetry around the zero goniometer position. This gives direct information about the orientation of the crystal with respect to the incoming beam and thus allows an absolute calibration of the goniometer.

3.3.1 The Tagged Photon Technique

The residual electrons from the bremsstrahlung process are then analysed in a magnetic spectrometer. With a knowledge of the incident electron energy, E_e, which for MAMI-B is 855 MeV, and a measurement of the residual electron energy $E_{e'}$, the associated (coincident) photon's energy is given by:

$$E_\gamma = E_e - E_{e'} \tag{3.3}$$

The photon beam is collimated to form a small beam spot on the target which is several metres downstream. The photons subsequently induce reactions in the target which generates experimental triggers. Photon tagging requires an identification of the particular residual electron that is coincident with the photon responsible for a given reaction trigger. This requires accurate timing information to separate the prompt electrons that are correlated with a photon from random electrons that are not correlated with the photon causing a reaction.

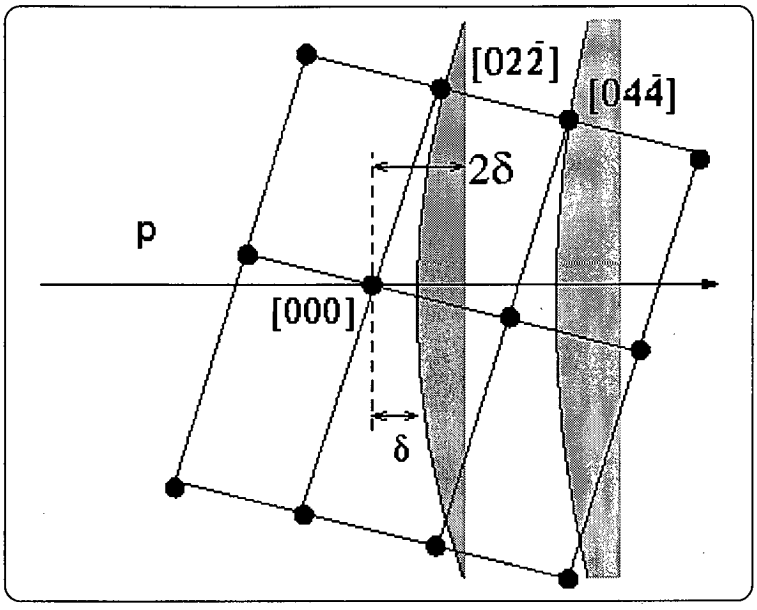

Figure 3.5: *Reciprocal lattice of the diamond crystal*

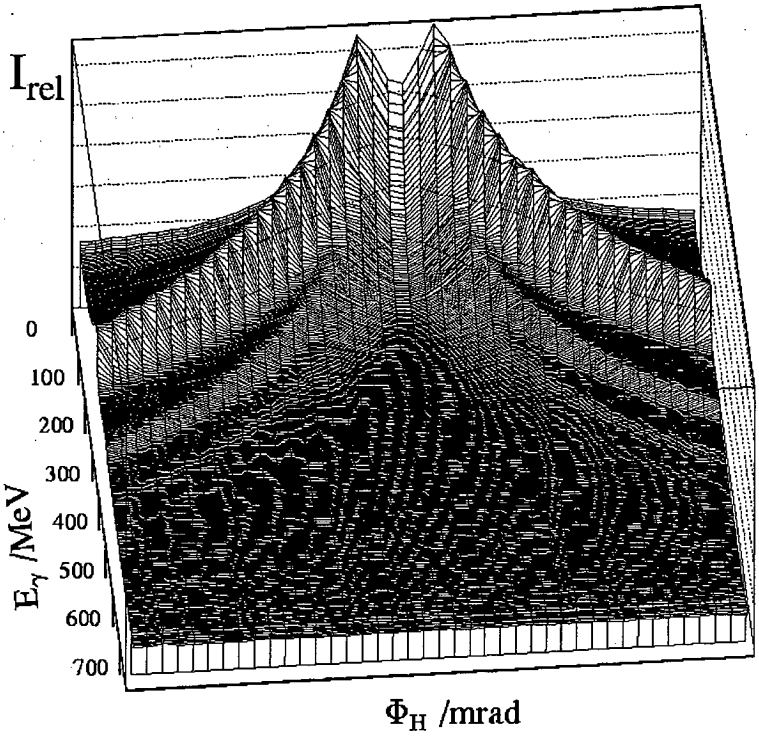

Figure 3.6: *Calibration of the diamond position*

3.3.2 The Glasgow Tagging Spectrometer

The Glasgow Tagger [Ant91] is shown in figure 3.7 The Tagger analyses the residual electrons from the bremsstrahlung process and also transports the electrons which do not interact with the radiator to the beam dump. To accommodate the wide range of experiments performed within the A2 collaboration the design of the spectrometer had to be extremely flexible. The spectrometer has a large momentum acceptance, $p_{max} : p_{min} \simeq 16 : 1$, and can cover the energy range 40 MeV to 790 MeV in a single field setting. It also has a large enough entrance solid angle to accept most of the post bremsstrahlung electrons.

To accomplish this a Quadrupole-Dipole (QD) design was chosen. The quadrapole magnet provides vertical focusing, while the dipole magnet bends and focuses the electrons onto the focal plane.

3.3.3 The Focal Plane detector

A residual electron's energy is established by simply determining the point at which it traversed the spectrometers focal plane. Knowledge of this combined with the strength of the magnetic field leads to an unambiguously determined electron energy. The Focal Plane Detector (FPD) is an array of 352 overlapping scintillators, each of which is connected to a small photomultiplier (PM) tube. In order to reduce the contribution from the background electrons a coincidence is demanded between neighbouring array elements.

For photonuclear reactions between 100 MeV and 800 MeV the focal plane detector had to satisfy the following criteria [Hal96]:

- Run at such a rate as to provide an adequate photon flux. For the low cross sections under investigation this corresponds to fluxes of the order of $10^6 - 10^8$ photons per second.

- Label each photon with a sufficiently good energy resolution. The Glasgow Tagger has an average resolution over the whole focal plane of $\sim 2MeV$.

- Define the arrival time of each electron with sufficient precision to provide an unambiguous correlation with a photon inducing a nuclear reaction.

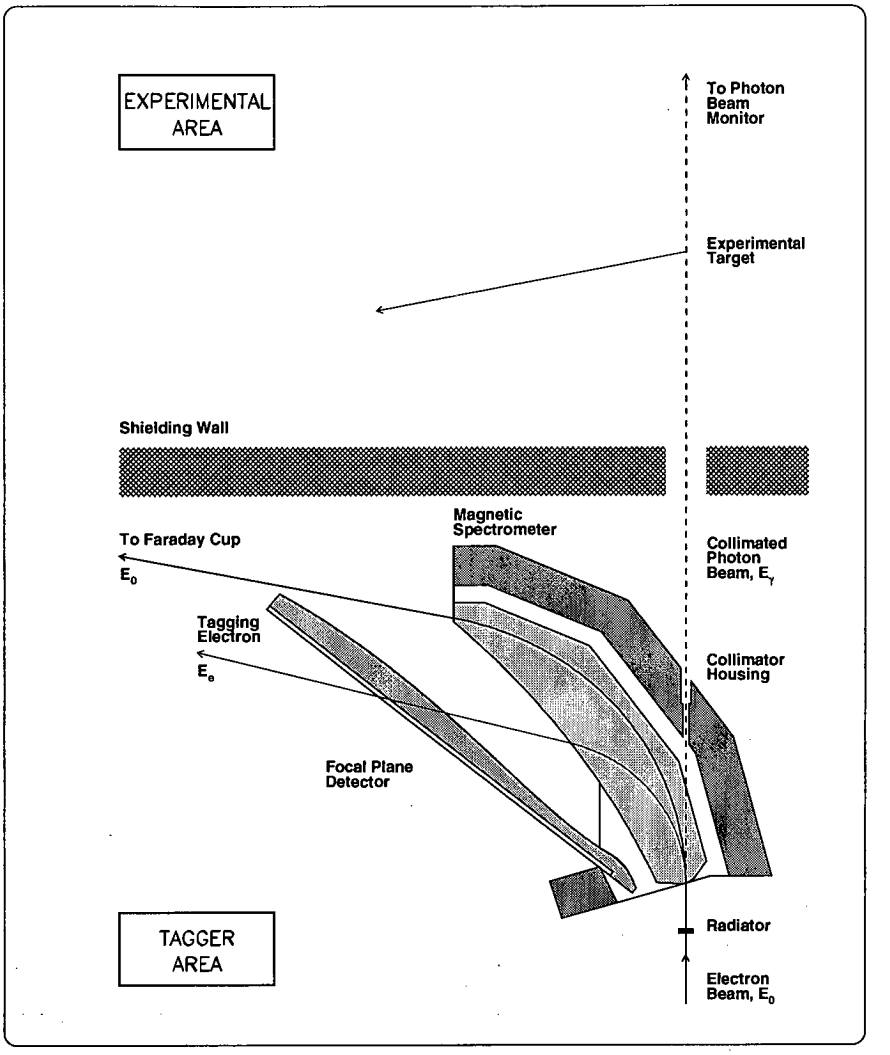

Figure 3.7: *The Glasgow Tagging Spectrometer*

- Delay timing and hit pattern information until an experimental trigger has been made, indicating whether or not to process the event data

The signal from the scintillator's photomultiplier tube enters a dual threshold discriminator which produces an associated logic pulse which is routed to the tagger electronics racks where the FASTBUS scalers and time to digital converters (TDCs) record the required information. The scalers are used to obtain a measurement of the photon flux, while the TDC signals are used to establish a coincidence between a residual electron hit in the FPD and a reaction in the target caused by a photon.

3.3.4 Photon Collimation and Tagging Efficiency

The distance between the radiator and the target is several metres, because of this the photon beam must be collimated to ensure a small beam spot is incident on the target. A small beam spot is advantageous in that it reduces the error in establishing the reaction vertex. The collimation process also helps in increasing the degree of polarisation when the diamond radiator is used. This is due to the fact that the angular distributions of incoherent and coherent bremsstrahlung are different. The typical size of collimator used was 3mm.

During the experiment the vast majority of photons do not interact with the target and are dumped at the far end of the A2 hall. The photon beamline is shown in figure 3.8 which also shows the ionisation chamber that is used to obtain a rough estimate of the photon flux. However the ion chamber is only used as a diagnostic and in the analysis it is the tagger scalers that are used to obtain the photon flux. The scalers count the number of electrons detected in each FPD element. Some of the photons with a corresponding electron in the FPD are removed from the beam by collimation and the fraction which reach is given by:

$$N_\gamma|_{(coincident\ with\ e'\ at\ FPD)} = N_e \cdot \epsilon_{tagg} \tag{3.4}$$

Where ϵ_{tagg} is the tagging efficiency and is defined as the ratio of electron hits on the FPD which have a coincident photon, to the total number of electron hits at the focal plane. The tagging efficiency is measured by placing a Pb glass detector in the photon beam well downstream of the target. The size of the detector ensures that it has a photon detection efficiency very close to 100%. The beam current is lowered to suppress random coincidences in the tagger. The Photons incident on the detector generate triggers which gate the tagger TDCs. The TDCs record the time of any coincident residual electron on the FPD. Meanwhile the tagger scalers count the total number of residual electrons in each element. Thus the tagging efficiency for each element is defined as:

$$\epsilon = \frac{TDCcounts}{scalercounts} \tag{3.5}$$

Tagging efficiency measurements were made several times a week. The average efficiency for unpolarised photons was around 55%, while for polarised photons it

rises to a maximum of 50 % in the region corresponding to the maximum degree of polarisation.

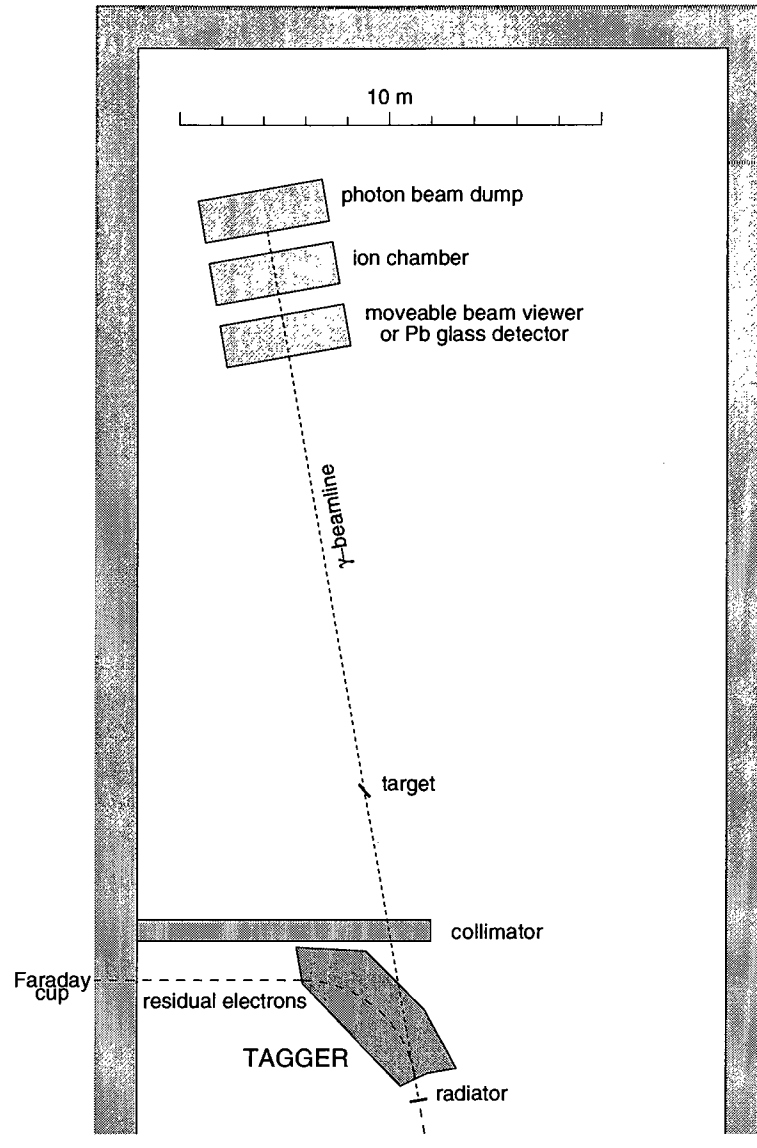

Figure 3.8: *The photon beam line*

3.4 Experimental Targets

The two main targets used in this experiment were a liquid Helium-4 target, used to perform the ^{4}He$(\gamma, \pi^+$n) measurement, and a solid CH_2 target that was used to obtain the p(γ, π^+)n calibration data.

The Helium target was purpose built by the University of Tübingen [Heh96]. Figure 3.9 shows a schematic of the target. The target is cylindrical along the photon beam axis with a diameter of 3cm and a length of 8cm. The wall material is Kapton. The cell is wrapped with several layers of superisolating foil to reduce the heat input. A vacuum chamber surrounds the target cell and is made of a carbon fibre cylinder. The Helium was cooled with a liquid nitrogen jacket, and had to be refilled on average every 12 hours by pumping more in from the top.

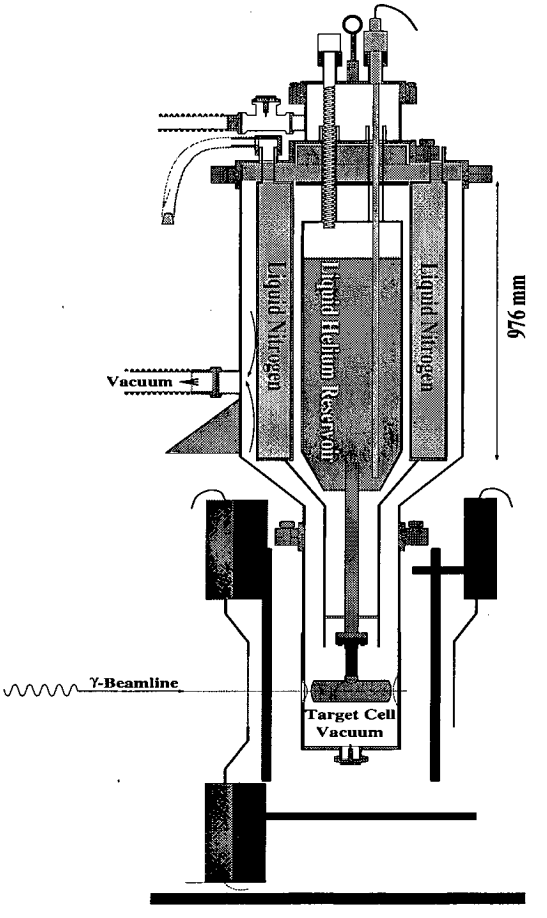

Figure 3.9: *The liquid helium target*

3.5 Particle Detectors

When the photon impinges upon the target there are a large number of different possible reaction channels open to it. As well as nuclear reactions there is also the possibility of the photon undergoing an atomic reaction (γ, e) this leads to a large electron background. The particle detection systems used in this experiment thus had to be designed to discriminate between the various reaction products produced so as to select a specific reaction channel. Particles emitted include, electrons, protons, pions and neutrons. There are a variety of techniques to differentiate between these particles in particular $\Delta E-E$ cuts, veto detectors and the afterpulse technique are all used.

Energy measurements are made by either particle energy deposition or time-of-flight methods and it is important to achieve a satisfactory energy resolution. In the present experiment a combined resolution of around 10 MeV was achieved. The third important factor in the design of the detector systems is that of angular resolution. In order to perform a comparison with theoretical predictions good angular resolution is required. This depends on the detector timing properties.

The arrangement of the detectors in the A2 hall for the experiement is shown in figure 3.10 The three detector systems, the Δ-E ring, PiP and TOF all consist of scintillator blocks. When a charged particle enters a scintillator block the scintillator material emits light which travels to the ends of the block and is focussed by light guides on to a photomultiplier tube. The photomultiplier converts the light into an electrical signal and amplifies it. The amount of light emitted is proportional to the energy of the particle, and by finding the time difference between when the light reaches either end of the scintillator bar a position measurement can be made.

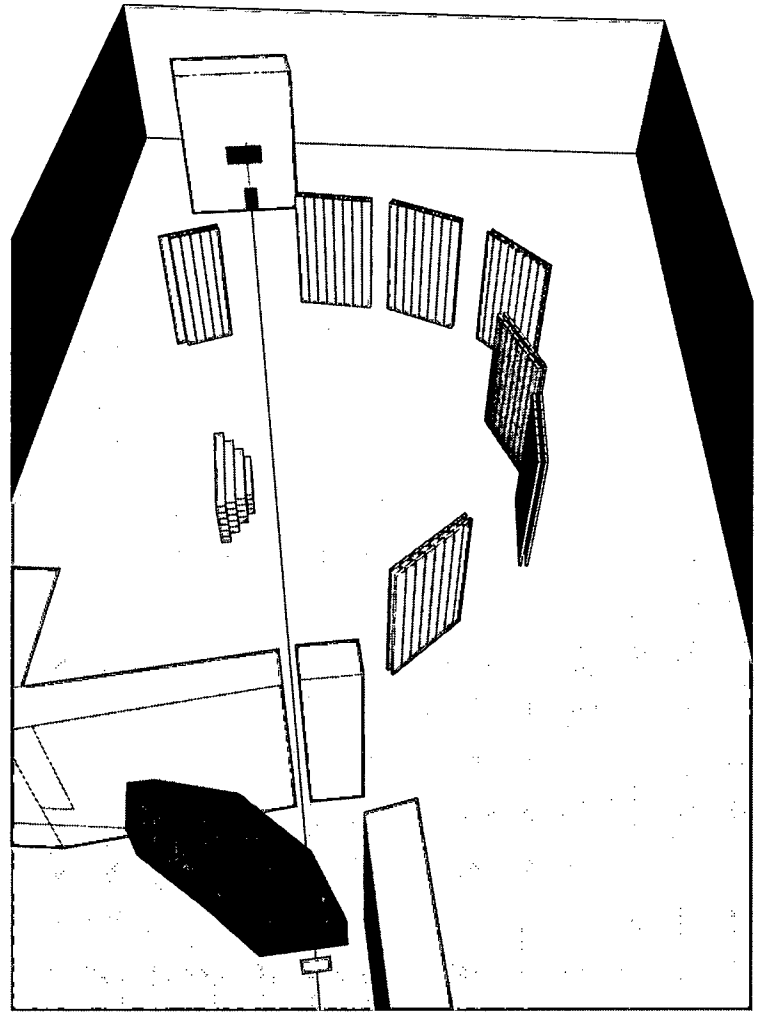

Figure 3.10: *The layout of the A2 hall*

3.5.1 The ΔE Detector

The ΔE detector is shown schematically in figure 3.11. The ring is centred on the target and has a radius of 11cm. Both sides of the ring have seven separate scintillator segments. The detector performs two main functions.

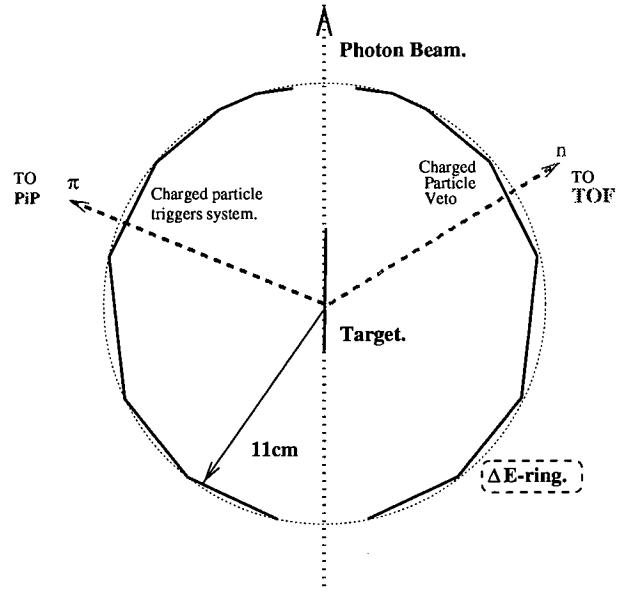

Figure 3.11: *The ΔE detector*

On the PiP side, a charged particle passing through the ΔE detector will give a signal, this is then used as the so called start time which is closely related to the reaction time due to the detector being in close proximity to the target. All other times are measured relative to this time. This ΔE signal can also be used in conjuction with PiP to perform a ΔE-E cut which can eliminate a lot of background, i.e. electrons and random events. It can also separate pions from protons.

The TOF side segments are used as a charged particle veto. Since neutrons are neutral particles they do not give a signal in the ΔE detector whereas protons, being charged do. This veto is performed in the offline analysis to avoid accidental vetoing by randoms. By selecting on events that do have a signal in the TOF side ΔE detector it becomes possible to study reactions involving charged particles on the TOF side.

3.5.2 The PiP detector

The PiP detector is a highly segmented Pion/Proton scintillator hodoscope [Mac96b]. The detector consists of five separate layers of scintillator, NE110. The first layer is a thin ΔE layer followed by four E layers, E1 to E4. This is shown in figure 3.12.

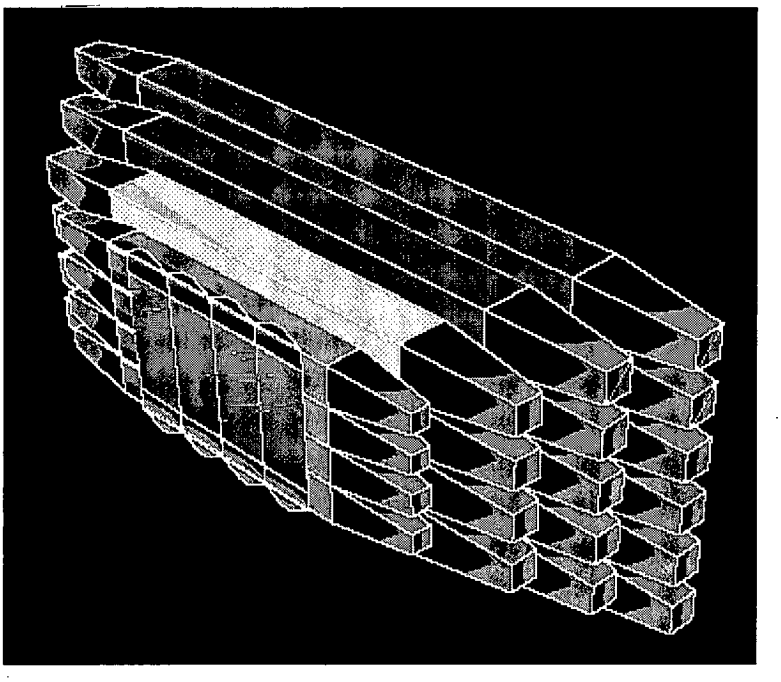

Figure 3.12: *The PiP detector*

The ΔE layer consists of four vertical scintillator strips of dimensions 2mm thick x 20cm wide x 42cm high. In its usual position of 50cm from the target, this defines the solid angle of PiP to be $\simeq$ 1.0 steradian. The ΔE layer is also used to provide azimuthul position information.

Each successive E layer is larger than the previous one, so as to ensure that a particle entering the detector will not pass out through the detector's edges in a subsequent layer, even after allowing for scattering events inside the detector [Bra91]. The light produced in the blocks is guided into photomultiplier tubes at both ends of a block using light guides. The dimensions of the E layers are given in table 3.1.

Each block is shielded from external light sources by the use of black tape,

E layer	No. Blocks	L x D x H (cm)
E1	4	100.0 x 11.0 x 13.5
E2	4	130.0 x 17.5 x 17.5
E3	5	160.0 x 17.5 x 17.5
E4	6	190.0 x 17.5 x 17.5

Table 3.1: Scintillator block dimensions in PiP

while the whole system is shielded by a 5mm steel plating to further reduce light leaks and provide a barrier against room background. The detector is mounted on a strong steel framework with the electronics in four racks at the rear of the detector. The total weight of the detector is around 4 tonnes.

3.5.3 The TOF Detector

The TOF array consists of 102 scintillator bars [Gra98]. These bars are mounted vertically on movable frames eight at a time and placed at between 4m and 7m from the target. The TOF array was designed to maximise the solid angle, time resolution and detection efficiency while still being able to be applied in a variety of different experiments [Bra91]. The height of the A2 hall and the required timing resolution, gave rise to bars with the dimensions 300cm x 20cm x 5cm. Again light is collected at both ends by photomultiplier tubes. The azimuthul position of a detected particle is determined by the time difference, while the polar angle is just given by which bar the particle struck. The time of flight, which is used to determine a particle's energy, is obtained by the average time of both signals. A typical TOF frame is shown in figure 3.13.

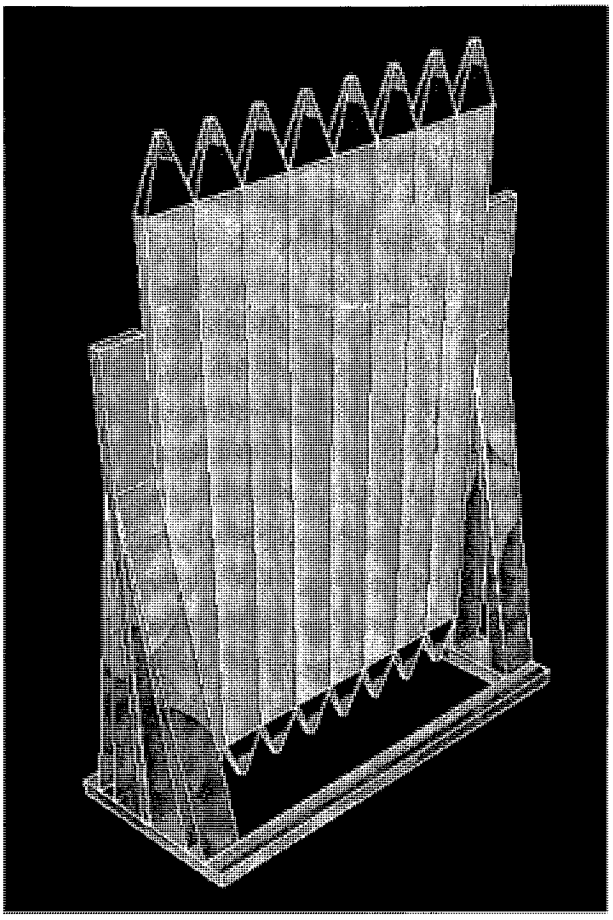

Figure 3.13: *A typical TOF stand*

3.6 Event Triggering

When a particle enters a detector block the resulting signal in the photomultiplier tubes must be transformed in to a useful form for analysis. This is done in three stages. Firstly, events of interest must be identified from the sea of background and random events, this is done by the trigger electronics, which on recognising a desired event gate the analogue to digital converters (ADC's) that are used to digitise pulse height and timing information. Lastly storage of this information is performed by the data acquisition system which reads out these modules. Because the experiment is disabled when this is taking place, this dead time must be kept to a minimum which in practice means making a trigger as selective as possible without throwing away valid events.

For a given event the experimentalist needs to know, the pulse height of the signals in each PM tube which are recorded in charge to digital converters (QDC's) and the time of each PM signal relative to the start time, which is recorded when a pulse is able to produce a logic pulse in a leading edge discriminator which rises over a preset threshold and then stops the time to digital converters (TDC's).

Figure 3.14 shows the basic instrumentation found in all detector scintillator blocks of the PiP, TOF and ΔE detectors.

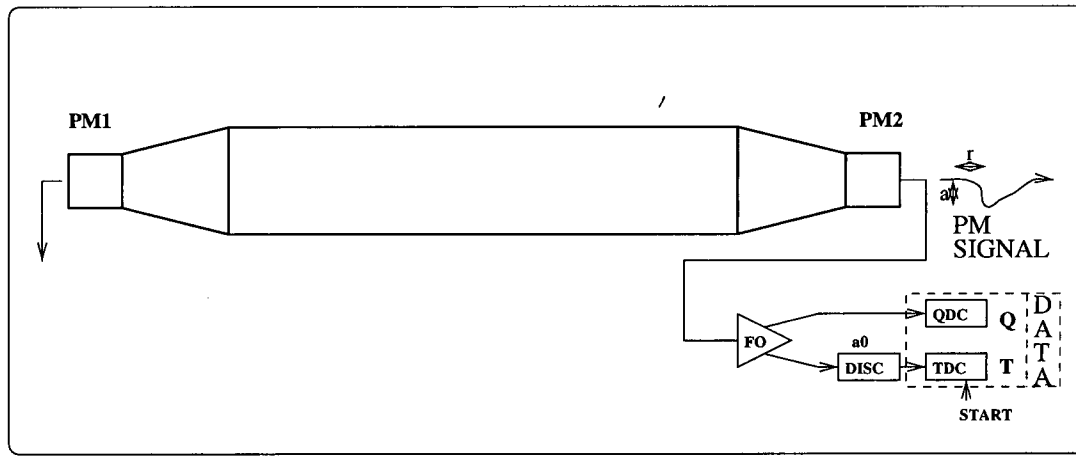

Figure 3.14: *Instrumentation of a typical scintillator block*

The output from the ADC's forms the raw data which is later analysed to reconstruct the kinematics of an event, e.g. particle energies, angles etc.

3.6.1 Trigger Logic

The trigger electronics use the pulses from the discriminators to decide whether an event of interest has occurred. For the 1996 set of experiments a joint $(\gamma, \pi^+ n)$, (γ,pN) trigger was employed enabling the collection of both types of events, and meaning the beam time for the separate experiments was combined together. The events of interest were defined as:

- Event in PiP with an associated particle in TOF
- Cosmic event in PiP
- PiP or TOF flasher events

The last two types of events were used for calibration purposes and gain monitoring.

A two level trigger system was used due to the timing limitations and a need to minimise dead time. The first level trigger is used to make fast and simple decisions. This trigger can gate the ADC's and start converting the event for storage, reject an event immediately, or alternatively initialise the second level trigger if further investigation of the event is required. The second level trigger can make more complex decisions on an event and after a preset time decides whether to keep the event and thus initiate the data acquisition which is a time consuming process or to reset all the ADC's and thus reject the event. A flow diagram of the decision making process implemented by the trigger logic is shown in figure 3.15.

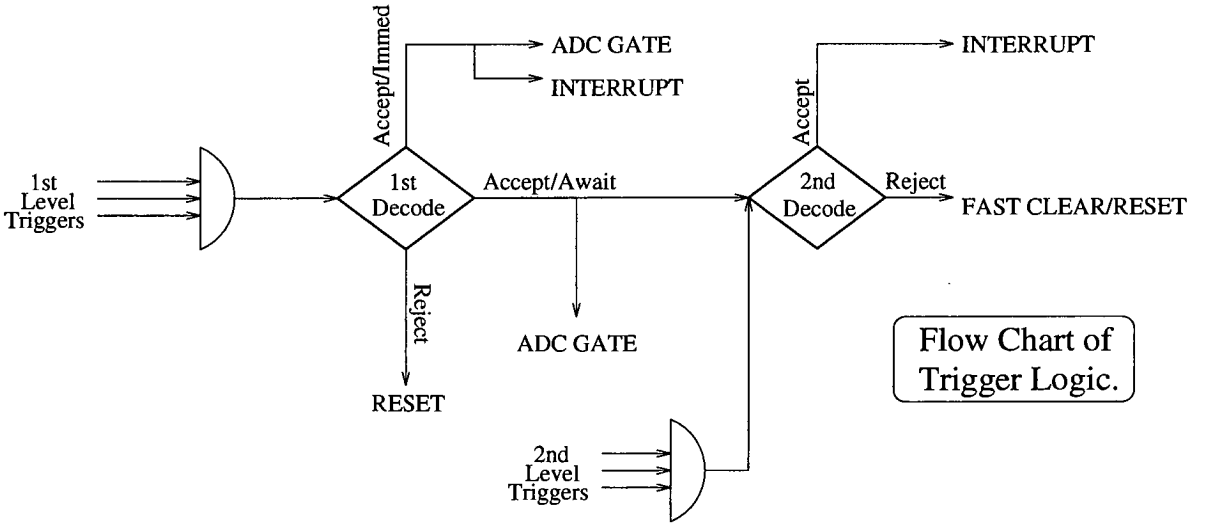

Figure 3.15: *Flow diagram of the trigger logic*

3.6.2 First Level Triggers

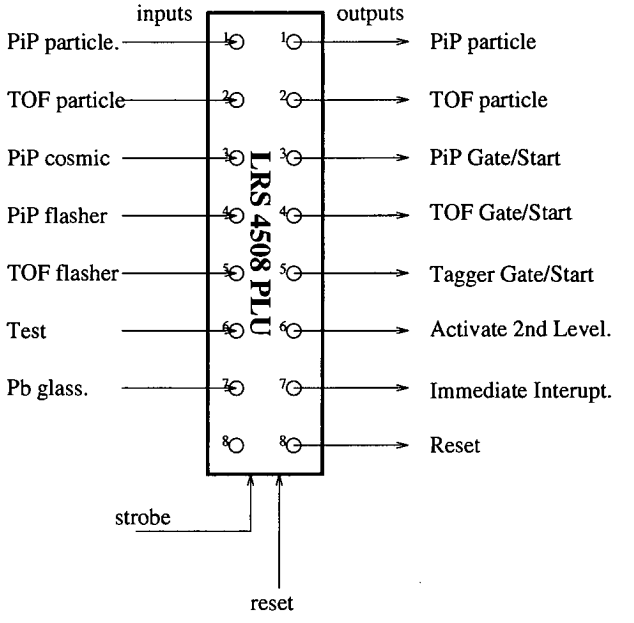

Figure 3.16: *The 1st level trigger*

There are four main types of first level trigger input, the signals from these are input into a Programmable Logic Unit or PLU which decodes them and then acts accordingly. The 1st level PLU decoder is shown in figure 3.16. The trigger inputs are:

- **The PiP particle trigger:** This guarantees a charged particle in PiP. The time of this trigger corresponds closely to the reaction time and QDC and TDC starts are derived from it. It is generated by demanding coincidence signals from the PiP-side ΔE, the PiP ΔE layer and the first PiP layer, E1.

- **The Cosmic Trigger:** For calibration purposes, PiP cosmic ray events are recorded. The trigger demands a coincidence between the top block in a layer and the bottom block of the same layer. If the PLU receives this input readout is enabled immediately.

- **PiP and TOF Flasher Triggers:** Both PiP and TOF have flasher units installed which consist of a Light Emitting Diode (LED) which sends light

into each PM tube and a PIN diode. By comparing the PIN diode signal to the PM tube signal the gain of the PM tube can be monitored. Each time a flasher is activated a trigger is created and when the PLU receives this trigger again readout is enabled immediately.

- **The Pb Glass Trigger:** This trigger can only be activated during tagging efficiency runs when the Pb glass detector is placed in the photon beam. When it detects a photon a trigger is generated and readout is immediate.

When a trigger is raised the PLU disables or latches its inputs and the inspection of events is put on hold while the PLU is strobed and the output conditions generated. There are three main output conditions:

- **Immediate Interrupt:** If a Cosmic, Flasher or Pb glass trigger is present then the relevant detectors are provided with ADC gates. No further processing of the event is required and the data acquisition computer is interrupted and the ADC's are read out enabling the event to be stored.

- **Activate 2nd Level:** If the PiP particle trigger is raised, the ADC gates are generated but the interrupt of the acquisition computer is delayed. Instead the second level trigger circuit is activated.

- **Reject:** If more than one trigger was present, which is an unlikely occurrance, then the event is rejected and the system reset to process the next event.

3.6.3 Second Level Triggers

The second level triggers are activated once a charged particle entering PiP has been identified. The 2nd level triggers correspond to more complex conditions which take more time to establish. The 2nd level PLU decoder is shown in figure 3.17, it is similar to the first level decoder.

The four main 2nd level triggers are:

- **Electron Reject:** Due to atomic (γ, e) process a large number of low energy atomic electrons enter PiP. These events are of no use and if read out would

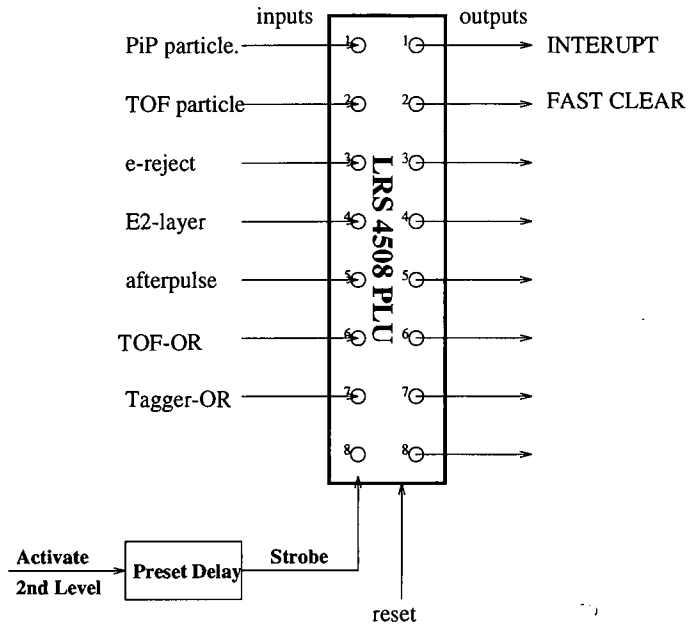

Figure 3.17: *The 2nd level trigger*

swamp the data. To counteract this they are rejected by means of a ΔE-E cut in the hardware. This is done by demanding that a weighted sum of the PiP ΔE and E1 signals is above a certain discriminator threshold. If a signal is however received in the E2 layer this cut is overridden as the E1 signal is no longer proportional to the particles total energy.

- **TOF-OR:** A large proportion of events with a particle in PiP have no corresponding particle detected in the TOF array. The TOF-OR trigger is a gatted OR of all the 102 TOF bars. This requires a particle to be detected in TOF within 400ns of the initial PiP trigger. This selectivity greatly reduces experimental dead time.

- **Tagger-OR:** In order to reconstruct the photon energy, a prompt electron must be present in the Tagger Focal Plane Detector. The Tagger-OR is a gated OR of all 352 FPD elements. This requires an electron to be present within a 80ns PiP-Tagger coincidence window. At normal beam currents, the presence of randoms on the FPD means the chance of this trigger not being generated are extremely small.

- π^+ **Afterpulse Trigger:** This trigger is used for determining the presence of positive pions in PiP. Pions are identified from the generation of an afterpulse from the $\pi^+ \rightarrow \mu^+ \rightarrow e^+$ decay process. Once the PiP particle trigger has been raised the PiP E-blocks are monitored for the occurrence of an afterpulse. The inspect time was set at 6μs. The time the afterpulse occurred is recorded in a multi-hit long range TDC.

The second level PLU is strobed at a fixed time after the 1st level trigger. This time is to allow the second level triggers to be processed, in particular it depends on the inspect period required by the afterpulse trigger. The PLU is programmed to identify certain combinations of inputs and can decide between two output states:

- **Accept Trigger:** This means the event has an acceptable set of second level triggers present. An interrupt is issued to the data acquisition computer and the ADC's are read out. Once this is done the computer issues a reset to the circuit.

- **Fast Clear:** This means the event is rejected as one or other of the acceptable input states are not met. All ADC's are reset and the trigger logic is unlatched to allow a new event to be processed.

Different trigger requirements can be set depending on the nature of the run.

3.7 Data Acquisition

The data acquisition system controls and collects data from the electronics modules in the experiment. The acquisition system has three primary tasks. Firstly it must initialise the electronics modules and load programmable settings, e.g. discriminator thresholds. Secondly, it must read out data from these modules and lastly it must store this information in a useful format.

The data acquisition system used in the PiPTOF experiments is the ACQU data acquisition and analysis sytem [Ann95, Ann96]. ACQU is written in the C programming language and can handle both on-line data collection and off-line data analysis. The acqu software consists of two parts, a front end component which controls the experimental hardware, reads out data from ADC's and optionally stores the data, and a workstation based component which stores on-line data or reads and analyses off-line data.

The heart of the data acquisition system is the VME crate. This has an MC68040 based, single board computer, running the OS-9 operating system, which houses a VMEbus interface and 16 Mbytes of RAM. This executes the acquisition software while the VMEbus facilitates I/O between the computer and other interface modules, which provides a bi-directional link to the Camac and FASTBUS crate controllers [Ann93]. The bi-directional link serves to initialise and control the Camac and FASTBUS modules. The collected data can be filtered (pedestal subtracted, zero and overflow supressed) and then sent via an ethernet TCP/IP connection to a VAXstation outside the experimental hall. This VAXstation can perform online analysis and stores the data to disk/tape.

3.7.1 Acquisition Software

There are four main parts to the acquisition software running on the MC68040:

- **Supervisor:** This initialises the experimental hardware on the basis of information read from user-edited parameter files specifying the desired electronic modules, their locations and initialisation data, e.g. threshold or pedestal values. It also starts child tasks, acqu, store and control, which run in a semi-independent manner.

- **acqu:** The acqu process handles the data read out from the ADC's. When an interrupt is received from the trigger logic, acqu proceeds to read out all the modules. The event data is a list of integer pairs giving the ADC index and its contents. On completion of readout, the acqu process unlatches the trigger and awaits another interrupt.

- **store:** The store process enables the data collected by the acqu process to be sent over the ethernet using the TCP/IP protocol to the online analysis workstation.

- **control:** This is started by the user and is used to pause or start/stop the acquisition system.

3.7.2 Data Analysis Software

In order to monitor the performance of an experiment it is necessary to perform some online analysis. This is performed on a VAXstation in the control room. There are three process run on the VAX:

- **vme_server:** This makes the network connection to the VME based MC68040 computer and receives data from it. The data is written to disk and is passed to the sort process for analysis.

- **sort:** This processes the ADC information on an event-by-event basis and produces spectra. Conditions may be applied to ADCs or derived values and these can be used to monitor the performance of the experiment.

- **control:** This displays the spectra that are produced from the sort process.

The above system is the same as the one used in the offline analysis.

Chapter 4

Detector Calibration

After the experiment is completed all that is left is a large collection of data tapes containing vast quantities of raw information. This information is in the form of ADC indices and their contents for every event. The purpose of the detector calibration process is to convert this raw data into useful physical quantities. The ADC's can be of two distinct types, QDC's which can store a digitised version of the pulse height of a photomultiplier tube, which enables a determination of the particle's energy, and TDC's which can record the time of a pulse relative to the reaction start time, which can enable a determination of a particle's hit position and thereby angle relative to the target. In this chapter the calibration techniques that were applied to the different detectors in the experiment are discussed.

4.1 General Concepts

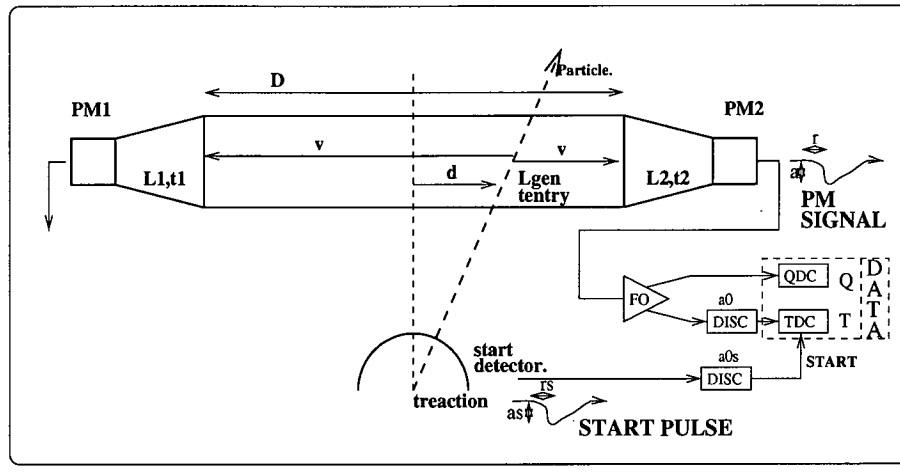

Figure 4.1: *Notation relating to a scintillator block*

Figure 4.1, shown above shows a typical scintillator block. The quantities used in this chapter are defined below. The subscripts 1,2 refer to the different ends of a block.

Constants:	D	-	Length of the block.
	v	-	Velocity of light along the block
	r_1, r_2	-	Pulse rise times (TDC's)
	$a0_1$, $a0_2$	-	Descriminator thresholds (QDC's)
	p_1, p_2	-	Pedestals (QDC's)
Raw Data:	Q_1, Q_2	-	QDC values in channel space
	T_1, T_2	-	TDC values in channel space
Derived:	a_1, a_2	-	Pulse heights (QDC's)
	L_{gen}	-	Light generated by particle in the block
	t_1, t_2	-	Time of PM pulse relative to reaction time
	t_{tof}	-	Time of flight of the particle
	d	-	Hit position relative to the block center

4.2 Generic calibration of a block

4.2.1 Pedestal subtraction

The QDC value that is obtained from the PM signal is not linearly proportional to the pulse height. There is a constant offset, called the pedestal value which arises due to the fact that there is a constant DC input current in each QDC. This pedestal value must be obtained for each QDC and subtracted from the raw value. Thus the pulse height a, is related to the QDC value Q, via:

$$a = Q - p \tag{4.1}$$

Where p is the pedestal value. The pedestal values are determined from special runs in which no hardware window is set.

4.2.2 Discriminator Thresholds

Before a TDC stop is generated the signal in the PM tube must exceed a preset discriminator threshold. The thresholds enable a reduction in the low energy background and the removal of electronic noise but are set as low as possible to widen the acceptance of the detectors for low energy particles. Threshold values are required in order to perform discriminator walk corrections which are required in the PiP-TOF TDC's. The threshold vaule for each TDC can be determined by plotting the associated QDC pulse height spectra under the condition that the associated TDC has valid data.

4.2.3 Discriminator Walk Corrections

The stop signals in the TDC's, generated when the input exceeds the discriminator threshold were derived from leading edge discriminators. In these type of discriminators the time recorded is dependent on the signal amplitude. This is shown in figure 4.2.

If a large and a small pulse arrived at the same time the small pulse would appear to have arrived later since it takes longer to reach the constant threshold. This is known as the walk effect, but can be corrected for by using the following:

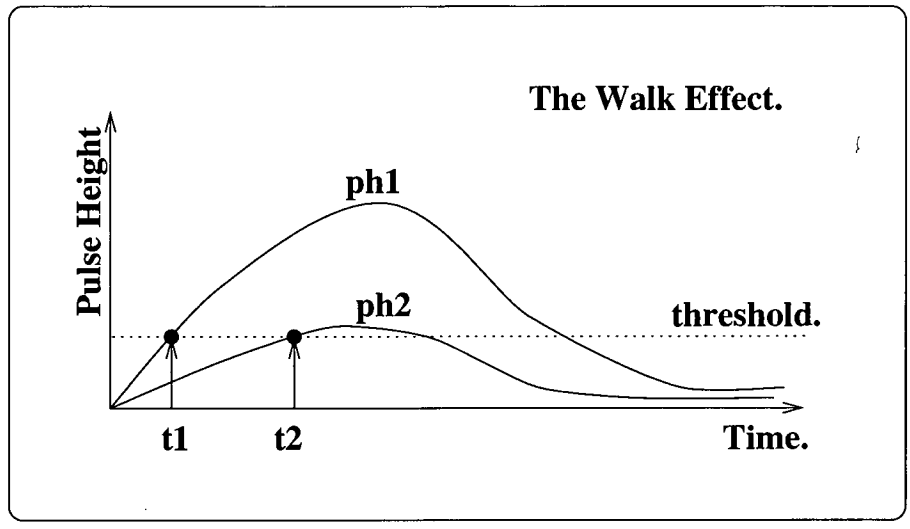

Figure 4.2: *The Walk effect*

$$T' = T + r(1 - \sqrt{\frac{a_0}{a}}) \tag{4.2}$$

Where T' and T are the corrected and uncorrected times (in TDC channels), a and a_0 are the pulse height and discriminator threshold (in QDC channels). r is the pulse height rise time, which is also obtained from the data but different methods are used for each detector.

4.2.4 Light Output

From the pulse heights a_1 and a_2 we must establish the total amount of light deposited by the particle in the block. Due to the fact that as the light travels in the block it suffers some attenuation, the amount of light collected at each end does not give the total amount of light generated. If the attenuation is assumed to be exponential with the distance travelled this leads to the following relation:

$$L_{gen} \propto \sqrt{a_1 a_2} \tag{4.3}$$

This states that the light generated in the block is proportional to the geometric mean of the pulse heights. In reality the attenuation of the light is not in fact exponential and a residual droop correction is required to account for the position

dependence in the geometric mean. This gives us the relation:

$$L_{gen} = constant \times \frac{\sqrt{a_1 a_2}}{f_{droop}(d)} \tag{4.4}$$

The droop function along with the calibration constant is obtained from the data.

4.2.5 Particle Energy Losses

All the particles detected in the experiment will have suffered an energy loss as they travel from the target to the dectector and also as they travel between dead layers in the dectector. This energy loss is calculated by use of the range method. The particle range, R, in a given material is:

$$R = aT^k \tag{4.5}$$

, where T is the particle kinetic energy and the coefficients a and k were found for each particle type and material by use of a GEANT [Bru82] simulation. If T_i is the initial particle energy and d is the distance the particle travels in the material then the energy loss is given as:

$$R_i = aT_i^k \tag{4.6}$$

$$R_f = R_i - d \tag{4.7}$$

$$T_f = (\frac{R_f}{a})^k \tag{4.8}$$

$$E_{loss} = T_i - T_f \tag{4.9}$$

In practice we have knowledge of the particle's final energy and we sum up all the energy losses along the particle track back to the reaction vertex to obtain the original energy of the particle.

4.3 The Start Detector

The PiP side of the ΔE-ring, which is known as the start detector, is of crucial importance to the whole experiment. All coincidence gates and TDC start times are generated from it. This start pulse should occur at a fixed time relative to the actual reaction start time, $t_{reaction}$. In practice, due to several factors, this does not happen. The three factors involved are the transit time of the particle between the target and the detector, walk effects at the discriminators and misalignments in the relative timing of the seven detector elements in the ring. The term Δt_{start} is defined as:

$$\Delta t_{start} = \Delta t_{flight} + \Delta t_{walk} + \Delta t_{align} \tag{4.10}$$

, which leads to the reaction time being related to the time of the startpulse via:

$$t_{reaction} = t_{startpulse} - \Delta t_{start} \tag{4.11}$$

The first of the corrections to $t_{startpulse}$, is the flight correction term, which depends on the variation of the particle's velocity over the energy range we are interested in. For pions between 20 MeV and 180 MeV this time difference is 0.3 ns and was thus neglected.

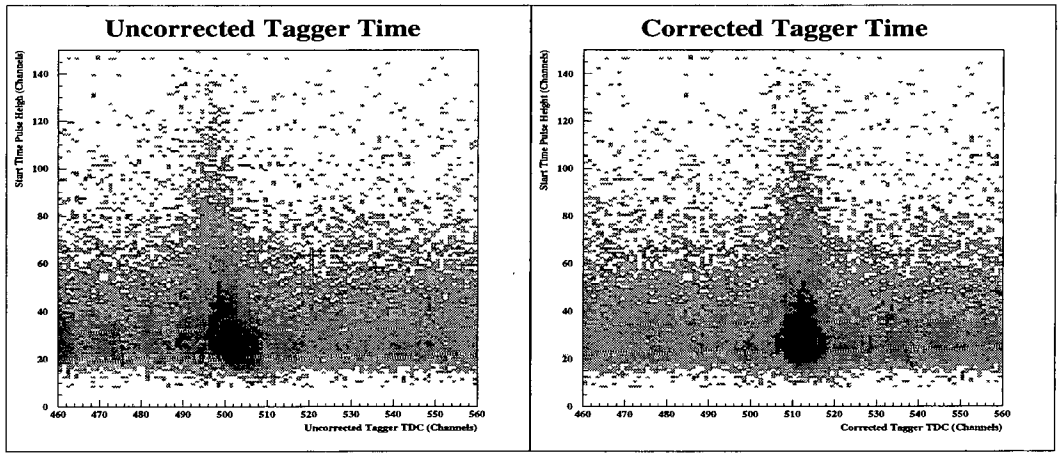

Figure 4.3: *Walk correction of the start detector*

The walk correction is established by plotting the pulse height from a start detector element against a tagger element TDC. The difference in transit times of

the photon, travelling from the radiator to the target, and the electron, travelling from the radiator to the tagger FPD, should be constant as both particles are relativistic. This is shown in figure 4.3 and it is apparent that there is a walk effect present. The tagger TDC walk is minimal due to the fact that high/low dual threshold discriminators are used, thus it is clearly the walk in the start detector element that is the main cause. The threshold is obtained and the rise time calculated to correct the walk. This procedure is performed for all the start detector elements and an offset, Δt_{align} is calculated to align the elements.

4.4 The Photon Tagger

The Glasgow photon tagger consists of 352 focal plane detectors to measure the energy of the electrons residual to the Bremsstrahlung at the radiator. The hit position of the electron along the FPD is dependent on the electron energy and the magnetic field strength of the bending magnet. The field strength is measured precisely by a Nuclear Magnetic Resonance (NMR) probe.

As well as a determination of photon energy the tagger also gives the time of the electron's arrival at the focal plane. The electrons that are correlated with photons causing a reaction form a coincidence peak in each focal plane element's TDC spectrum. This peak is sharpened by applying the start detector walk correction and the 352 elements are aligned to form a single peak. The flat random background results from electrons not correlated with the photons which induce reactions. The combined tagger time spectra is shown in figure 4.4

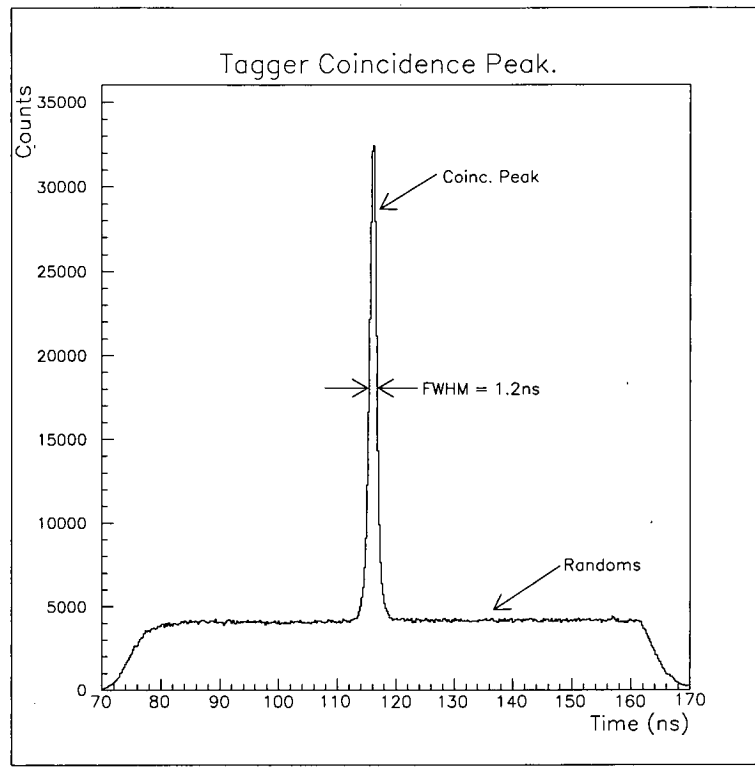

Figure 4.4: *The aligned tagger spectrum*

4.5 The PiP Detector

The PiP detector is used in the detection of positive pions. Pion identification is carried out by the afterpulse technique. The detected pion's energy is related to the light collected within the detector's scintillator blocks. The pion's position can be determined from the time difference between the signals in the PM tubes at either end of a block. From this position the pion angle can be calculated.

4.5.1 Position Calibration

The position of a particle hitting a PiP block relative to the center of the block is given by the time difference of the pulse at either end:

$$t_2 - t_1 = 2d/v + constant \tag{4.12}$$

$$d = (v/2) \times (t_2 - t_1) + constant \tag{4.13}$$

$$= [factor \times (t_2 - t_1)] + constant \tag{4.14}$$

d is the distance from the block center and v is the velocity of light in the scintillator. The constant reflects cable delays in the system.

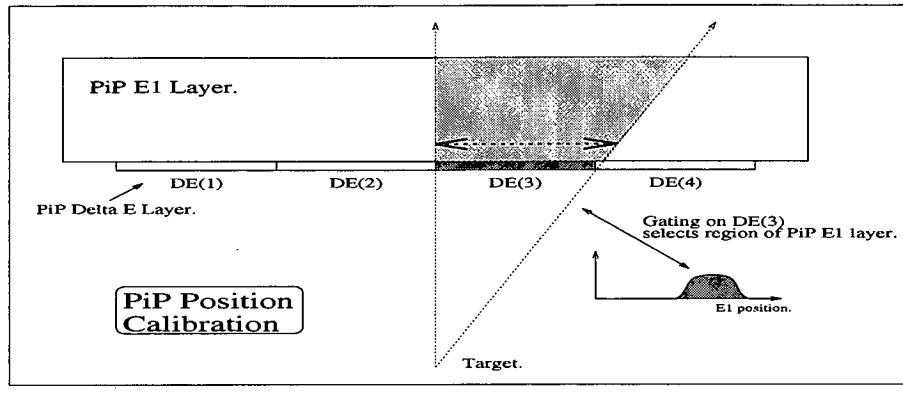

Figure 4.5: *ΔE gating for PiP position calibration*

The coefficients can be found by gating on each PiP ΔE element individually, and ploting the time difference spectra of a PiP E block, as shown in figure 4.5. The resultant spectra show, when plotted together, an overlap that indicates the join between two adjacent ΔE strips, the positions of which are known. This is seen in figure 4.6.

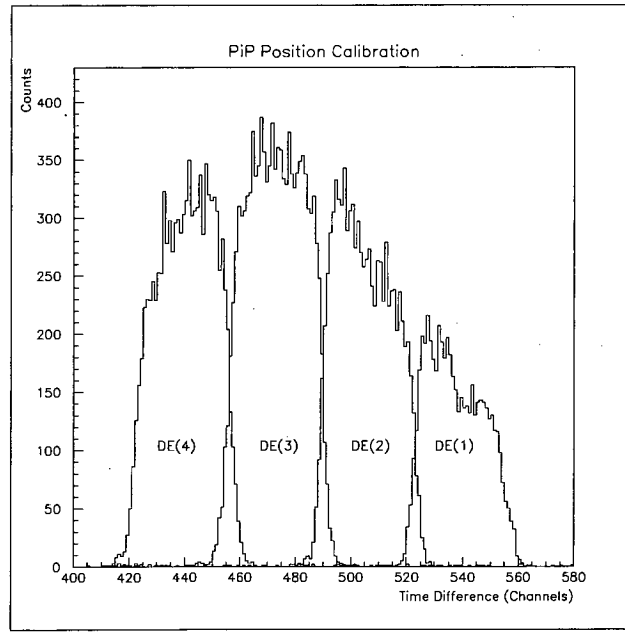

Figure 4.6: *Time difference spectra*

To calibrate the ΔE elements the reverse of this process is carried out, i.e. the blocks in the E1 layer are gated on individually which gives four overlaping spectra for each ΔE element. The calibration process gives horizontal and vertical information regarding the particle's hit position which can enable a determination of its trajectory and its spherical polar angles θ, ϕ.

4.5.2 Energy Calibration

An initial energy calibration for the PiP detector was done using cosmic rays. Cosmic rays are highly energetic, ultra-GeV minimum ionising muons. They travel downwards through the layers of PiP and a special trigger (see section 3.6) was used to record cosmic ray events alongside the reaction data. Only events that travel through a single layer are analysed and the path length, d, travelled by the cosmic ray through a block can be calculated from it's angle. Any dependence of the path length normalised pulse height mean, $\sqrt{a_1 a_2}/d$, against the position that the cosmic ray hit along the block is due to residual droop, so by plotting $\sqrt{a_1 a_2}/d$ against position the droop function f_{droop} can be determined. This is shown in figure 4.7.

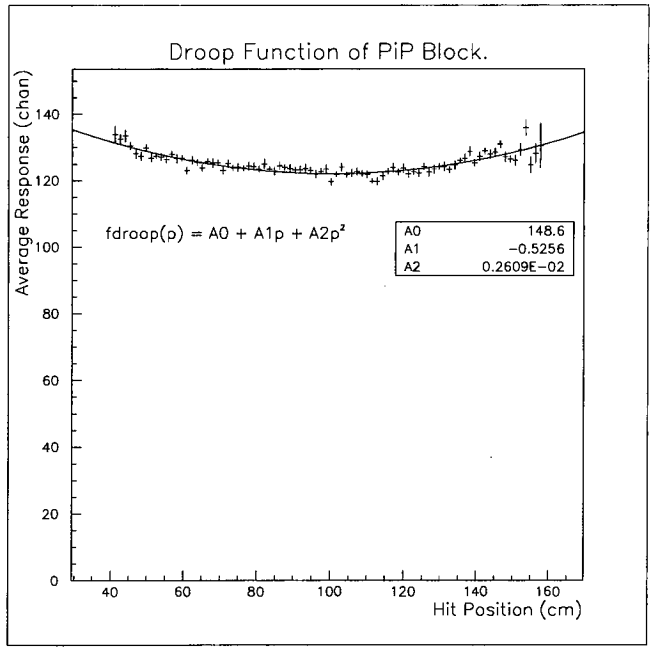

Figure 4.7: *Droop function of PiP block*

The droop corrected pulse height mean, shown in figure 4.8, has a characteristic Landau distribution. The light output half way up the leading edge of the Landau distribution is known to correspond to 1.87 MeV/cm. With this we can perform an initial energy calibration for the PiP detector. This energy calibration is later checked and refined by using the calibration data from the CH_2 target. Once the energy deposited in the final PiP layer is determined, the initial pion energy at the target can be found by working back along its trajectory to the target adding up all the energies deposited in preceding layers and calculating the energy lost in the dead layers.

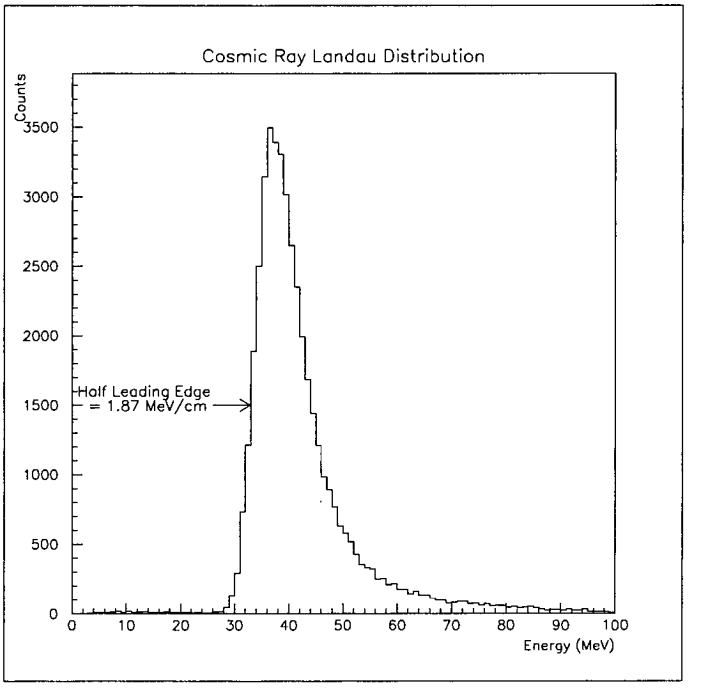

Figure 4.8: *Cosmic ray Landau distribution*

4.5.3 Pion Detection

Pions are mesons that can have charges +1,0,-1. The charged pion has a mass of 139.5 MeV and decays weakly via the process $\pi^{+(-)} \rightarrow \mu^{+(-)} + \bar{\nu}_\mu$ with a lifetime $\tau \sim 2.6 \times 10^{-8}$s. Identification of the positive pions in PiP was achieved in two stages. Firstly a ΔE-E plot is used to separate pion from protons and electrons, due to the fact that for a given energy E, particles of differing mass

deposit different amount of energies in the ΔE layer. An example of this type of plot is shown in figure 4.9.

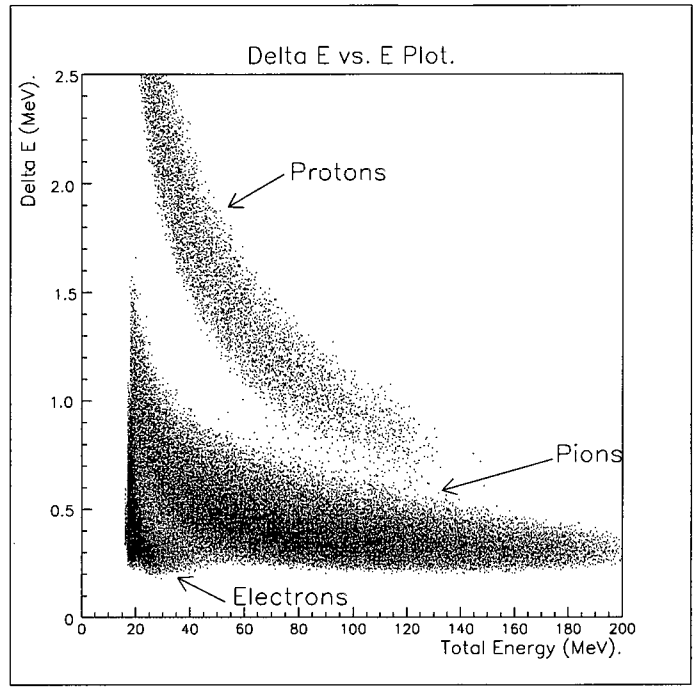

Figure 4.9: *Particle separation by ΔE-E plot*

The pion ridge contains both positive and negative pions. However these particles can be differentiated by means of their decay mechanism. The positive pion decays via:

$$\pi^+ \rightarrow \mu^+ + \nu_\mu \tag{4.15}$$

$$\mu^+ \rightarrow e^+ + \nu_e + \bar{\nu}_\mu \tag{4.16}$$

While the negative pions seldom are able to decay due to the fact that they are quickly absorbed onto nuclei in the scintillator material and release their mass-energy of around 140 MeV. At 26ns the lifetime of the decay of the positive pion into a muon is too short to be resolved by the detector. The positive muons decay into positrons with a lifetime of 2.2 μs and by demanding an afterpulse detector hit from these positrons the presence of a positive pion can be assured. These afterpulses are identified by means of a multi-hit long range TDC. After an initial pulse in the detector the TDC is started and left open for an inspect time of 6 μs.

Random afterpulses can occur during the inspect time but these are reduced by ensuring that there is no signal in the PiP side ΔE during this time, to prevent another particle from the target entering PiP and causing an afterpulse, and as we expect the pion to decay near to where it is stopped in the detector in the offline analysis the block in which the pion stopped and the block in which the afterpulse occurred can be compared and if they are not within the vicinity of each other the event can be rejected.

As a pion travels through the PiP blocks it interacts with the medium and loses energy through ionisation. This in turn produces the scintillation light which is measured and related to the pion's energy. From adding up all the collected light and determining the energy losses in dead layers it should be possible to calculate the pion's initial energy at the reaction vertex. However this fails to be the case if one or other of the following happens:

- **The pion does not stop in PiP:** This happens if the pion has enough energy to travel all the way through the detector, which corresponds to an energy of 180 MeV. Alternatively, a pion may scatter in the scintillator in such a way that it escapes outside the sides of the detector. In both these cases it is impossible to reconstruct the initial pion energy as the final pion energy is undetermined.

- **Inelastic pion scattering:** It is possible for the pion to suffer inelastic scattering from the nuclei that comprise the scintillator material, with energy being absorbed or released during the process. In this case the energy deposited in the material will not correspond to the initial pion energy.

The first problem is overcome by demanding an afterpulse, which guarantees the pion has stopped in the detector. The second problem is more complex and involves determining the predicted energy loss in each PiP layer and then on an event by event basis calculating the deviation from this. Any deviation from the predicted values of greater than the 20 % which can be accounted for by straggling should be considered to have come from a pion which has undergone some form of inelastic scattering and can consequently be rejected.

The predicted values were obtained from the calibration reaction $p(\gamma, \pi^+ n)$. This was used to obtain a sample of events where the detector response was as that predicted from the two-body kinematics, thus guaranteeing that there was no inelastic scattering. From this a plot of the path normalised energy loss in a layer was made against the incident pion energy. This removed any angular dependency. Figure 4.10 shows the response of the E1 layer for particles stopping in the E2 layer as a function of incident pion energy. In the analysis the polynomial fit of this is used to generate a predicted energy loss in the E1 layer given the total amount of energy deposited in PiP by the pion. If the difference between predicted and measured E1 energy loss is greater than a 20 % limit the event is regarded as having undergone inelastic scattering and is rejected.

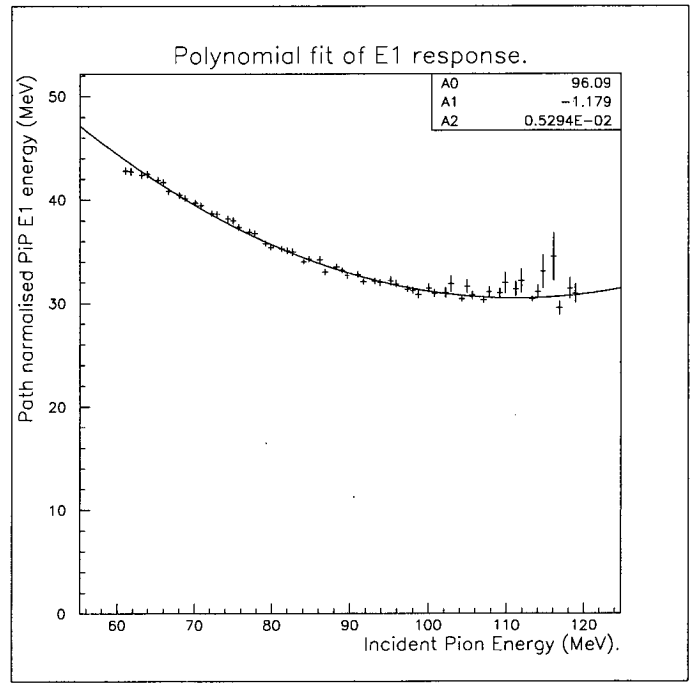

Figure 4.10: *Predicted response of E1 layer*

The PiP detector has been extensively simulated using the CERN library package GEANT by John MacKenzie [Mac95].

4.6 The TOF Detector

The TOF array is used to detect neutrons in coincidence with a pion in PiP. The polar angle of a detected particle is given by the position of the bar which it was detected in, while the azimuthal angle is given by the vertical hit position along the bar. The energy of the detected particle is obtained from its time of flight and thus timing measurements and walk corrections are of crucial importance. Neutrons are selected by means of the TOF side ΔE detector which enables a vetoing of charged particles.

4.6.1 Position Calibration

The position calibration of the TOF detectors is determined by plotting the time difference between signals at either end of a bar and then assuming that the ends of this distribution correspond to the actual ends of the bar. The actual position of each bar is measured precisely with an ultrasound device, which combined with the hit position along the bar allows the spherical polar angles of a hit to be determined.

4.6.2 TOF Walk Corrections

Before a determination of a particle's energy in TOF it is essential to calibrate the timing of TOF. Walk corrections of the TOF bars was performed by use of LED flashers which are installed in the array to monitor any gain drifts in the bars during the experiment. The LED flashers inject a pulse of light into each TOF PM tube while at the same time providing a TDC start signal. This gives a fixed time difference between when the light was emitted and when it was detected and the corresponding TDC spectrum displays a peak reflecting this. By varying the flasher intensity this peak is shifted due to walk in the discriminator. By plotting a bar's QDC against TDC this walk can be seen and the rise time can be extracted to correct for it. Figure 4.11 shows both the uncorrected and corrected ridge.

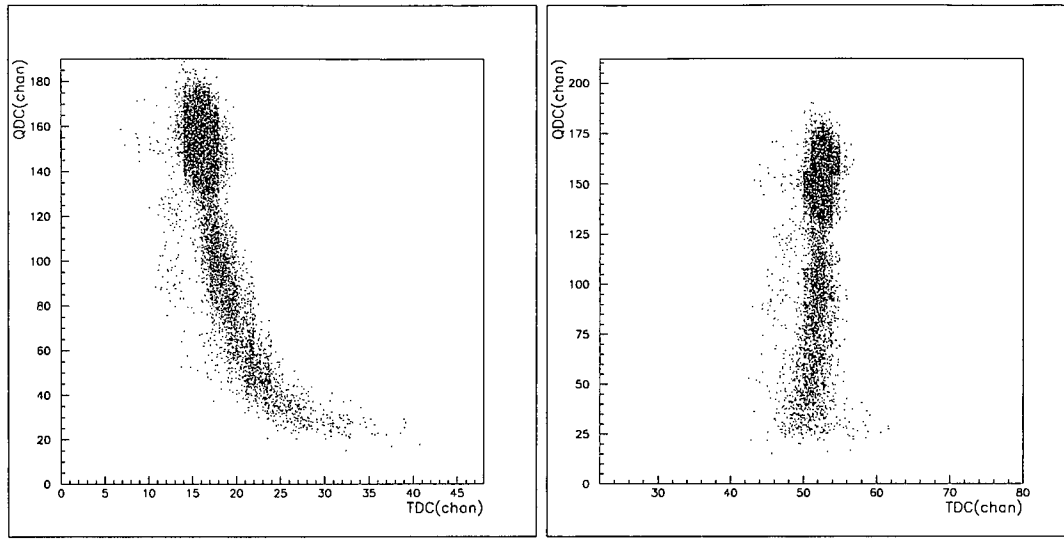

Figure 4.11: *TOF walk correction*

4.6.3 Time Of Flight

With the walk correction completed the particle time of flight from the target to the the TOF bar is given by:

$$tof = t_{mean} - t_{zero} \tag{4.17}$$

Where t_{mean} is the mean time from both PM tubes on a bar once walk and start corrections have been made and t_{zero} is the point in the t_{mean} spectra that corresponds to zero time of flight. This t_{zero} value for each bar can be obtained from the gamma flash corresponding to relativistic particles, which form a spike in a TDC spectra as they travel at the speed of light c. A plot of the quantity:

$$t_{cal} = t_{mean} - t_{start} - flightpath/c \tag{4.18}$$

projects the gamma flash onto the t_{zero} value and it can simply be read off from the spectra. Figure 4.12 shows a typical gamma flash spectra.

4.6.4 Energy Calibration

The kinetic energy of a particle, T, is related to its time of flight by:

$$\beta = flightpath/(tof \times c) \tag{4.19}$$

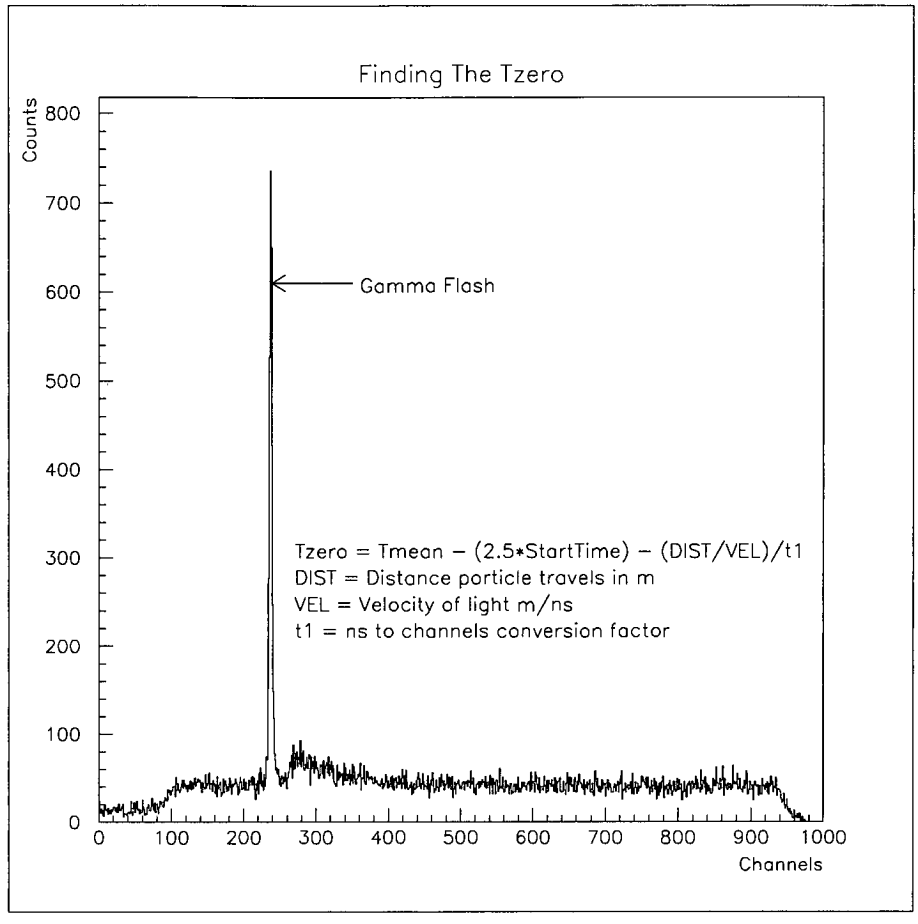

Figure 4.12: *Determination of t_{zero} from gamma flash*

$$\gamma = \frac{1}{\sqrt{1-\beta^2}} \tag{4.20}$$

$$T = (\gamma - 1) \times m_0 c^2 \tag{4.21}$$

Where m_0 is the particle rest mass. The above method while fine for neutral particles does not apply to charged particles as they interact with the air during their flightpath and lose energy, so the time of flight for them only gives an average energy.

The actual energy deposited by a particle while being of less importance than the time of flight is however required to determine the neutron detection efficiency. This efficiency depends on the threshold applied to the light output and a uniform threshold in MeV*ee* is required for all bars. This was achieved by finding the punch through energy for protons incident on the bars which should be at 78 MeV. A

plot of mean QDC vs mean TDC values shows this punch through point in terms of channel space enabling a calibration. An example of these so called sail plots is shown in figure 4.13. An alternative way of determining this calibration is in the use of an Am/Be radioactive source which provides gamma rays with a known Compton edge of 4.2 MeV.

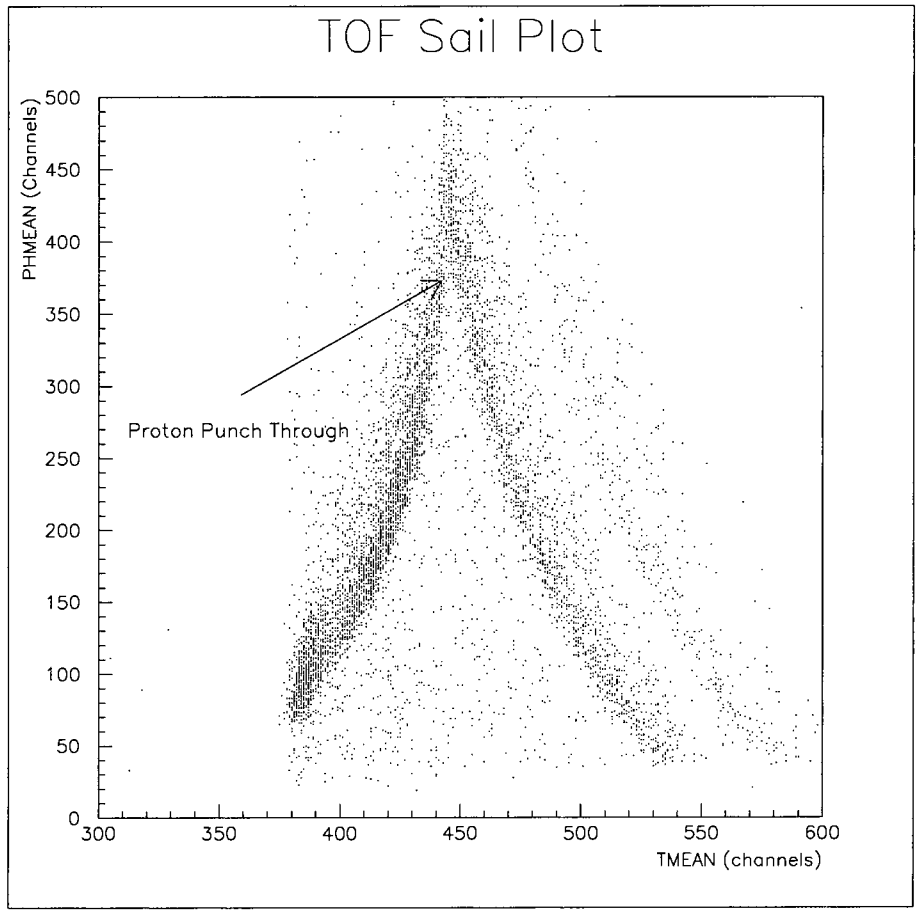

Figure 4.13: *Determination of the proton punch through point*

4.7 Detector Performance

By studying the free pion photoproduction reaction, $p(\gamma, \pi^+ n)$ it is possible to check and refine the calibration as well as to test the performance of the detector systems. This reaction was undertaken using a CH_2 target. The kinematics of the two-body final state are over-determined in that once the photon energy and

either the pion or neutron angle is known then the other kinematical variables can be derived by applying the usual conservation laws. It is this kinematical over determination that allows an independent check of the calibration, and by comparing measured and derived values, the energy and angular resolution of the detectors can be extracted. Ultimately, information from each detector is combined to form missing energies.

The resolution of the detectors is determined by plotting the difference of predicted and measured values. The error in the predicted value was determined using a Monte Carlo technique, i.e. given the error in E_γ and θ_n the error in E_π^{pred}, the predicted pion energy can be deduced. This error, σ_{pred}, is unfolded from the error in the difference, σ_{diff}, as obtained from the predicted minus measured spectrum, to give the actual resolution of the measured quantity:

$$\sigma_{meas} = \sqrt{\sigma_{diff}^2 - \sigma_{pred}^2} \tag{4.22}$$

4.7.1 Identifying Hydrogen Events

Before any resolutions can be determined, events from the $p(\gamma, \pi^+ n)$ reaction must be separated from reactions on the Carbon nuclei in the target. A spectrum of $\theta_n^{pred} - \theta_n^{meas}$, shown in figure 4.14, where the predicted values are calculated by means of the kinematics routine, shows a sharp peak at zero corresponding to reactions induced on the proton and background events corresponding to reactions on the Carbon. By cutting on this peak and a similar one involving a plot of $E_n^{pred} - E_n^{meas}$ it becomes possible to select a very clean sample of $p(\gamma, \pi^+ n)$ events.

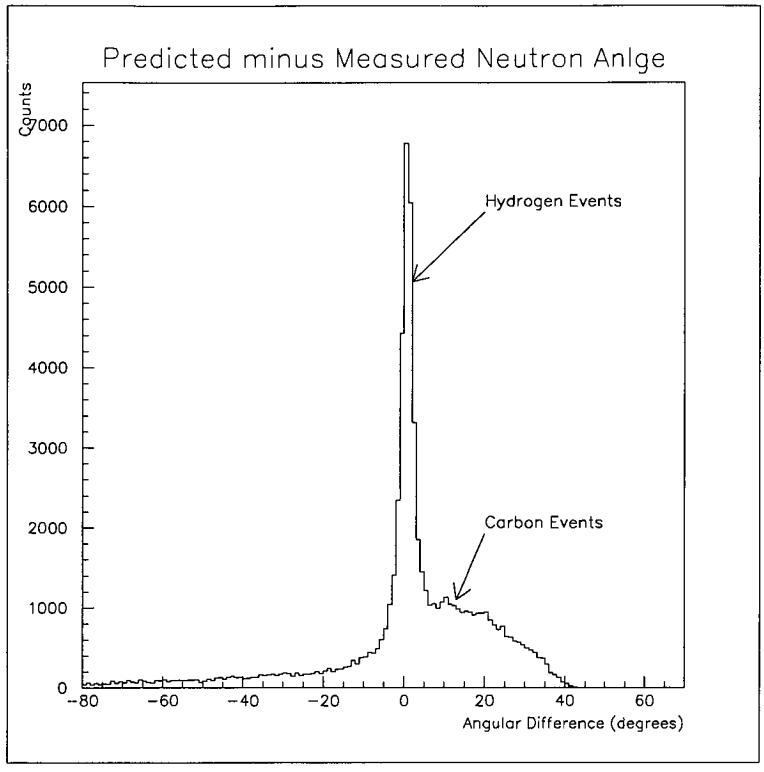

Figure 4.14: *Identification of Hydrogen $p(\gamma, \pi^+ n)$ events*

These cuts allow the predicted pion energy E_π^{pred} to be compared with the measured value E_π^{meas} for a sample of events that are guaranteed to have come from Hydrogen events, without any cut being made on the actual pion energy itself. By varying this technique it was possible to obtain calibration ridges and resolutions for all the kinematical variables.

4.7.2 Pion Measurement

Figure 4.15 shows a plot of the calibration ridge, E_π^{meas} against E_π^{pred}. As can be seen in the figure after an energy of around 180 MeV pions tend to punch through the entire detector and can no longer be detected. The overall pion energy resolution is found by plotting the difference between these two quantities as seen in figure 4.16. With a predicted pion energy resolution of 4 MeV, the measured pion energy resolution was determined to be 7 MeV FWHM.

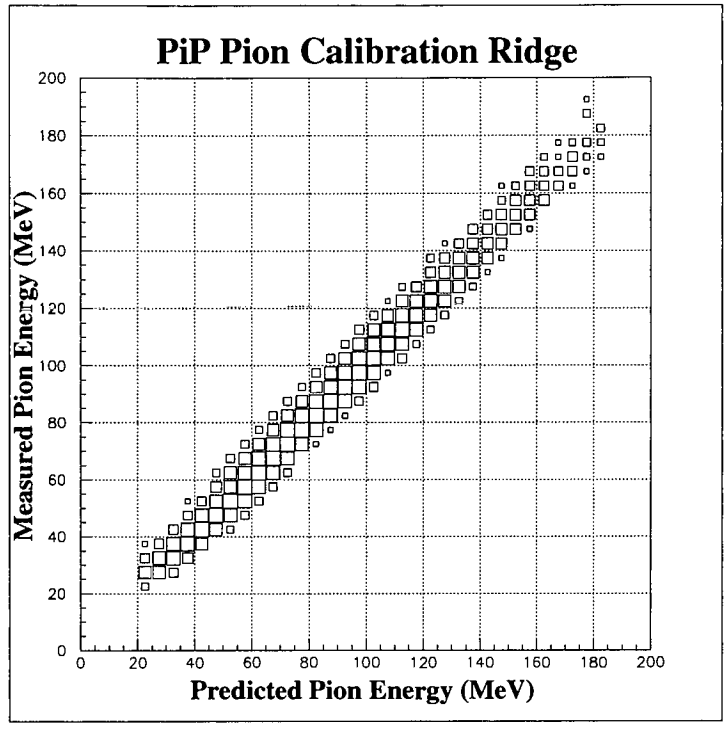

Figure 4.15: *The pion calibration ridge*

The pion angular resolution depends on the resolution of the particle hit positions in the ΔE and E layers of PiP. The polar angular resolution, $\Delta\theta$, is dependent on the position measured by the E layers which have a position resolution of 3cm, which at a distance of 50cm from the target, gives an angular resolution of $\Delta\theta_\pi \simeq 3^o$. The azimuthal angular resolution, $\Delta\phi$, is dependent on the position resolution of the vertical ΔE layers, which have a poorer position resolution of 9cm, leading to an azimuthal angular resolution of $\Delta\phi_\pi \simeq 10^o$.

4.7.3 Neutron Measurement

The neutron energy resolution can be determined in the same way as the pion energy resolution and leads to a neutron energy resolution of $\Delta E_n \simeq 3MeV$. The predicted minus measured neutron energy is shown figure 4.17. The neutron polar angle resolution is determined by the TOF bar width of 2cm and gives resolution of $\Delta\theta_n \simeq 2^o$, while again the azimuthal resolution is determined from the hit position resolution along the TOF bar.

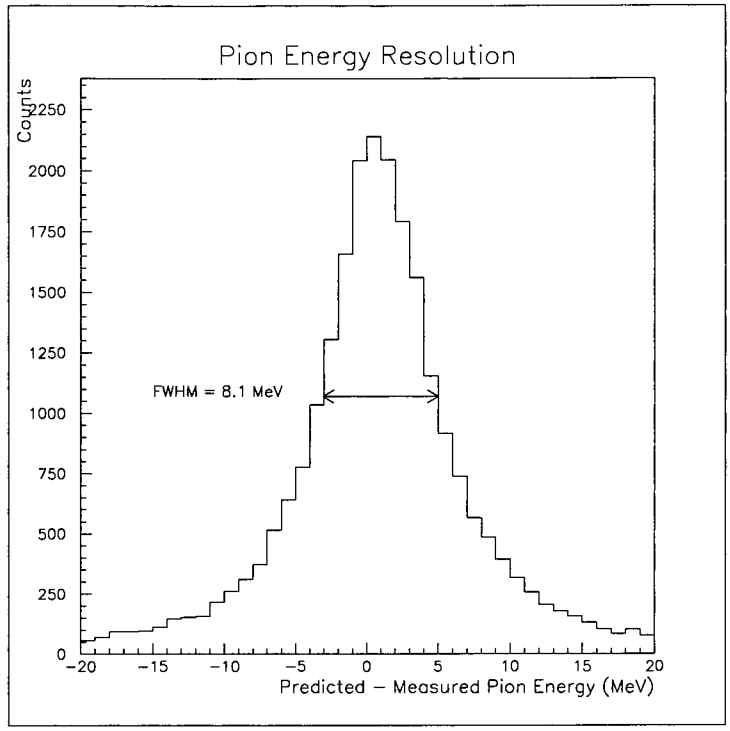

Figure 4.16: *The pion energy resolution*

4.7.4 Overall Resolution

The pion, neutron and photon energy measurements can be combined to form the missing energy, which is defined as:

$$E_{miss} = T_\gamma - T_\pi - T_n - T_{recoil} \quad (4.23)$$

$$= E_X + Q \quad (4.24)$$

For the calibration reaction, $p(\gamma, \pi^+ n)$, there is no recoil, and thus the excitation energy $E_X = 0$ and the missing energy is simply the Q value, which for the above reaction is:

$$Q = M_n + m_\pi - m_p = 140.8 MeV \quad (4.25)$$

The missing energy is shown in figure 4.18. The resolution is 8 MeV FWHM.

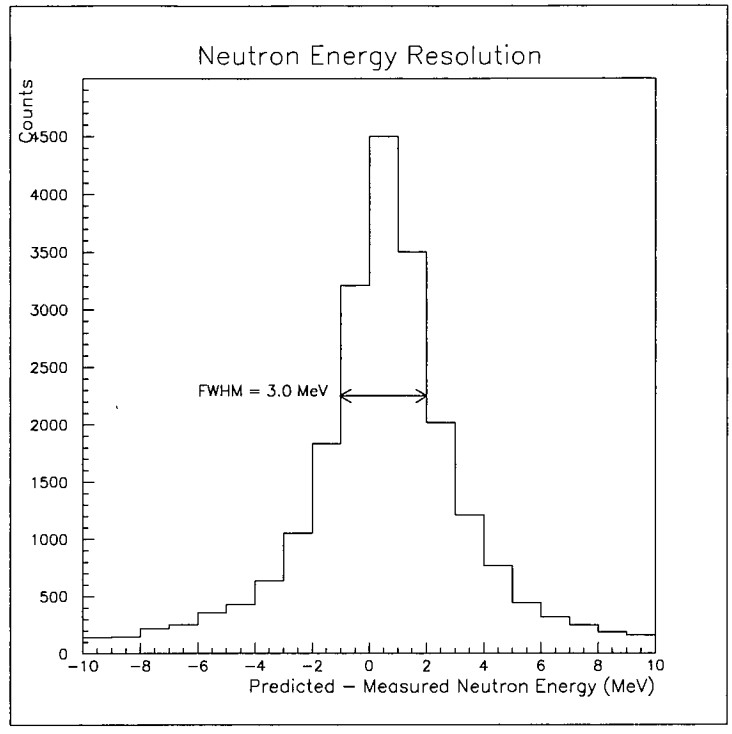

Figure 4.17: *The neutron energy resolution*

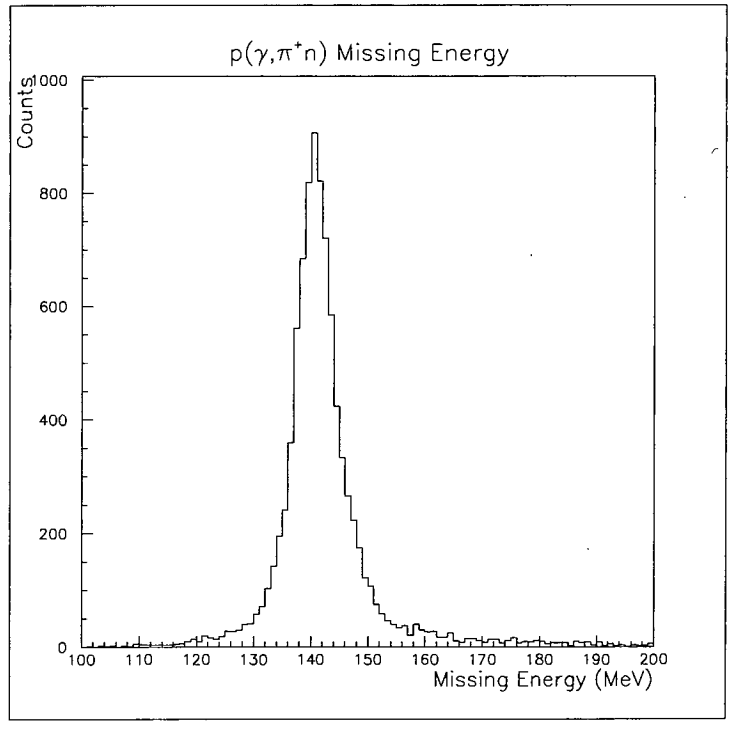

Figure 4.18: *The observed missing energy*

Chapter 5

Data Analysis

After the calibration procedure the next step is to extract the double and triple differential cross sections from the data collected. After selecting the π^+n channel, the various particle detection efficiencies have to be accounted for and random and background subtractions made. A knowledge of the photon flux and the target density are both also essential to make a determination of the absolute cross section measurement.

5.1 Analysis Code

The analysis was performed using the ACQU package [Ann95, Ann96], which was developed at the University of Glasgow. The ACQU code was written as a general code for the analysis of all experiments in the A2 PiP-TOF collaboration and performs tape handling, reduced data output and spectrum storage facilities. Code specific to a particular experiment must be developed by the user in the programming language 'C' in the form of user defined spectrum (uds) functions.

For the $(\gamma, \pi^+\mathrm{n})$ reaction a tree-like structure of code has been developed which starts with the scintillator blocks forming the basic constituents which then form layers in a particle detector. Finally all the detector information is combined to form the overall experiment. The code in this format is extremely efficient and loops round each block in a layer and then each layer in a detector and finally each detector in the experiment in turn.

The information contained in the ADC's and TDC's is analysed in this way with the array of calibration coefficients being included at this stage. The output then fills the data stucture ready for histogramming. At this stage the data was loaded into the CERN analysis package PAW++ [Paw95] for advanced analysis and presentational purposes.

5.2 Data Reduction

Out of the vast quantities of data obtained the aim of the data reduction process is to isolate those events that correspond to the exclusive $(\gamma, \pi^+ \mathrm{n})$ process. Although part of this is achieved in the hardware via the event trigger, the majority of the data is contamination from other reaction channels. It is however always safer to reject events in the offline analysis as the cuts can be unmade while a stricter hardware trigger runs the risk of rejecting desired events.

The first step in the reduction process is to remove the various calibration events such as cosmic ray and LED flasher events. This is achieved by simply reading the trigger type for a reaction event and rejecting the events with a cosmic or flasher trigger. The next stage is to identify positive pions in PiP and neutrons in TOF.

The pions are selected in PiP by cutting on the pion ridge in the ΔE-E plot, shown in figure 4.9. The requirement of an afterpulse which is demanded by the trigger selects positively charged pions. There is a large background of low energy electrons detected and in order to remove them a software threshold was applied to the pion kinetic energy, $T_\pi > 20$ MeV.

Neutrons can be selected via the fact that all particles produced at the target and entering TOF must travel through the TOF-side of the ΔE-ring. Charged particles generate a signal in this detector while neutral particles leave none and it is by demanding an absence of a signal in this detector that the selection of neutral particles can be made. Figure 5.1 shows the time spectrum of one of the ΔE elements, with the peak corresponding to charged particles. By demanding none of the elements have any particle hits in the peak a selection of neutral events can be made. Only hits in the peak are rejected as the random background is

due to uncorrelated randoms and their component underneath the peak actually causes true neutron events to be rejected. Photons, which are also neutral, can be rejected due to the fact that their relativistic nature gives signals that contribute to the gamma flash peak of the TOF spectra and by demanding a minimum TOF they can be rejected.

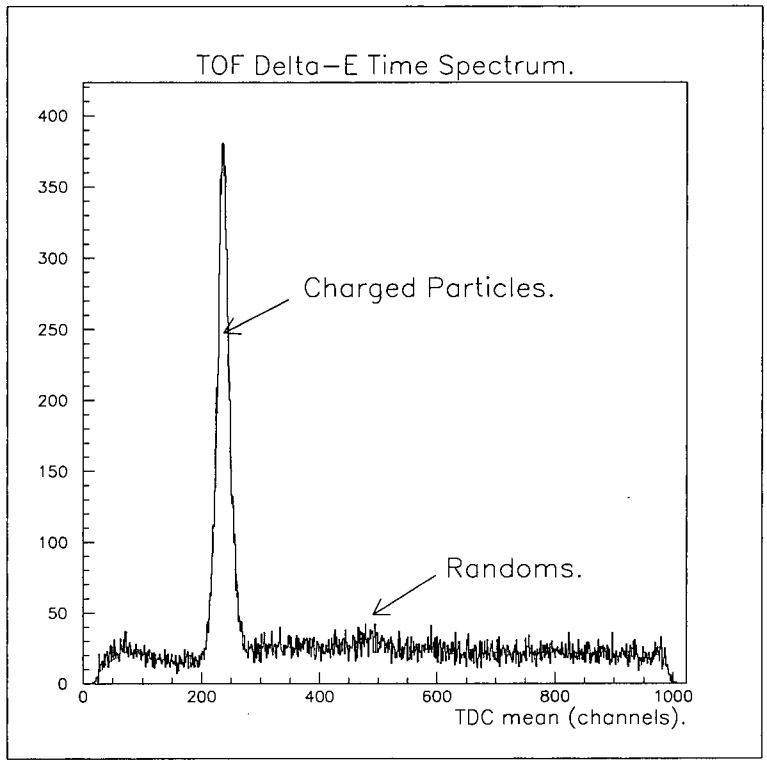

Figure 5.1: *The time spectra of a TOF-side ΔE element*

5.3 Random Subtraction

Although a positive pion and a neutron have been identified there still remains a residual contamination of the data by randoms and background. Randoms are detector hits uncorrelated with the reaction which generate erroneous triggers. The tagger has random electron hits which fire the focal plane detector elements. In TOF, random particles can fire elements of the array. While in PiP, random particles can generate random afterpulses, but these are greatly reduced due to the demanding of the position consistency of the afterpulse and as such were not dealt with. Even though correlated hits are selected, there remains a random component which must be subtracted. In order to achieve this a separate sample of random hits is required, which are given an appropriate negative weight and thus the total spectrum including events from prompt and random regions corresponds to the correlated hits alone.

5.3.1 Random Tagger Hits

Randoms in the tagger are caused by uncorrelated electrons being detected in the focal plane detector. The tagger time spectra has a peak corresponding to correlated tagger hits, events from this peak are labelled 'prompts' as can be seen in figure 5.2. There is a random component within this peak and to subtract this component two random regions are defined in the spectrum and hits in this region are weighted and subtracted from the peak events [Owe90]. The weight ascribed to a height is dependent on the relative size of the regions:

$$wgt^{\gamma}_{prompt} = 1.0 \tag{5.1}$$

$$wgt^{\gamma}_{random} = -\frac{1.0 \times \Delta T_{prompt}}{\Delta T_{random_1} + \Delta T_{random_2}} \tag{5.2}$$

The negative weight of the random events leads to spectrum entries originating from randoms in the prompt region being subtracted by entries coming from randoms in the random region.

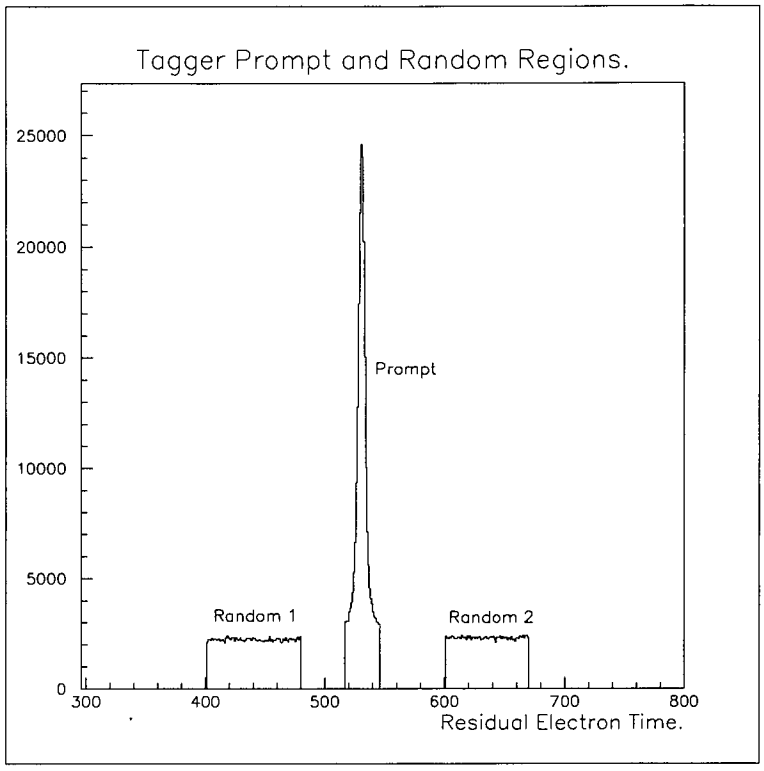

Figure 5.2: *Prompt and random regions in the tagger time spectrum*

5.3.2 Random TOF Hits

Randoms in TOF are dealt with in the same way as those in the tagger. The randoms can be seen as a flat background in the time of flight spectrum. The prompt and random regions are defined as shown in figure 5.3

Detector hits in the random region correspond to events beyond the valid time range, i.e. a neutron with such a large time of flight would have a corresponding energy of such a low energy that it would not be able to exceed the software threshold imposed on the detector pulse height. Hits in the random region have their time of flight shifted to bring them into the prompt region and these are then analysed in the same manner as those originally in the prompt region, except they are accorded a negative weight. The associated weights are in proportion to the time of flight windows:

$$wgt^{n}_{prompt} = 1.0 \tag{5.3}$$

$$wgt^{n}_{random} = -\frac{1.0 \times \Delta T_{prompt}}{\Delta T_{random}} \tag{5.4}$$

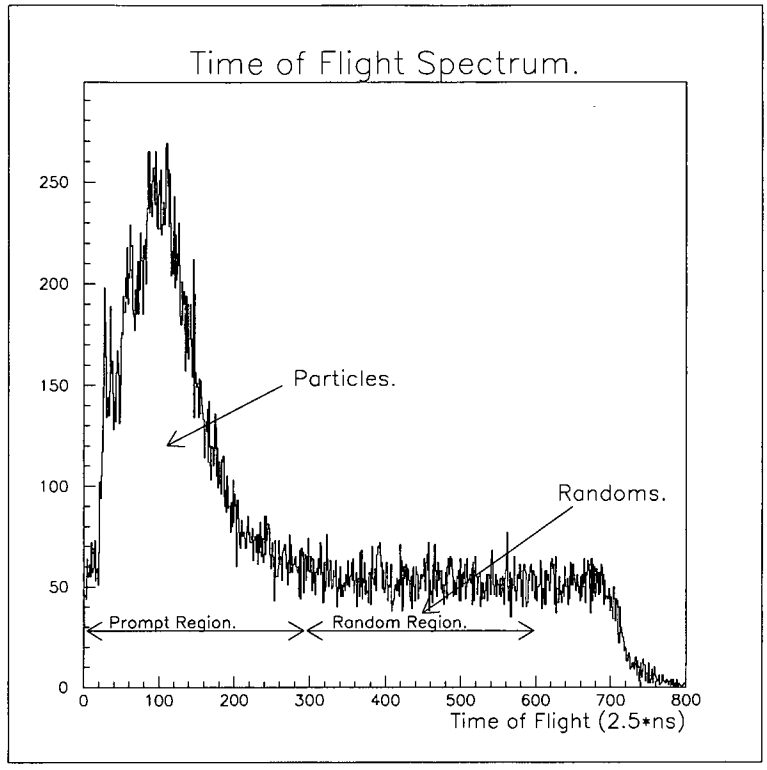

Figure 5.3: *Prompt and random regions in TOF*

5.3.3 Subevents

The existence of randoms cause multiple hits in each of the detectors, i.e. for every afterpulse in PiP there will be several hits in the tagger and several in TOF. These hits are combined, one from each detector, in all possible combinations to form what have been termed subevents. The number of Tagger, PiP and TOF hits is denoted as N_γ, N_π, and N_n respectively, while the number of subevents which can be formed is given by:

$$N_{subevents} = N_\gamma . N_\pi . N_n \tag{5.5}$$

Each subevent is analysed as if it were an independent event except that when spectra are incremented the weight the event is given corresponds to the weight of the hits which constitute the subevent:

$$wgt_{subevent} = wgt^\gamma . wgt^\pi . wgt^n \tag{5.6}$$

The detector weights are those discussed above and depend on whether the hit

was in a detectors prompt or random region. Spectra formed in this way are said to be random subtracted. Figure 5.4 shows the Helium missing energy spectrum with random subtraction.

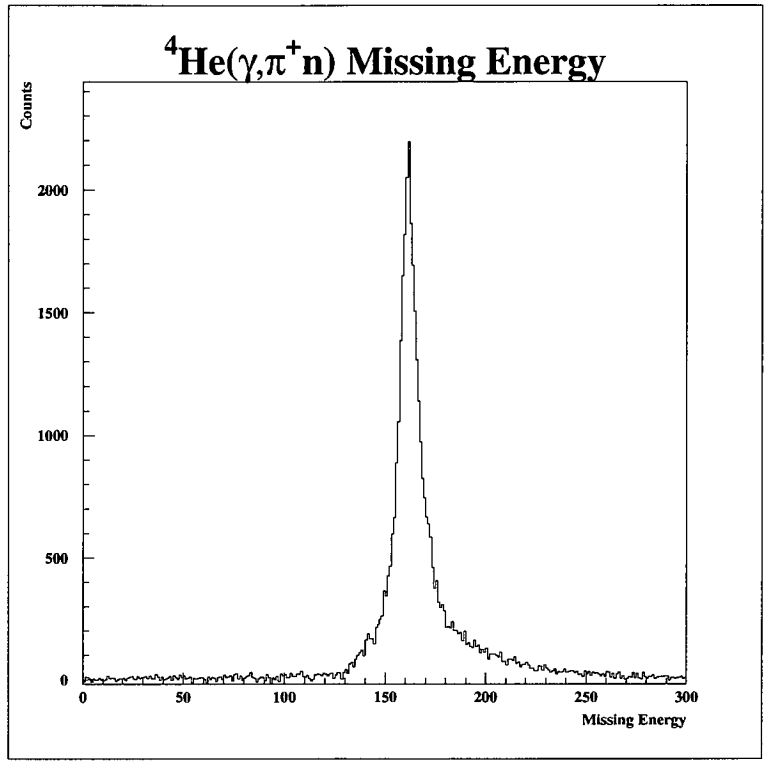

Figure 5.4: *Random subtracted Helium missing energy*

5.4 Detection Efficiencies

To obtain cross sections and have a meaningful comparison with theoretical results we have to obtain information on the various detectors' detection efficiencies. The previously described weighting procedure was found to be extremely useful in accounting for these various detection efficiencies. The efficiencies were calculated in different ways for each of the three detector systems and this section describes each of these in turn.

5.4.1 Tagging Efficiency

The method for obtaining the tagging efficiency, ϵ_{tagg}, has already been described in section 3.3.4. Shown in figure 5.5 is how the tagging efficiency varies with photon energy for both unpolarised and polarised photons.

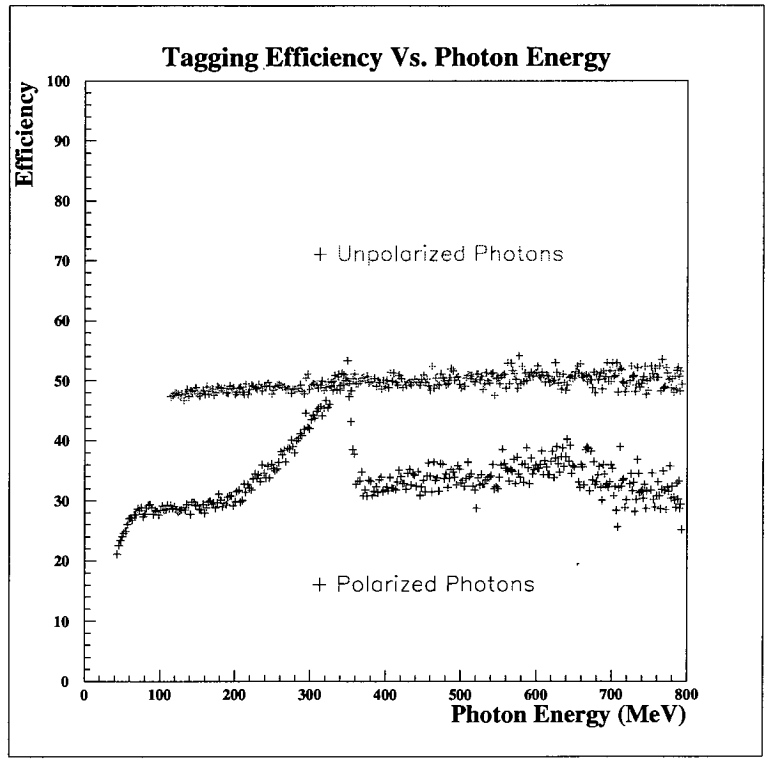

Figure 5.5: *Tagging efficiency versus photon energy*

The tagging efficiency of the unpolarised photons increases slightly with photon energy due to the fact that the higher energy photons form a smaller angular cone

than the lower energy photons. The tagging efficiency of the polarised photons rises to peak at the polarisation edge and then drops sharply, this again is due to the fact that the photons in the polarised region form a smaller angular cone than the photons further away from the polarisation edge.

In calculation of cross sections, the photon flux is derived from the number of electrons detected at the FPD elements multiplied by the tagging efficiency.

5.4.2 Pion Detection Efficiency

It is also neccessary in the calculation of cross sections to know what percentage of pion events are undetected either due to a lack of an afterpulse or because of inelastic scattering. This is known as the pion detection efficiency, ϵ_{π}^{+}, which is given by the probability that a pion generates an afterpulse, $P_{\pi+}$(afterpulse) multiplied by the probability that given an afterpulse was detected the pion had not undergone inelastic scattering, $P_{\pi+}$(clean). This is denoted as:

$$\epsilon_{\pi+} = P_{\pi+}(afterpulse \cup clean) \tag{5.7}$$

$$= P_{\pi+}(afterpulse).P_{\pi+}(clean|afterpulse) \tag{5.8}$$

Where $P_{\pi+}(clean|afterpulse)$ is the probability that the pion has not scattered given that there was an afterpulse.

The two probabilities were evaluated separately. Firstly, the probability of an afterpulse occurring, $P_{\pi+}$(afterpulse), was evaluated by using CH_2 data with the afterpulse trigger deactivated and events corresponding to the $p(\gamma, \pi^{+}n)$ reaction were selected by cutting on the predicted minus measured neutron energy spectrum. The number of events, N_{neut}, in the predicted minus measured energy spectrum was determined then the spectra was recreated for those events which generated an aferpulse and the new number in the peak denoted as $N_{neut}^{afterpulse}$ was determined. The probability of an afterpulse is given by:

$$P_{\pi+}(afterpulse) = \frac{N_{neut}^{afterpulse}}{N_{neut}} \tag{5.9}$$

The observed afterpulse efficiency is shown in figure 5.6 as a function of pion energy. The efficiency decreases with increasing pion energy, due to the fact that

as the energy increases the chance of a pion being inelastically scattered outwith the detector increases thus reducing the chance of it generating an afterpulse. The curve was fitted with a polynomial for use in the analysis.

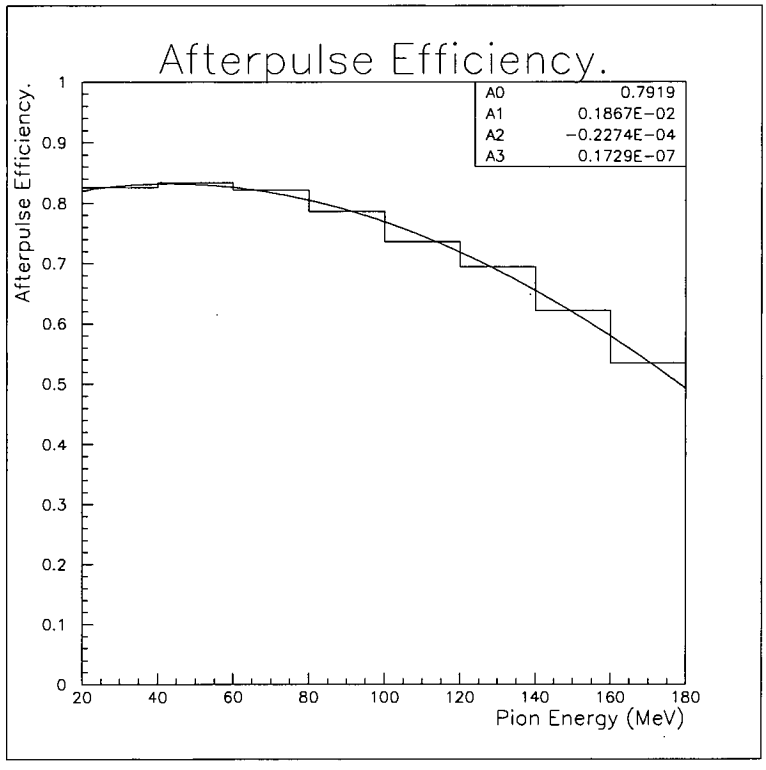

Figure 5.6: *Pion afterpulse efficiency plotted against pion energy*

The second quantity $P_{\pi+}(clean|afterpulse)$, was measured again using CH_2 data this time demanding an afterpulse. Hydrogen events were selected again using the predicted minus measured neutron energy spectrum. The number of neutrons in the peak was counted and denoted as $N_{neut}^{afterpulse}$. The proportion of events that had not undergone any scattering was found by counting the number of events in the peak of the missing energy spectrum, denoted $N_{\pi+}^{clean \cap afterpulse}$. The probability is thus:

$$P_{\pi+}(clean|afterpulse) = \frac{N_{\pi+}^{clean \cap afterpulse}}{N_{neut}^{afterpulse}} \tag{5.10}$$

The resultant detection efficiency is shown in figure 5.7. This curve is also fitted with a polynomial for use in the analysis.

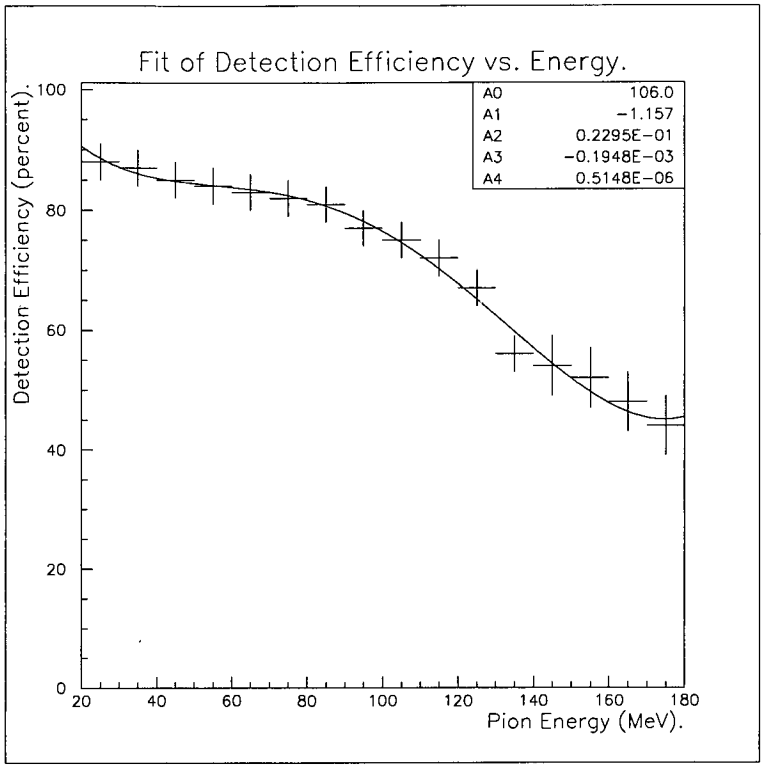

Figure 5.7: *Probability of inelastic scattering for afterpulse events*

5.4.3 Neutron Detection Efficiency

Because the neutrons are neutral they are not detected directly in TOF. This is due to the fact that neutrons do not ionise the scintillator material but instead they knock out protons in the material whose ionisation is subsequently detected. The neutron will only be detected if it knocks out a proton of sufficiently high energy to exceed the detector threshold. This leads to a relatively low neutron detection efficiency, ϵ_n, in TOF. In order to calculate the efficiency the Monte Carlo code STANTON [Cec79] was used. With a threshold imposed on the TOF bars of 5 MeV_{ee}, the results of the efficiency calculation is shown in figure 5.8. As can be seen from this the average neutron detection efficiency of a single bar is around 5%. To improve on this the stands were doubled up one behind the other.

Where a TOF stand has more than one layer, the neutron can pass through more than one bar. The efficiency for a single bar is denoted as ϵ_n^{bar} while the total efficiency for a stand of N layers, $\epsilon_n(\mathrm{N})$, can be derived from the reccurrence

relation:

$$\epsilon_n(N) = \epsilon_n(N-1) + \epsilon_n^{bar}(1 - \epsilon_n(N-1)) \quad (5.11)$$

$$\epsilon_n(0) = 0.0 \quad (5.12)$$

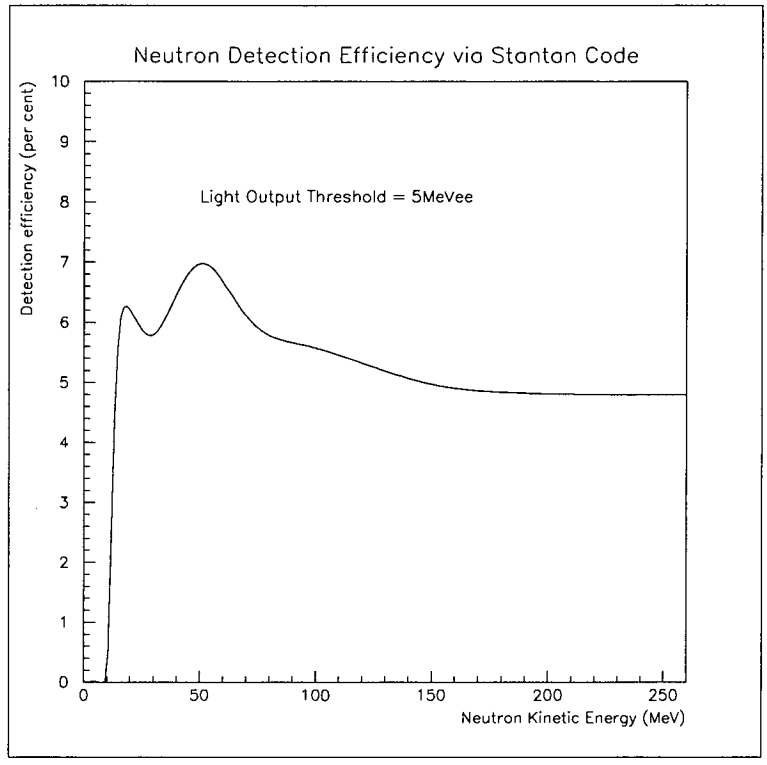

Figure 5.8: *Neutron detection efficiency for a TOF bar*

The efficiency also depends on the effective thickness that a bar presents to the particle which is angle dependent.

5.5 Determining the Degree of Polarisation

The photon asymmetry is defined as:

$$\Sigma = \frac{1}{P_\gamma} \frac{\sigma_{||} - \sigma_\perp}{\sigma_{||} + \sigma_\perp} \tag{5.13}$$

Where, $\sigma_{||}$ & $\sigma_\perp$, are the cross sections obtained with parallel and perpendicularly polarised photons respectively. While P_γ is the degree of polarisation.

When the electron beam strikes the diamond radiator, only a proportion of the produced photons are polarised, and there is still produced a fraction of unpolarised photons. Thus in determining the photon asymmetry it is of crucial importance to have a knowledge of the degree of polarisation, which is essentially the fraction of photons produced that are actually polarised in the correct orientation. This was determined by performing a Monte Carlo simulation, [Wun97]. The program calculates the relative intensity of the coherent and incoherent parts of the bremsstrahlung produced by the diamond lattice. This enables a calculation of the degree of polarisation. It is also possible to determine the degree of polarisation of the photon beam by means of a measurement. In coherent photo-production of π^0 mesons on ^{4}He, both the helium and the meson have zero spin, which means that the degree of linear polarisation of the photon beam is completely transfered to the azimuthal asymmetry of the produced π^0 mesons. This reaction had been performed at Mainz prior to our experiments by Kraus *et al.* [Kra97]. The results compare well with the calculations of the degree of polarisation. This shows that the production of linearly polarised photons by the coherent bremsstrahlung technique is a well understood process.

The degree of polarisation depends on several things:

- The required photon beam energy.
- The horizontal and vertical emittance of the electron beam.
- The orientation of the diamond crystal.
- The thickness of the diamond crystal.
- The temperature of the diamond crystal.

- The size of the collimator used.

An example of a calculation of the degree of polarisation is shown in figure 5.9. The plot shows that the highest level of polarised photons are within a 40 MeV region. The photons within this region were used in the determination of the asymmetry. It is also possible to see the contribution from other reciprocal lattice vectors in the smaller peaks at higher photon energies. The calculation gave an average degree of polarisation of 0.5 in the region $E_\gamma = 258 \pm 20$ MeV and 0.4 in the region $E_\gamma = 338 \pm 20$ MeV.

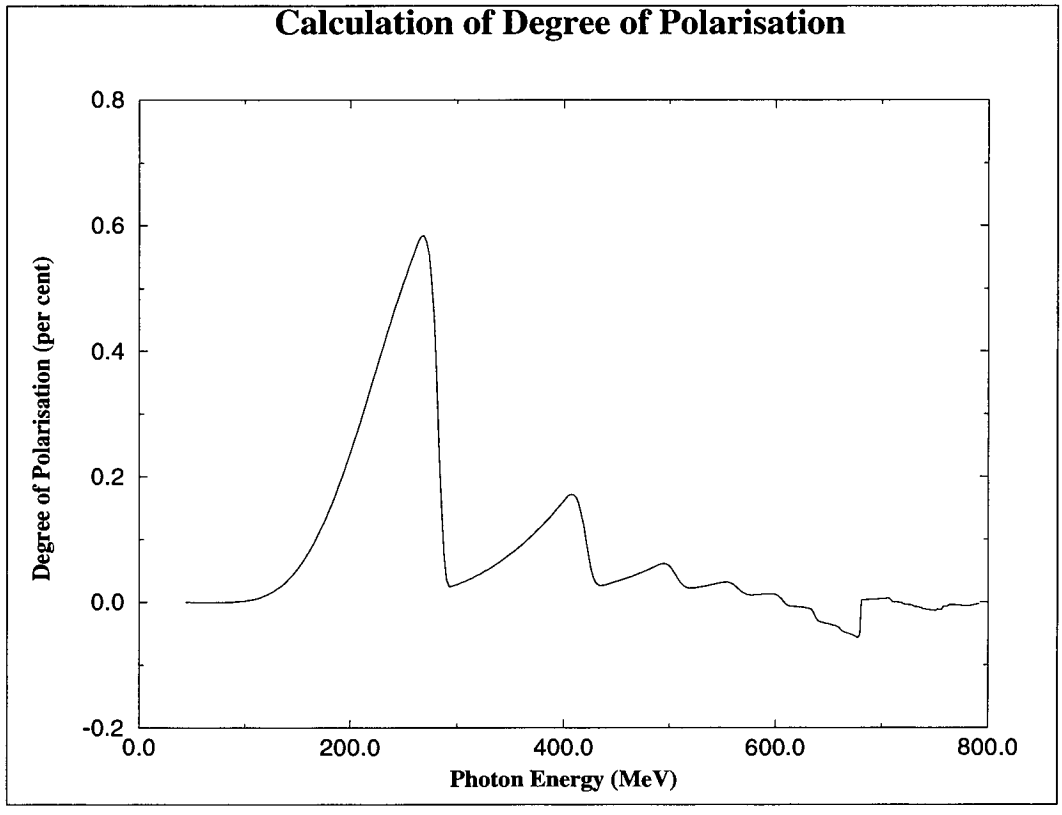

Figure 5.9: *Calculation of the degree of polarisation*

5.6 Derivation of Cross Sections

With the calculations of all weights and the determination of the efficiencies it is now possible to derive the cross sections. A reaction cross section is essentially the probability of the process occurring. This is found by determining the yield of reaction products under well defined geometrical conditions for a known incident flux of particles. The cross section, σ, is related to the yield, $\mathcal{Y}$, by the relation:

$$\mathcal{Y} = N_{\gamma}.n_{target}.\sigma \tag{5.14}$$

Where N_{γ} is the number of incident photons and n_{target} is the number of target nuclei per unit area which can be expressed as:

$$n_{target} = \frac{N_{A}.\rho_{s}}{A} \tag{5.15}$$

, where N_A is Avogadro's number, 6.02×10^{23}, and A is the atomic weight of the atom, while the quantity ρ_s is the target mass per unit area, the element of area being defined normal to the incident beam.

$$\rho_{s} = \rho.\frac{t}{sin\theta_{target}} \tag{5.16}$$

Where t is the target thickness and θ_{target} is the angle between the beam axis and the target plane.

A cross section has the dimensions of an area, the most commonly used unit is the barn where $1b = 10^{-28}m^2$. The reaction cross section is highly dependent on the energy of the incident particle and in the case of pion photoproduction shows resonant behaviour.

In practice what is measured is the differential cross section rather than total cross sections due to the fact that the detectors cover only a small region of space. In the case of the $p(\gamma, \pi^{+}n)$ reaction at a given incident photon energy, the kinematical quantities involved are the outgoing particles' kinetic energy and their spherical polar angles. The differential cross section at a specific pion polar and azimuthal angle, (θ, ϕ), is found by measuring the reaction yield, $d\mathcal{Y}$, for pions in the element of solid angle $d\Omega_{\pi}$:

$$\frac{d\sigma}{d\Omega_{\pi}} = \frac{d\mathcal{Y}}{N_{\gamma}.n_{target}d\Omega_{\pi}} \tag{5.17}$$

Which is measured in units of barns/steradian (b/sr). The element of solid angle, $d\Omega$, is defined in terms of the elements of polar and azimuthal angles in radians as:

$$d\Omega = sin\theta d\theta d\phi \tag{5.18}$$

For the free pion photoproduction reaction, $p(\gamma, \pi^+ n)$, the two-body final state means that once the pion angles have been specified the other quantities are determined while, in the case of the nuclear pion photoproduction reaction, $^4He(\gamma, \pi^+ n)$, the above kinematical constraints no longer apply due to the presence of the residual nucleus in the final state. An element of phase space in this case is defined by specifying five of the six kinematical variables and choosing the set T_π, θ_π, ϕ_π, θ_n, ϕ_n then the differential cross section is denoted by:

$$\frac{d^3\sigma}{dT_\pi d\Omega_\pi d\Omega_n} \tag{5.19}$$

Which is in units of b/MeV.sr^2. This triple differential cross section is a function of five variables, although due the system's azimuthal symmetry it depends only on the difference of the pion and nucleon azimuthal angles, rather than each independently. To plot this cross section, it is necessary to fix four of the variables and plot it as a function of the remaining one. This requires a lot of statistics as this selects a small region of phase space and only a small fraction of events fall into each bin. For this reason it was not possible to determine the asymmetry of the triple differential cross sections, but they were integrated over the pion energy to obtain the double differential cross section:

$$\frac{d^2\sigma}{d\Omega_\pi d\Omega_n} = \int \frac{d^3\sigma}{dT_\pi d\Omega_\pi d\Omega_n} dT_\pi \tag{5.20}$$

The detector threshold and the fact that the maximum pion energy that can be detected is 180 MeV means it is only possible to integrate over a specific range of energies. It is essential to state these integration limits if a meaningful comparison with theory is to be undertaken.

The double differential cross sections presented in this thesis have integration limits, $T_\pi^{min} = 20$ and $T_\pi^{max} = 180$ MeV, which are wide enough to cover almost all produced pions. Triple differential cross sections will also be made, though

with inferior statistics. The double differential cross sections were evaluated as:

$$\frac{d^2\sigma}{dT_\pi d\Omega_\pi} = \frac{\Delta\mathcal{Y}}{N_\gamma . n_{targ} . \Delta T_\pi . \Delta\Omega_\pi} \tag{5.21}$$

, where the yield was extracted from the data using weights to perform random subtractions and to account for the various detection efficiencies:

$$\mathcal{Y} = \sum_{events} \sum_{subevents} wgt \tag{5.22}$$

$$wgt = \frac{wgt_\gamma . wgt_\pi . wgt_n}{\epsilon_\pi \epsilon_n} \tag{5.23}$$

The photon flux during the experiment was typically of the order of 10^6 photons per second at each element in the focal plane. The number of photons, N_γ, was obtained from the tagger scalers combined with the tagging efficiency:

$$N_\gamma = N_{e'} . \epsilon_{tagg} \tag{5.24}$$

The quantitiy n_{target} was obtained for both the CH_2 and the Helium targets and is the number of atoms in the target. This is shown in table 5.1

Target	Atomic Wgt	Thickness (cm)	n_{target}
CH_2	14.01	1	$2 \times 1.150 \times 10^{23}(H)$
^{4}He	4.00	3	1.56×10^{22}

Table 5.1: Target Details

5.6.1 Hydrogen Cross Sections

To determine that the overall system was performing as expected, data from the CH_2 target was used to obtain differential cross sections for the free pion photoproduction reaction,$p(\gamma, \pi^+ n)$. The data was obtained by using polarised photons, but by averaging the parallel and perpendicularly polarised cross sections it is possible to obtain the unpolarised cross sections. The differential cross section was obtained for four photon energy regions, each 50 MeV wide, between 225 MeV and 425 MeV. It was plotted as a function of pion polar angle in the centre of

mass system, θ_π^*. The solid angle bins were defined by using 5^o CMS pion polar angle bins and one 30^o azimuthal angle bin.

The reactions on Hydrogen were separated from the Carbon events by requiring that particle energies and angles were consistent with two body kinematics. A cut was also made on the missing energy peak. The experimental cross sections were compared with the predictions of the Blomqvist-Laget free pion photoproduction operator [Blo77] which have compared well with previous data [Bet68, Mac95]. The comparison of the data and the theoretical predictions is shown in figures 5.10, 5.11. An overall normalisation factor of 1.16 was applied to all spectra to obtain maximal agreement between the data and the theory. This loss of events can reasonably be expected from events such as unaccounted dead time, rejection of events due to random contamination and pion decay before entering the PiP detector.

The general agreement between data and theory is quite reasonable, though admittedly there are some data points that are in particular disagreement. A possilbe explanation for this may be due to the fact that the pion detection efficiency is modelled by a polynomial but may in fact be more complicated due to various dead layers within the detector. The Hydrogen cross sections indicate that the detection systems were still functioning correctly after their original use in 1993 and give confidence in the Helium results which were obtained in an identical experimental setup.

The photon asymmetry is shown in figure 5.12. This is compared to previous data taken at Mainz by Krahn [Kra96].

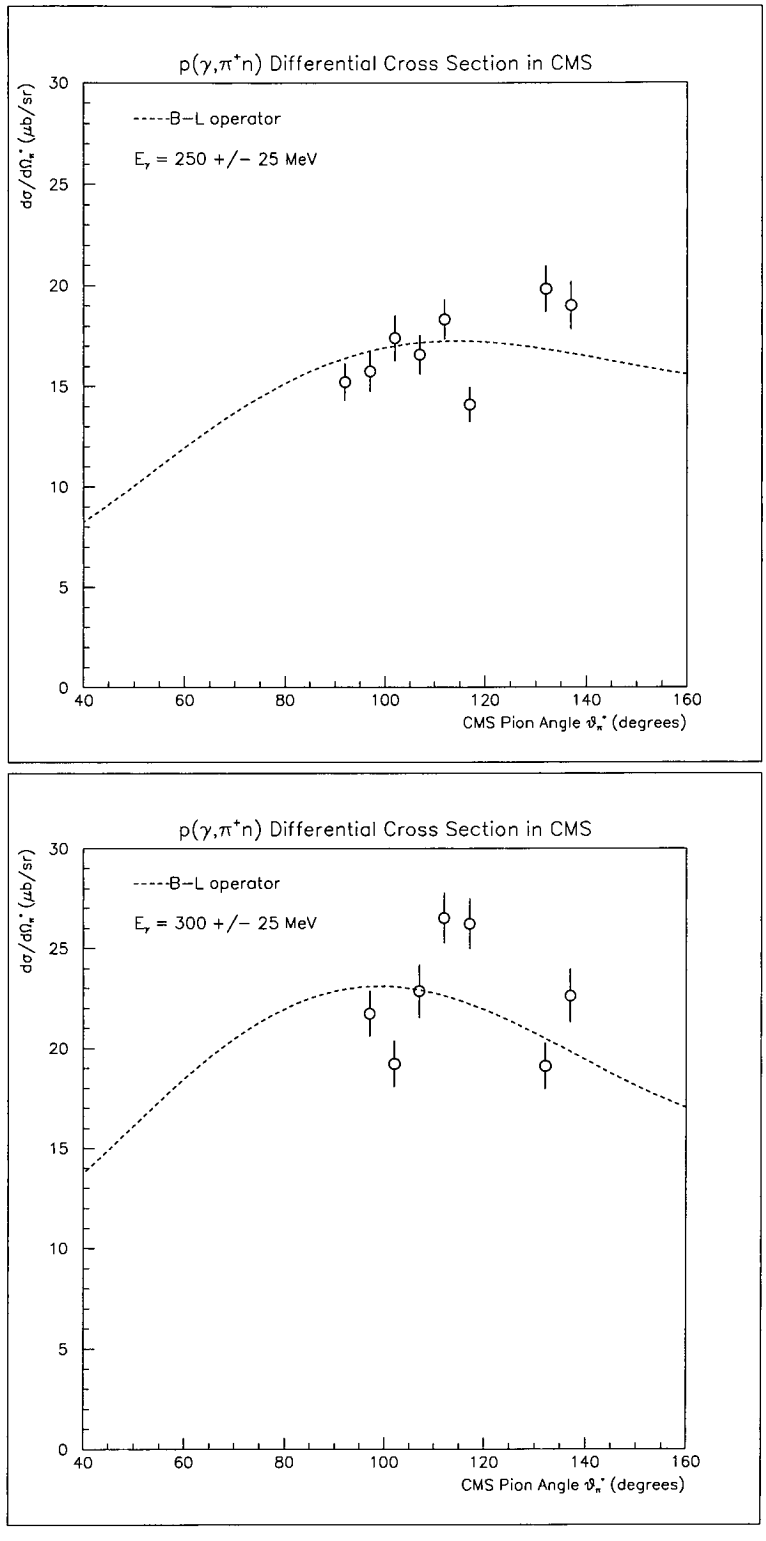

Figure 5.10: *Comparison of Hydrogen cross sections with theory.*

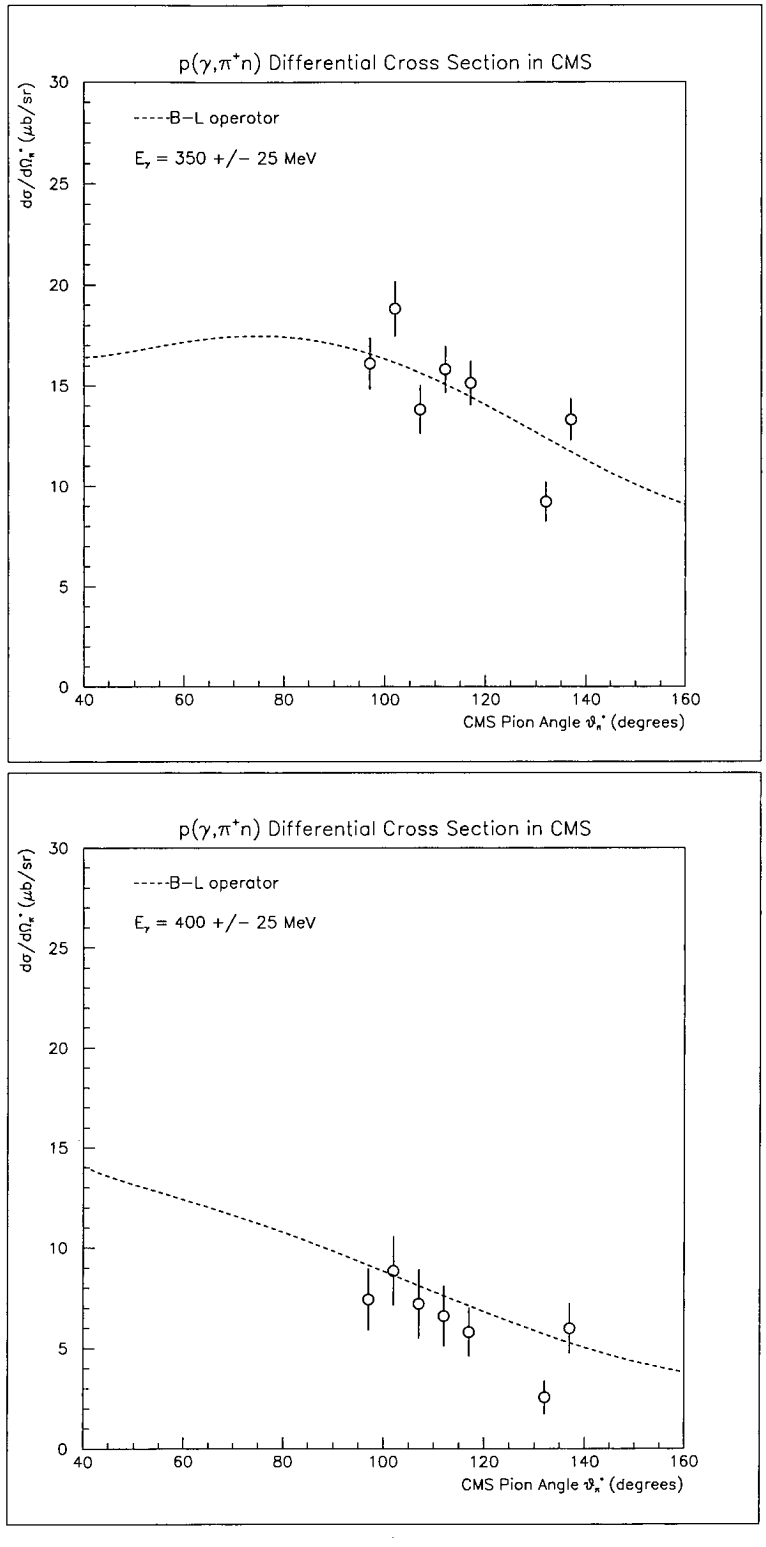

Figure 5.11: *Comparison of Hydrogen cross sections with theory.*

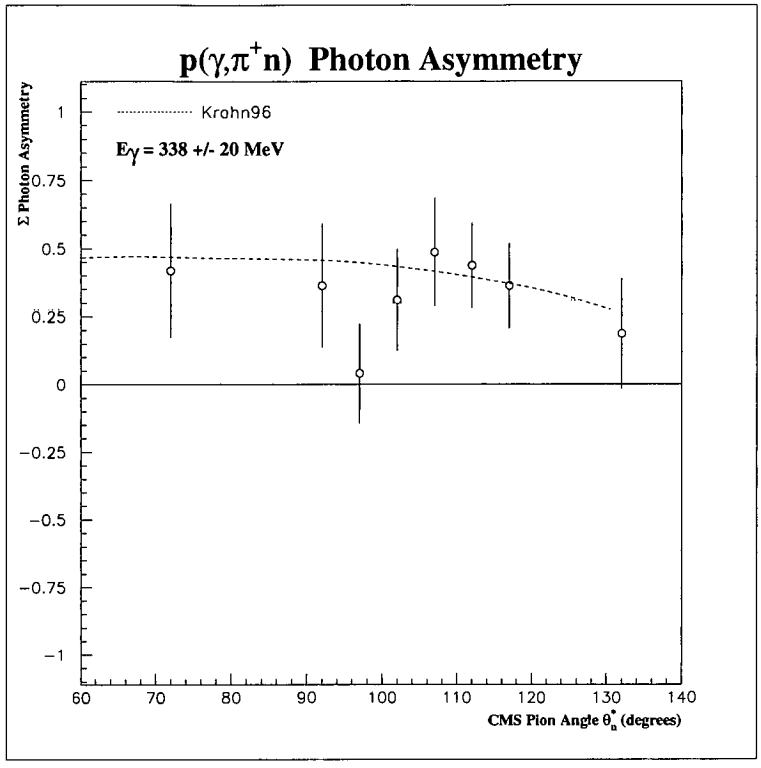

Figure 5.12: *Comparison of photon asymmetry with previous data*

5.6.2 Helium Cross Sections

The cross sections to be presented later represent the average differential cross section over the given energy and angular bins. The cross section was obtained for four photon energy regions, each 40 MeV wide, between 240 and 400 MeV. While the two photon asymmetries are presented at photon energies of 238 MeV and 338 MeV. The binning used is shown in table 5.2.

The last condition demands that the neutron is emitted approximately in the reaction plane defined by the pion. The integrated double differential cross sections were obtained by simply summing over all pion energy bins.

Target-out data was also taken and was analysed using the same cuts and bins as above. The missing energy spectrum, shown in figure 5.13, shows that Hydrogen was the main contributor to the background from the target. Because the actual data had a missing energy cut above the peak shown a lot of the target background was removed. Figure 5.14 shows a typical cross section measurement

Variable	Range	Bin Size	No. of Bins
T_π	20-180 MeV	10 MeV	16
θ_π	60-120^o	15^o	4
ϕ_π	(-15)-15^o	30^o	1
θ_n	10-150^o	5^o	28
$\phi_n - \phi_\pi$	170-190^o	20^o	1

Table 5.2: Binning choices used in obtaining Helium cross sections

for both the target-in and target-out data. The target-out contribution is only around 3% of the target-in data and was therefore neglected as it is much smaller than the systematic errors in the overall measurement.

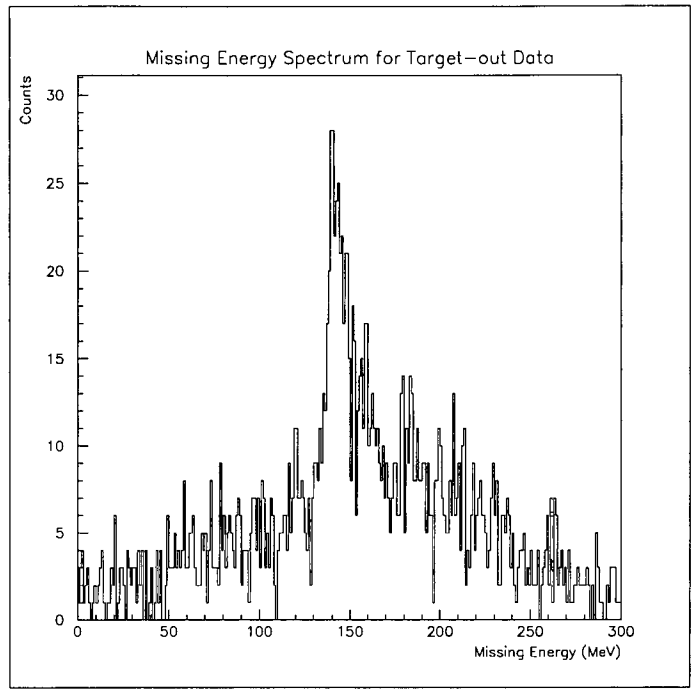

Figure 5.13: *Missing Energy spectrum for target-out data*

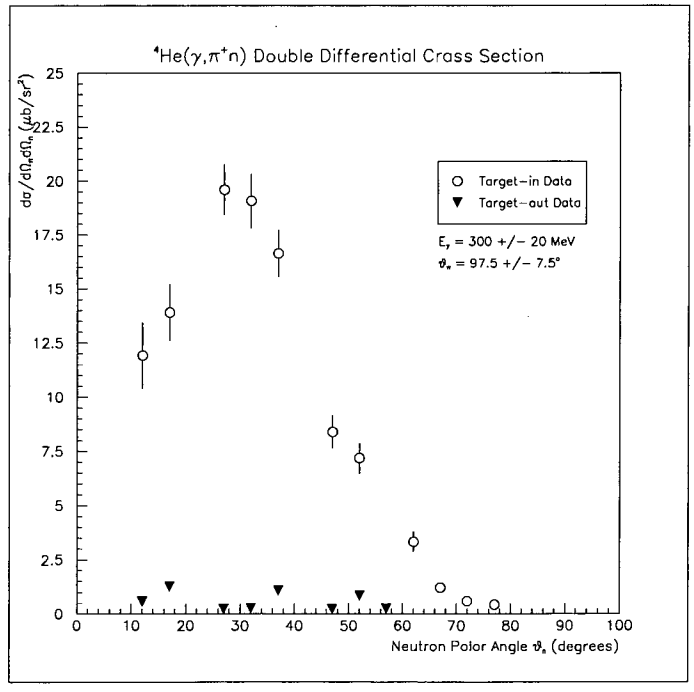

Figure 5.14: *Cross section contributions of targout out and in data*

5.7 Evaluation of Uncertainties

All experimental results must come with some estimate of the error associated with each value. This section looks at the various factors which contribute to the uncertainty in the results. There are two distinct types of error in the experiments, statistical and systematic and they arise from diffe rent factors.

5.7.1 Statistical Errors

Statistical errors arise from the fact that the experiment essentially measures the probability of something happen. The experimentalist needs to detect many events to accurately determine a reaction cross section. Thus the more events one has measured the less the statistical uncertainty will be. For N counts, the associated statistical error is given by $\sqrt{N}$. In the present experiment the events have been weighted in the experiment to allow for random subtractions and to compensate for detection efficiencies and this complicates matters somewhat. Instead of a number of counts there is a sum of weights:

$$W = \sum wgt \tag{5.25}$$

and the statistical uncertainty, σ_W, is given by:

$$\sigma_W = \sqrt{\sum (wgt)^2} \tag{5.26}$$

This reduces to $\sqrt{N}$ in the case where all the weights are unity. The size of the bins used to collect the data affects the level of statistical error. Thus to minimise the statistical error one can collect more data or use larger bin sizes.

The statistical error in the photon asymmetry, $\Delta\Sigma$, is given by:

$$\Delta\Sigma = \sqrt{\left(\Delta\sigma_{||} \cdot \frac{\partial}{\partial\sigma_{||}}\Sigma\right)^2 + \left(\Delta\sigma_{\perp} \cdot \frac{\partial}{\partial\sigma_{\perp}}\Sigma\right)^2} \tag{5.27}$$

Where $\Delta\sigma_{||}$ and $\Delta\sigma_{\perp}$ are the respective errors in the parallel and perpendicular cross sections, and $\frac{\partial}{\partial\sigma_{||}}\Sigma$ is the partial derivative of the photon asymmetry with respect to $\sigma_{||}$ and similarly for $\sigma_{\perp}$.

5.7.2 Systematic Errors

The systematic uncertainties are more complicated than the statistical ones and as such are more difficult to calculate. They arise from uncertainties in the calibration procedure and there is no simple formula to evaluate them, unlike the statistical errors. The sources of systematic error and their estimated sizes are discussed in turn below:

- **Tagging Efficiency:** The tagging efficiency was measured at frequent intervals during the running of the experiment and was found to be stable. The efficiency of each focal plane element was obtained with an uncertainty of about 3%.

- **Pion Detection Efficiency:** The calibration data which was used to determine the pion detection efficiency only comprised a few hours of data taking. As a consequence of the limited amount of available data, the detection efficiency has an error of around 5%. This error is magnified by the fact that pions may decay in flight before reaching PiP, and negative pions may be misidentified as positive pions. While demanding consistent signals between the ΔE and PiP reduces the former and demanding the correct energy deposition in each layer the later, there is still an additional uncertainty of around 10% which is energy dependent.

- **Neutron Detection Efficiency:** The STANTON code was used to ascertain the neutron detection efficiency. The authors, [Cec79], quote an uncertainty of 5%.

- **Target Density:** The target density, n_{target}, was determined from a knowledge of the volume of Helium required to fill the cryotarget. This was kept constant by means of a resevoir and was refilled on average every 12 hours. The uncertainty in the target density is thought to be under 1%.

- **Random Contamination:** There still exists the presence of random events contaminating the data and these contribute an uncertainty to the measurement. Events may be falsely identified or discarded due to a random hit in

any of the detectors. These are thought to introduce an error of approximately 5 %.

- **Position and Angular Uncertainties:** The position calibrations of PiP and TOF both carry systematic errors which lead to errors in the calculated angles of the particles and consequently in the size of the solid angle element. This uncertainty is thought to be approximately 6%.

Because the data was normalised to the previously well known Hydrogen cross sections, the overall uncertainties were much reduced. This normalisation overcomes many of the systematic errors listed above. The normalistation factor used was 1.16. This was obtained by comparing the CH_2 data with the model of Blomqvist & Laget [Blo77]. This model has been used previously to give a good fit to Hydrogen cross sections. The data of Betourne *et al.*, [Bet68], which agrees with the B-L model was quoted with systematic errors of 4%. However as the normalisation was performed on a limited amount of calibration data, the statistical error in the normalisation factor was found to be 10%. This gives an overall uncertainty in the normalisation of 12%.

The value of this error has been obtained by use of the Hydrogen cross section data, the question remains as to whether this is applicable for nuclear reactions and in particular the ^{4}He$(\gamma, \pi^+$n) reaction. Of the systematic errors listed previously most are unchanged for the case of a nuclear target. However unlike the well defined kinematics of the Hydrogen reaction, the reaction on a nucleus mean the neutron solid angle is not automatically defined by the pion solid angle so there is an additional uncertainty from this. This depends on the uncertainty in the TOF azimuthal angle calibration, which is estimated to be around 5%. Also the pions decaying in flight may have been rejected in the Hydrogen case due to inconsistent energy measurements from that required by the two-body kinematics routine. However such constraints no longer apply in the nuclear case and therefore a further error is introduced. This asociated uncertainty is estimated to be about 7%. The effect of these two uncertainties leads to a combined systematic error for the Helium cross section data of 15%.

In the case of the photon asymmetry measurements the systematic errors are much reduced due to the fact that the photon asymmetry is a ratio of cross sections. There are however new systematic errors introduced.

- **Degree of Polarisation:** There is an associated systematic uncertainty in the calculation of the degree of polarisation. This is estimated to contribute around 10% to the systematic error of the photon asymmetry.

- **Misaligned Diamond Crystal:** It is possible that if the initial position of the diamond is inaccurately known that the alignment of the diamond crystal could be erroneous leading to a different degree of polarisation than that predicted by the simulation. However the prealignment procedure is thought to be extremely precise in determining the initial position of the crystal so this systematic error should be under 1%.

It is thus thought that the systematic error in the photon asymmetry is around 10%. This is less than the systematic error quoted for the cross sections and is one of the reasons that make photon asymmetries a good measurement to make.

Chapter 6

Results and Discussion

6.1 Introduction

This present chapter will show the experimental results presented alongside theoretical predictions from Louis Wright [Wri98]. The cross sections are presented in the form of double and triple differential cross sections, while the asymmetries presented were obtained only from the double differential cross sections, due to a lack of statistics. The cross sections are shown at four separate photon energy ranges, while the asymmetries were obtained for two separate photon energy ranges.

6.2 Comparison of Data with PWIA Predictions

The full DWIA model of Li, Wright and Benhold, [Li93], which was discussed in chapter Two, involves several ingredients. These include an elementary production operator, bound state wavefunctions, and optical model potentials to describe the final state interactions of the produced particles. Unfortunately in the case of the ^{4}He$(\gamma, \pi^+$n) reaction, the optical potential method for treating final state interactions is not applicable due to the fact that the residual nucleus is too small to be described in terms of uniform nuclear matter. However an estimation of the magnitude of the final state interactions was obtained by determining the strength of the FSI in the ^{12}C$(\gamma, \pi^+$n) reaction, which can be modelled by optical

potentials, and then assuming that the FSI are proportional to the size of the nuclei involved this was then scaled for the reaction on ^{4}He, i.e.:-

$$^4He(DWIA) =^4 He(PWIA) \times \frac{^{12}C(DWIA)}{^{12}C(PWIA)} \times \frac{\exp(-r_C)}{\exp(-r_{He})} \qquad (6.1)$$

Where ^{4}He(DWIA), etc. refers to either the calculated DWIA or PWIA cross section on ^{4}He or ^{12}C respectively, while r_{He} and r_C refers to the radii of the respective nuclei. The exponential is due to the fact that the absorption of particles in nuclear matter falls exponentially with decreasing radii. A separate correction factor was calculated for the four different photon energies used.

This gave an indication of the magnitude of the FSI in the ^{4}He$(\gamma, \pi^+$n) reaction and it was then possible to perform an FSI correction to the calculated PWIA cross sections. However in the case of the photon asymmetries, because this is a ratio of cross sections, the final state interactions effectively are cancelled and as just an accurate comparison can be made with a PWIA calculation as that which can be made with a DWIA one.

The PWIA calculations employ the full Blomqvist-Laget pion photoproduction operator and use harmonic oscillator wave functions for the bound nucleons. A spectroscopic factor, defined as the overlap between the initial nucleus with a nucleon removed and the final nuclear state, of 0.8 was also used, [Die90].

The code made predictions of the triple differential cross section results which were then integrated over the experimental pion energy ranges to give double differential cross sections. The double differential cross section results and PWIA calculations with and without FSI corrections are shown in figures 6.1 to 6.8. The error bars show the statistical uncertainty of each data point. The systematic errors have been discussed earlier and were shown to be approximately 15%. The points shown are where the TOF bars give 100% geometrical detection efficiency, i.e. the missing points correspond to regions in which there are gaps in the TOF array. The triple differential cross sections are shown in figures 6.9 to 6.12. Two pion angles were selected, 67.5 and 112.5^o, with the neutron angle chosen such that it was conjugate with the pion angle. The chosen neutron angles were 34 and 15^o so as to give maximal statistics. The size of the statistical errors becomes large at the higher photon energies, but are quite reasonable at the lower energies.

The photon asymmetries are calculated from the double differential cross sections only and are again compared with PWIA calculations. These are shown in figures 6.13 to 6.16.

6.3 Discussion

From studying the double and triple differential cross sections it is observed that the data lie below the PWIA calculations as would be expected due to FSI. The FSI corrected calculations also appear to overpredict the data, except however at the backward pion angles where a reasonable agreement can be observed. It would however be fair to say that the PWIA calculations predict the actual shapes of the cross sections with reasonable accuracy. This is particularly true of the lower photon energy double differential cross sections and the backward pion angle triple differential cross sections, while there is a clear flattening of the data in the triple differential cross sections at higher photon energies and forward pion angles which is not shown up in the calculations.

Perhaps the main point of interest in the cross section data is the difference in the level of cross section between the forward pion angle data and the backward pion angle data. Though this phenomenon has been observed previously in the experiment of L.D. Pham *et al.* [Pha92], which was discussed previously in chapter 1, in which the $^{16}O(\gamma,\pi^-p)$ reaction at a photon energy of 360 MeV and at two pion angles, $\theta_\pi = 64^o$ and $\theta_\pi = 120^o$ was measured, there was no corresponding discrepancy found in the previous $^{12}C(\gamma,\pi^+n)$ experiments carried out by the Edinburgh group, [Mac95, Joh95].

Possible explanations of the difference in magnitudes of the forward and backward pion angle cross sections include differences in the final state interactions at the different angles which is not picked up in our attempt at estimating the magnitude of these FSI. However a more interesting possibility was shown in [Li93] where a reduction of the in-medium Δ mass reduces the forward pion angle cross section much more markedly than it affects the backward pion angle cross section. In particular, Li, Wright and Benhold show that on ^{12}C for a reduction in the Δ mass of 3%, a reduction of 40% is achieved in the forward pion angle

calculations while a reduction of only 25% is seen in the backward pion angle calculations. It is also of interest to note that the LEGS asymmetry data of K. Hicks *et al.*, [Hic97], taken on ^{16}O show that a calculation in which the Δ mass is reduced by 5% produces a better fit to their data than a calculation with the normal Δ mass.

The photon asymmetry data compares much more favourably with the PWIA calculations. Not only is the overall trend of the data accurately predicted but the overall magnitude of the asymmetries is also fairly well reproduced. This is as expected due to the fact that the final state interactions cancel out due to the asymmetry being a ratio. The data is reproduced by the calculations more faithfully at the lower photon energy than at the higher photon energy, where the data in particular falls away from the calculation at the backward pion angle. This feature also shows up in the LEGS asymmetry data where there is good agreement between data and theory at forward pion angles but data and calculations diverge at the backward pion angles.

The results provide a valuable first investigation of the asymmetries. However to obtain definitive information on medium effects it would be necessary to have run for a substantially longer period to reduce the error bars as changes in the Δ mass show up only as small shifts in the calculated cross sections.

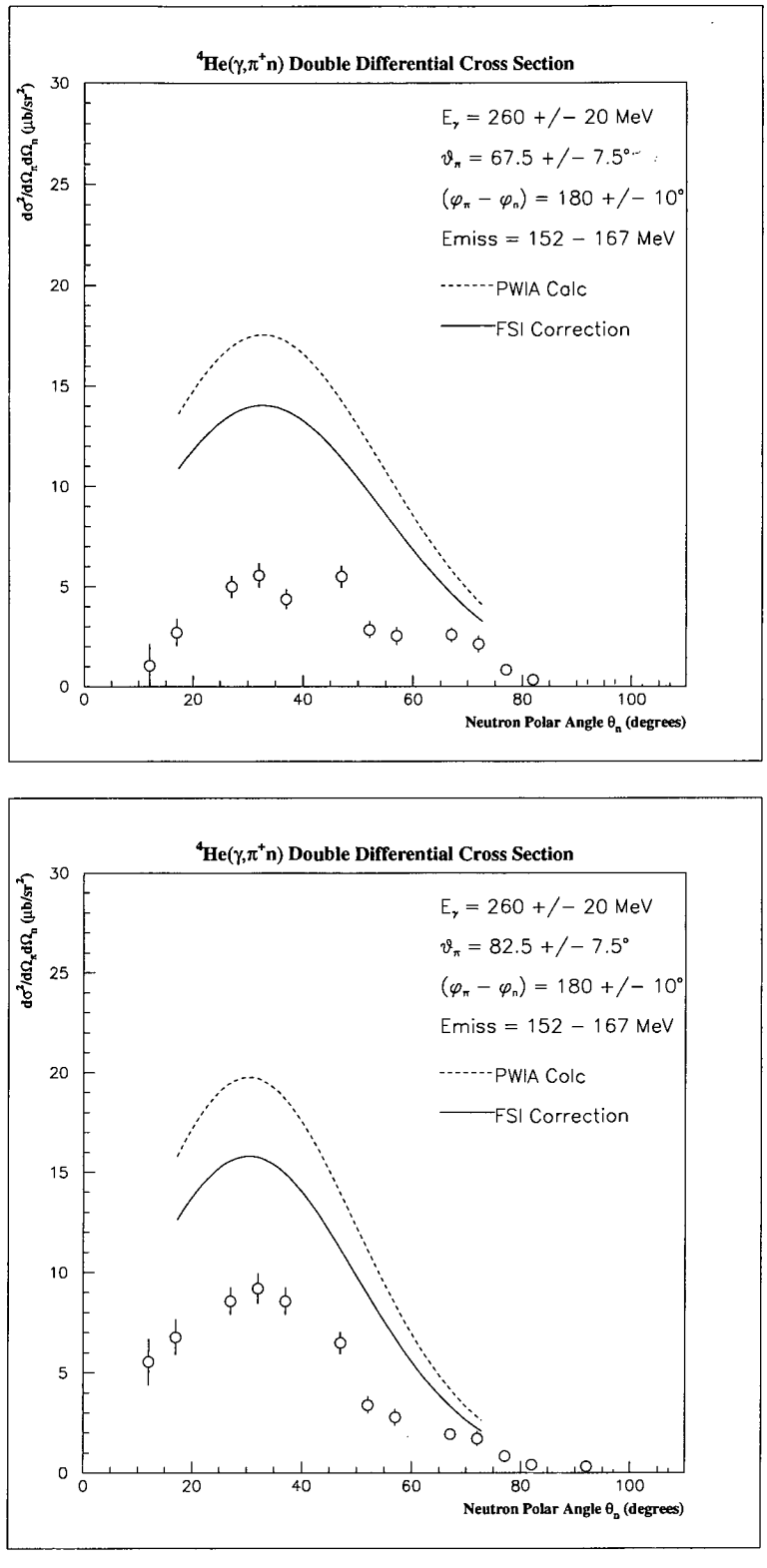

Figure 6.1: *Double Differential Cross Section Data.*

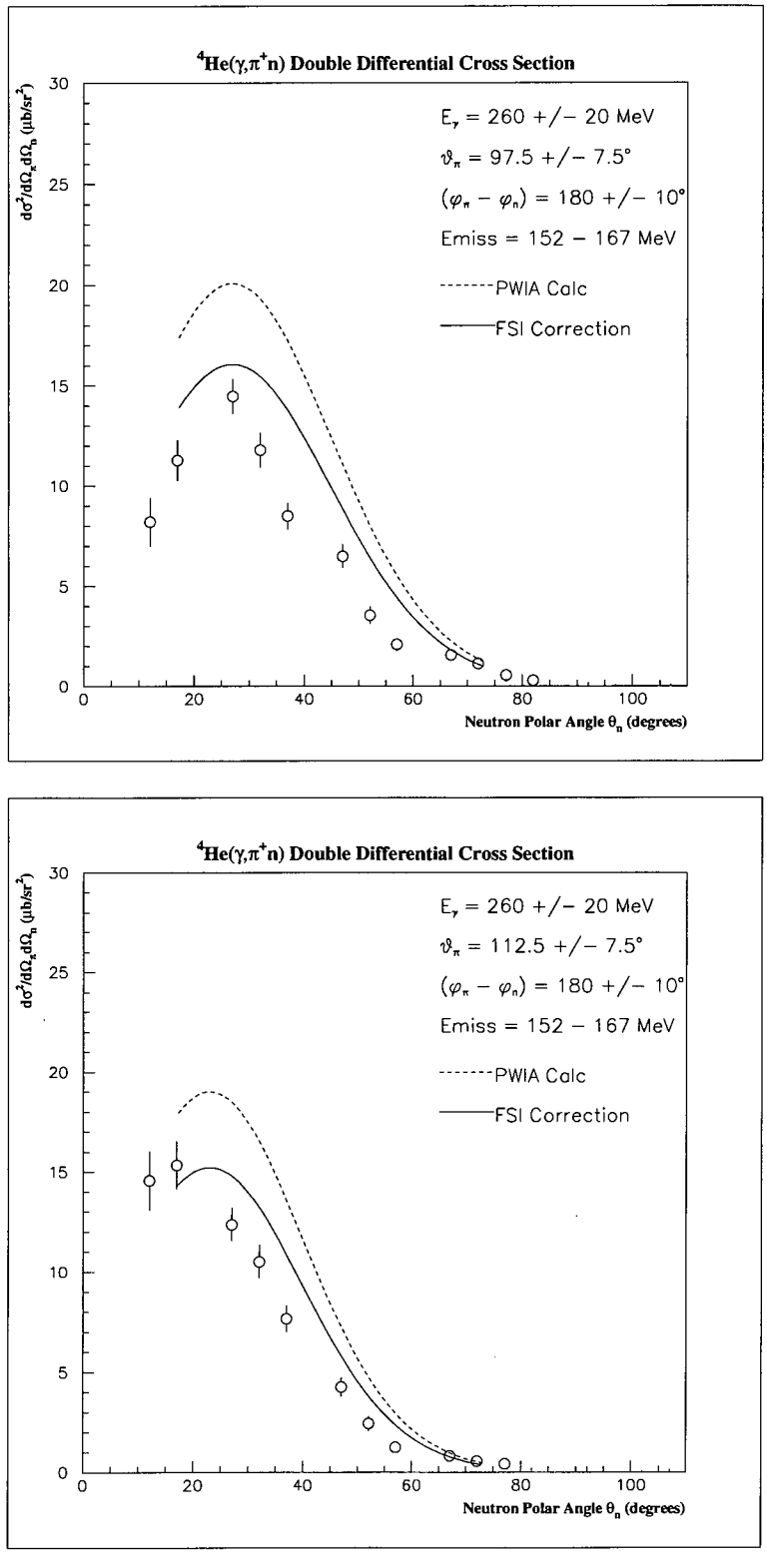

Figure 6.2: *Double Differential Cross Section Data.*

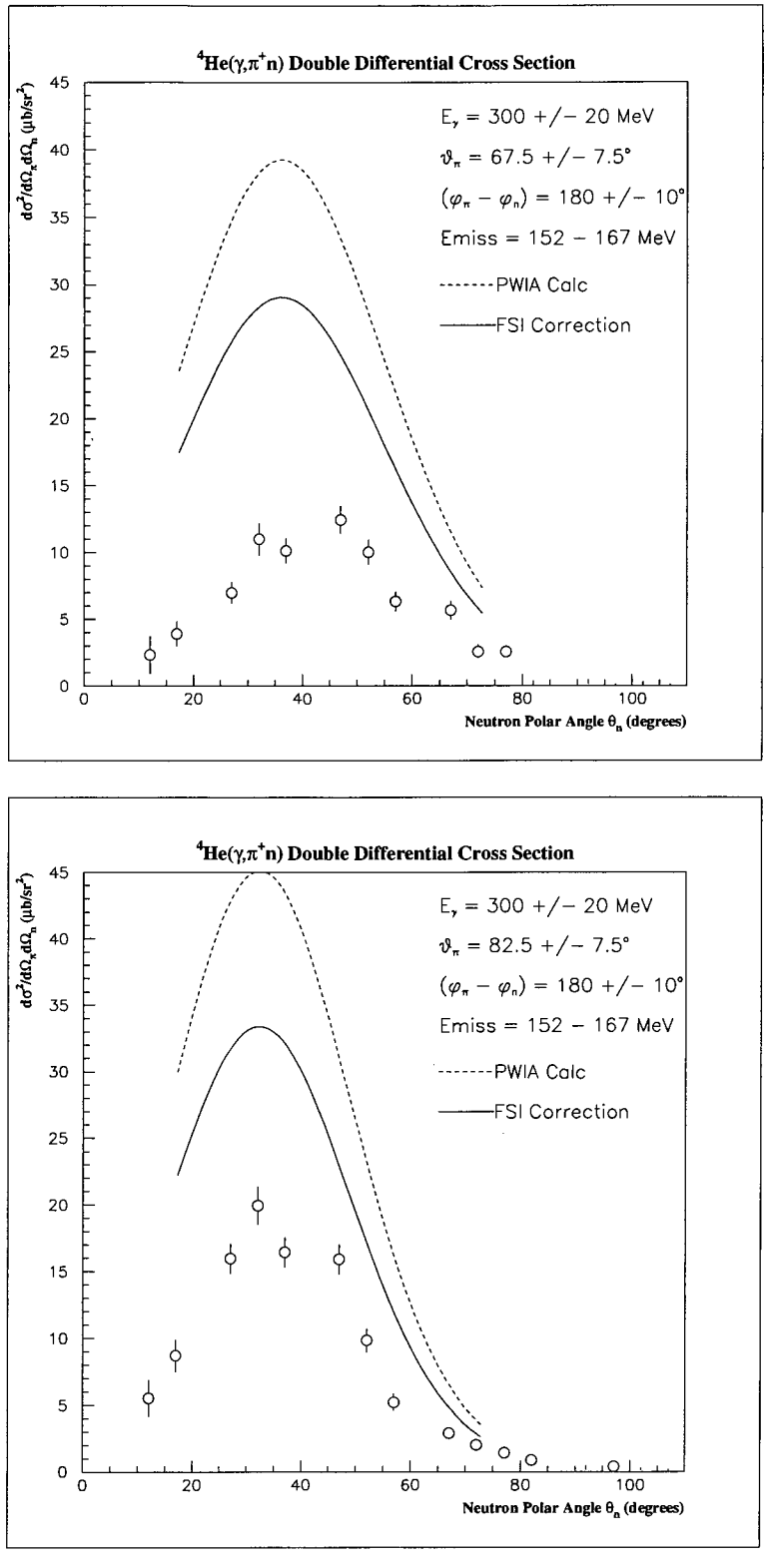

Figure 6.3: *Double Differential Cross Section Data.*

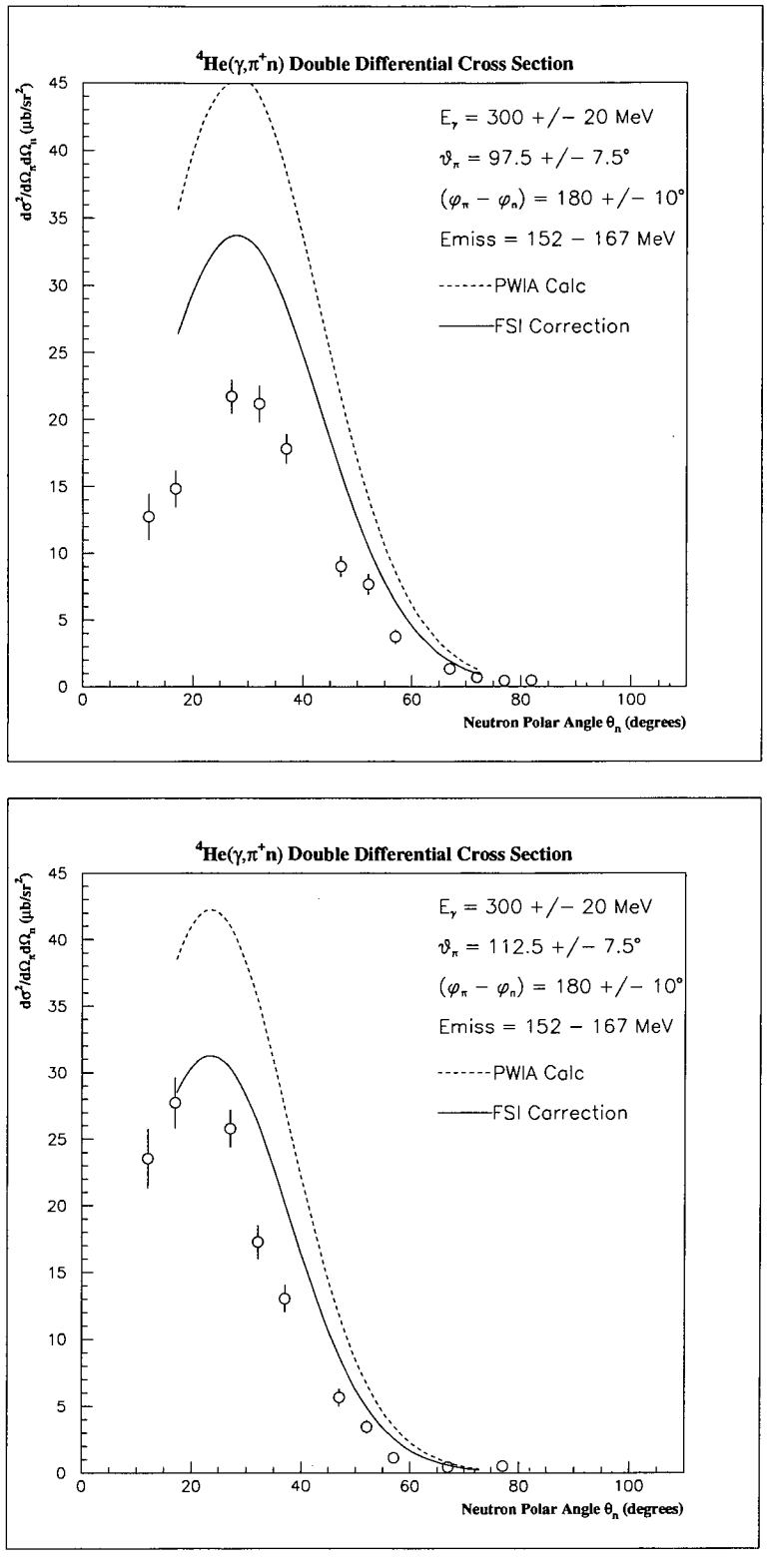

Figure 6.4: *Double Differential Cross Section Data.*

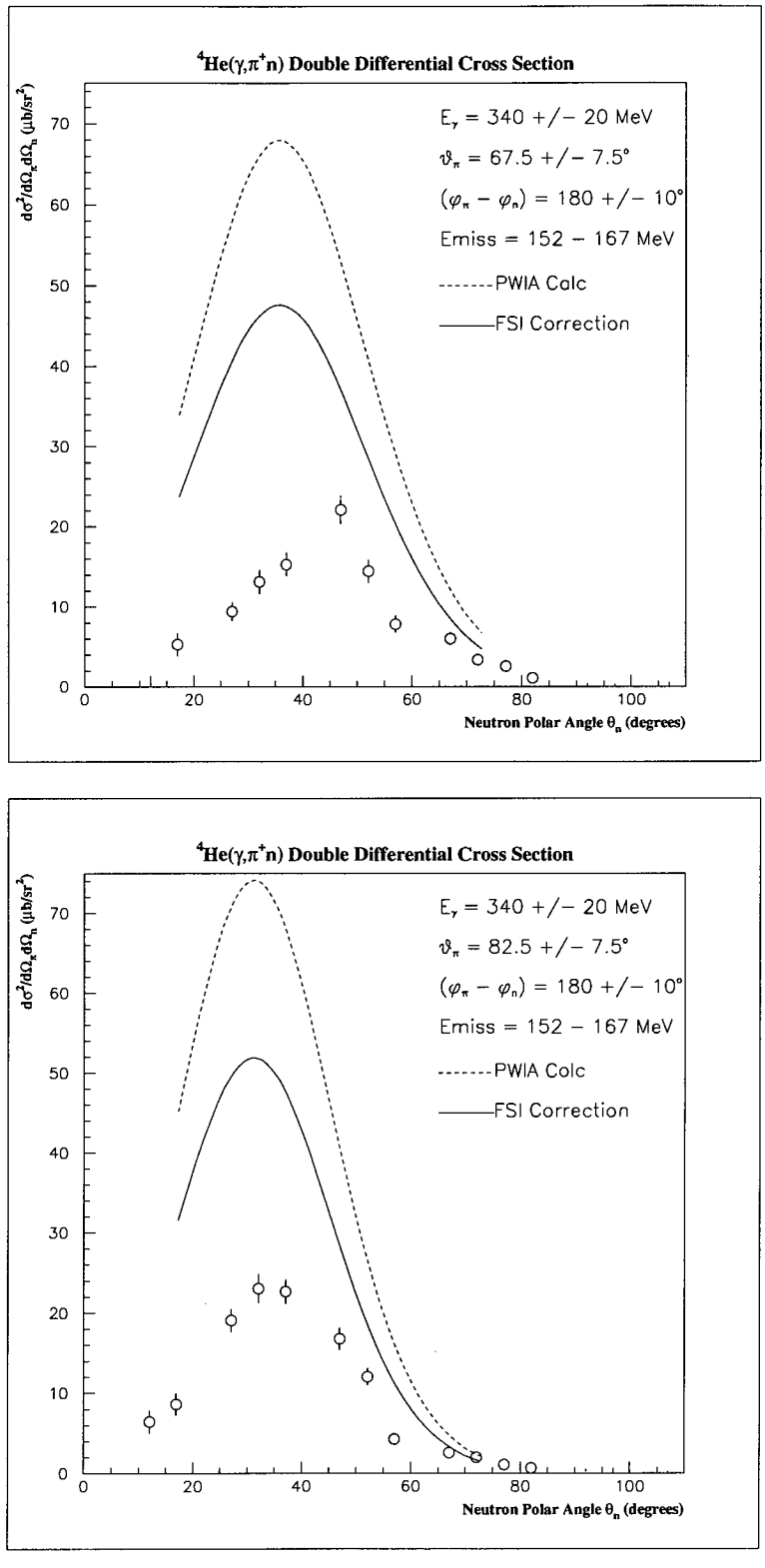

Figure 6.5: *Double Differential Cross Section Data.*

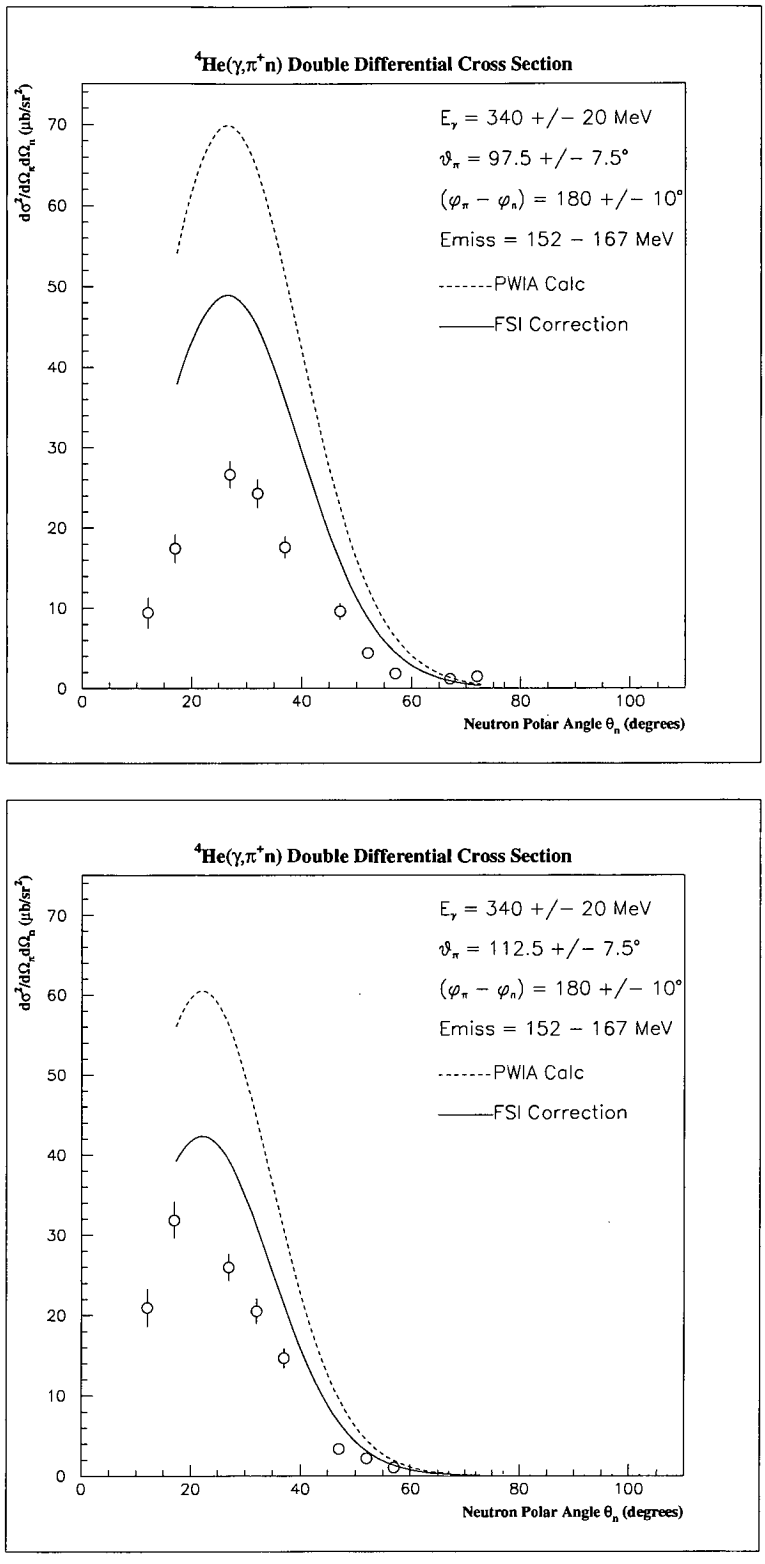

Figure 6.6: *Double Differential Cross Section Data.*

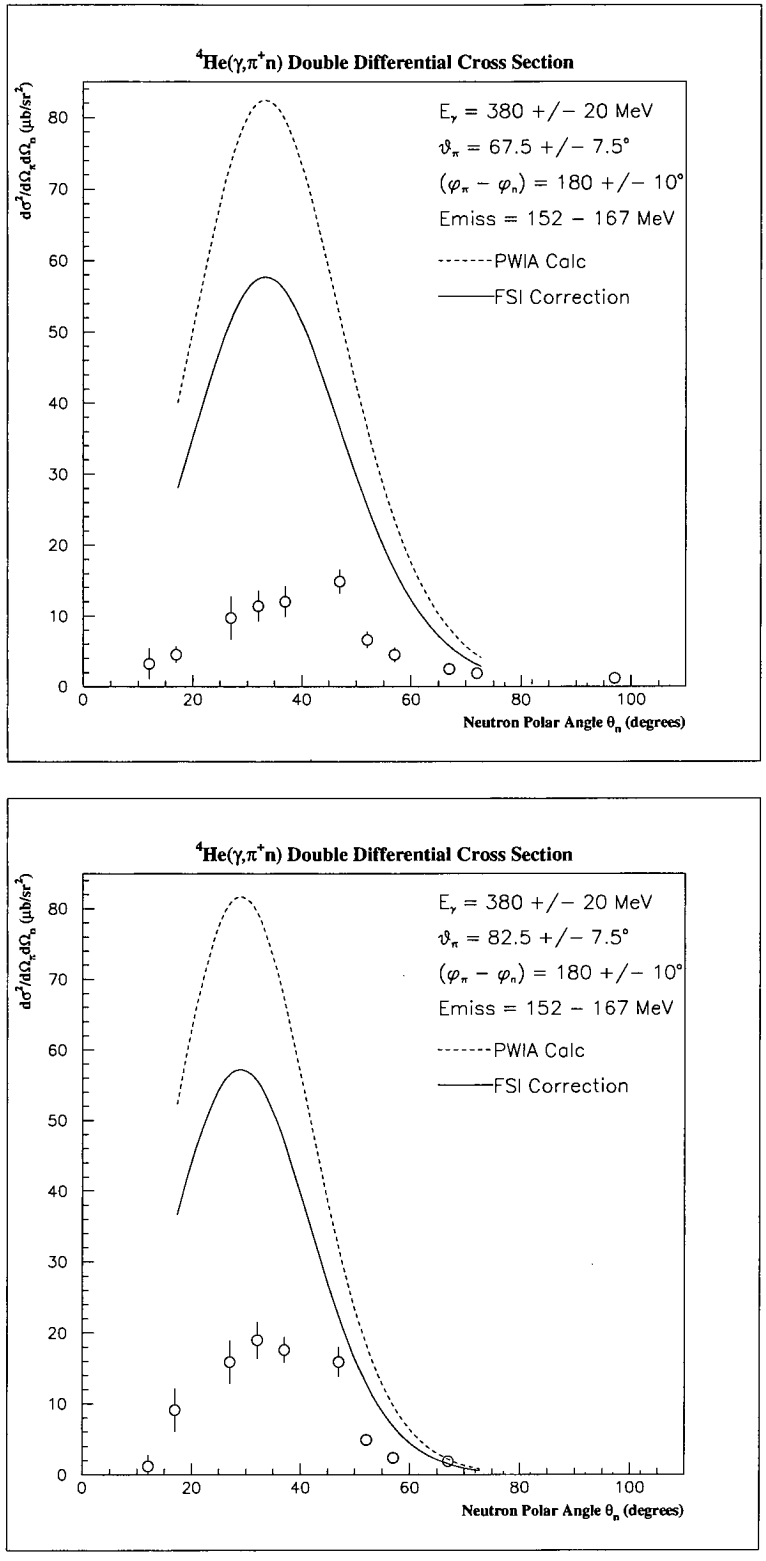

Figure 6.7: *Double Differential Cross Section Data.*

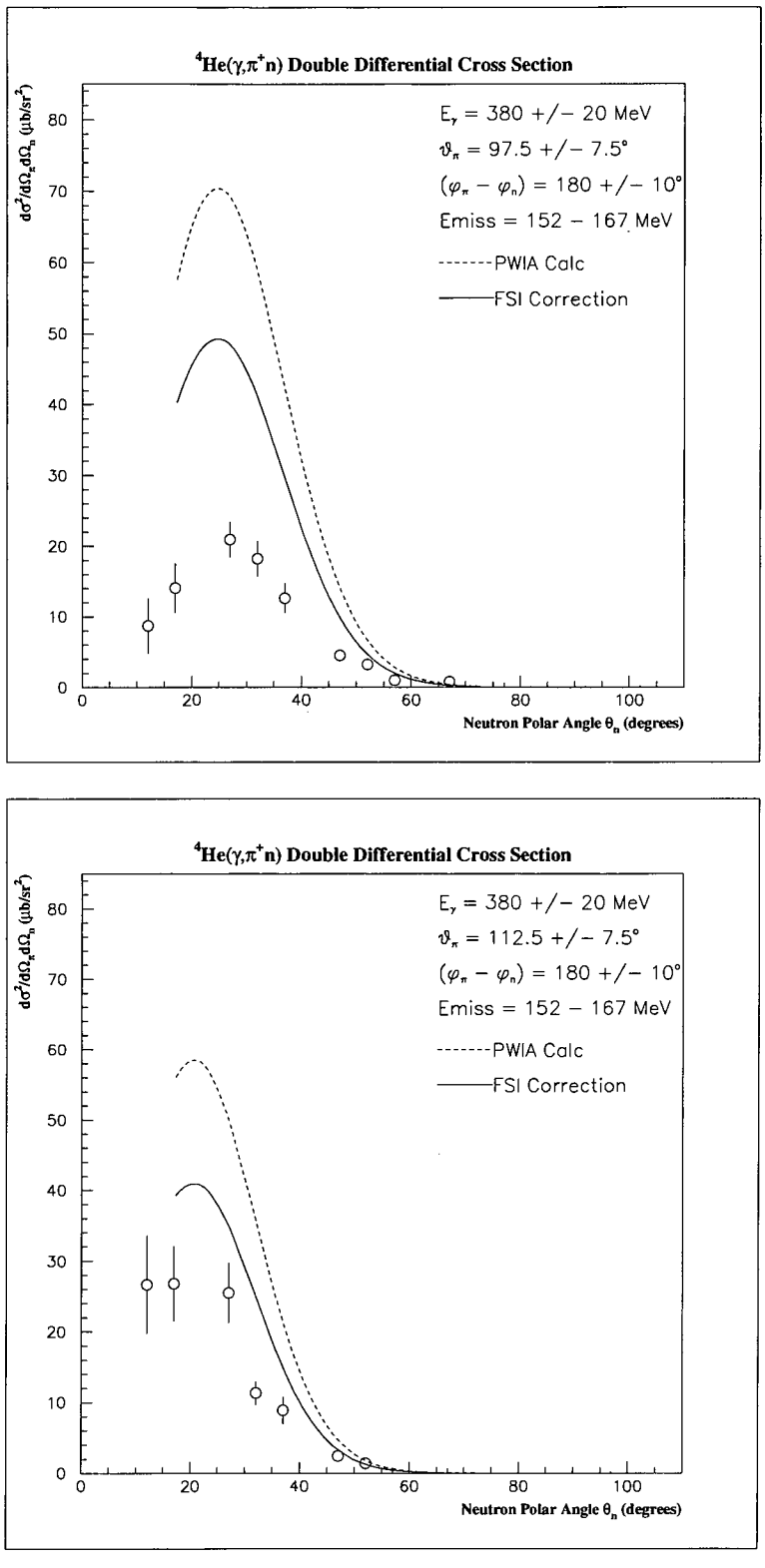

Figure 6.8: *Double Differential Cross Section Data.*

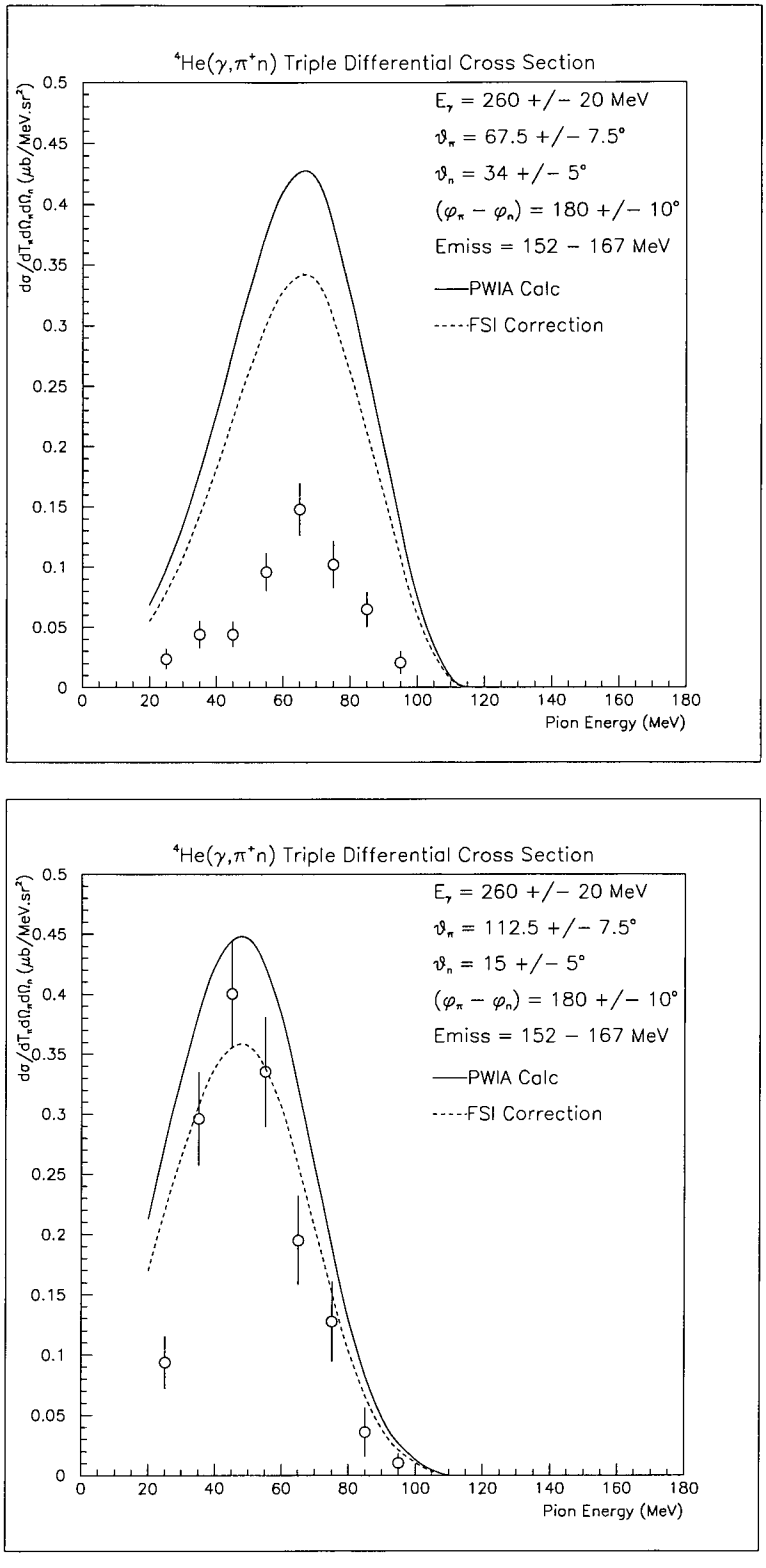

Figure 6.9: *Triple Differential Cross Section Data.*

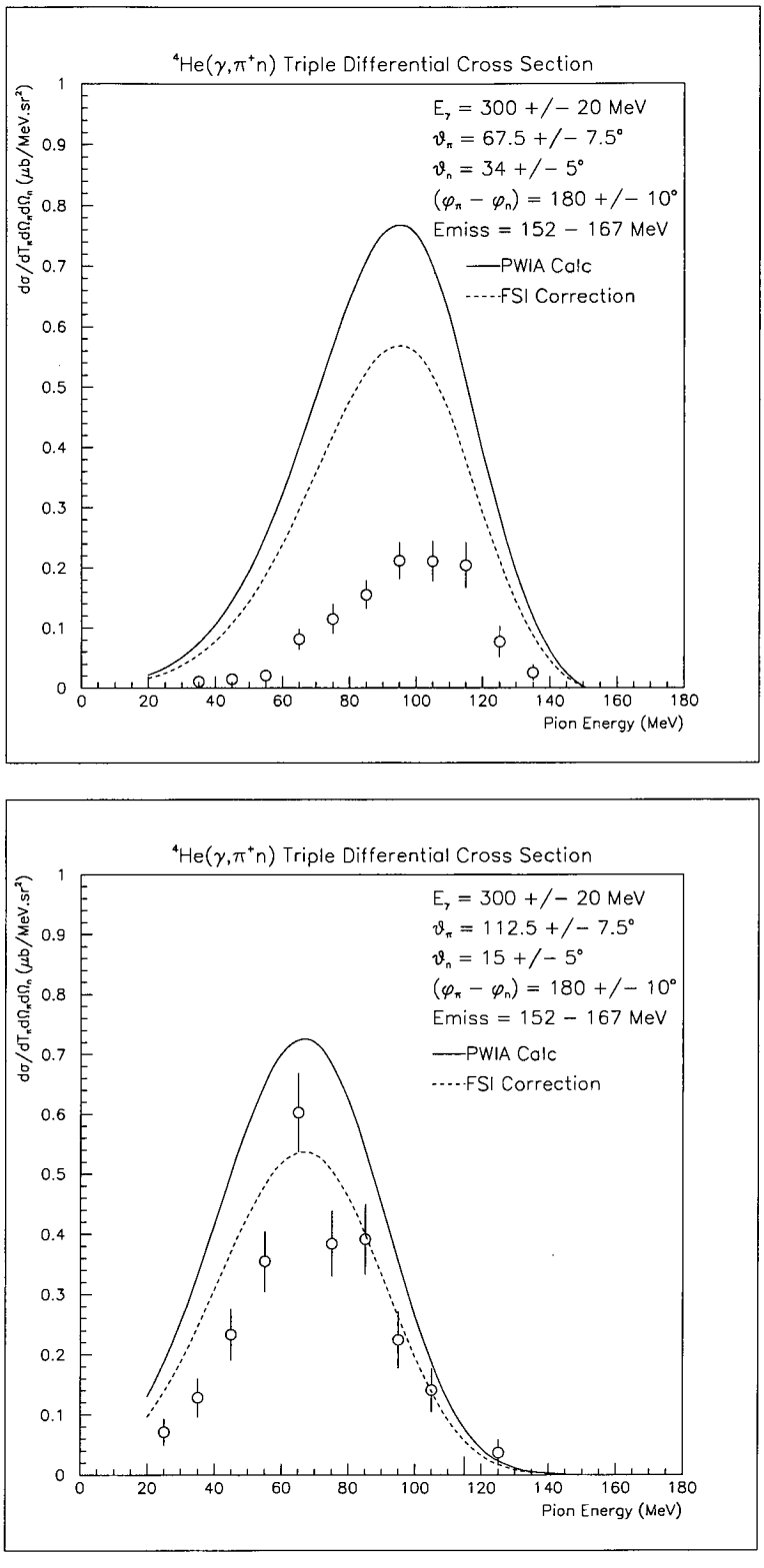

Figure 6.10: *Triple Differential Cross Section Data.*

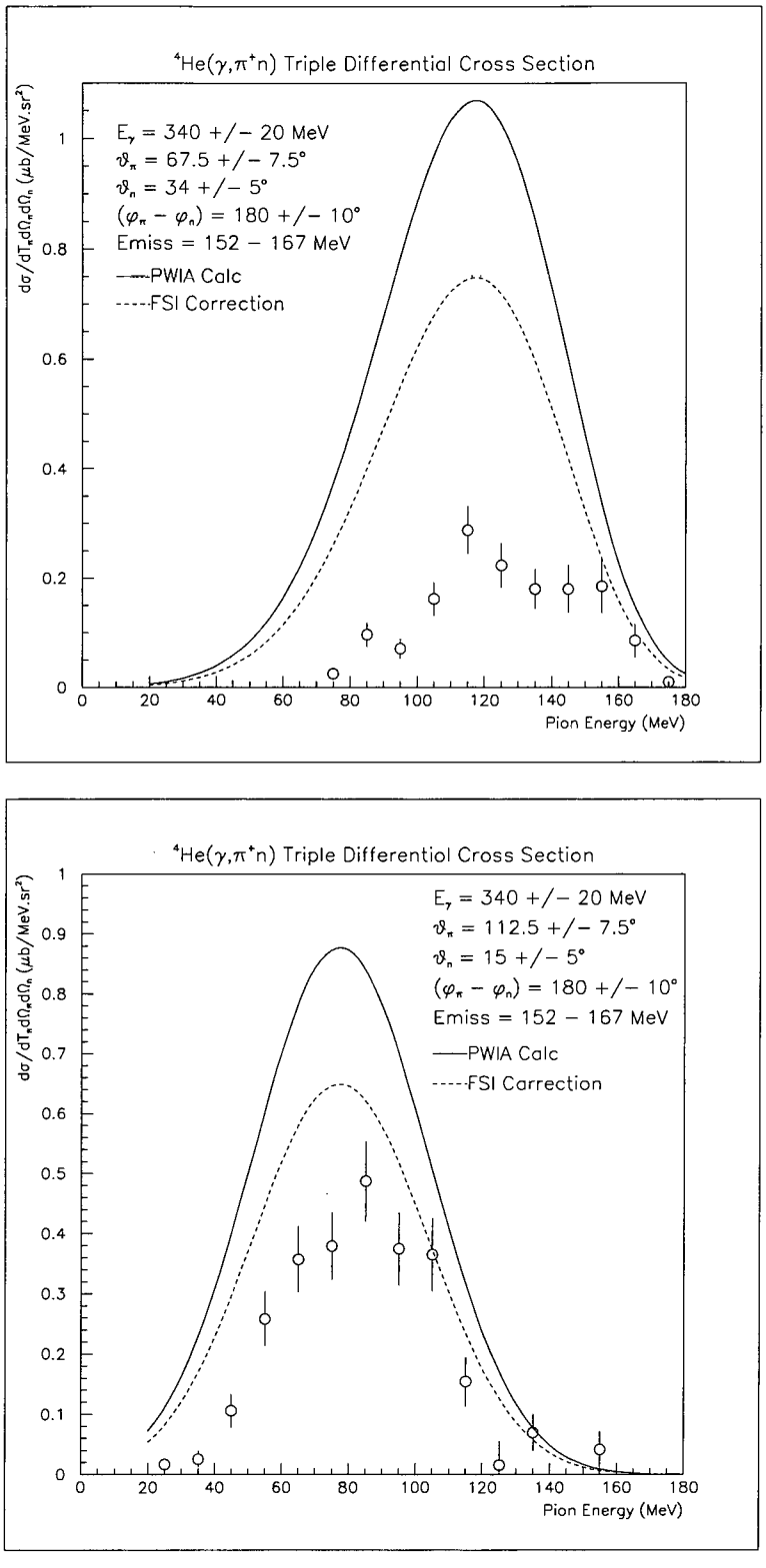

Figure 6.11: *Triple Differential Cross Section Data.*

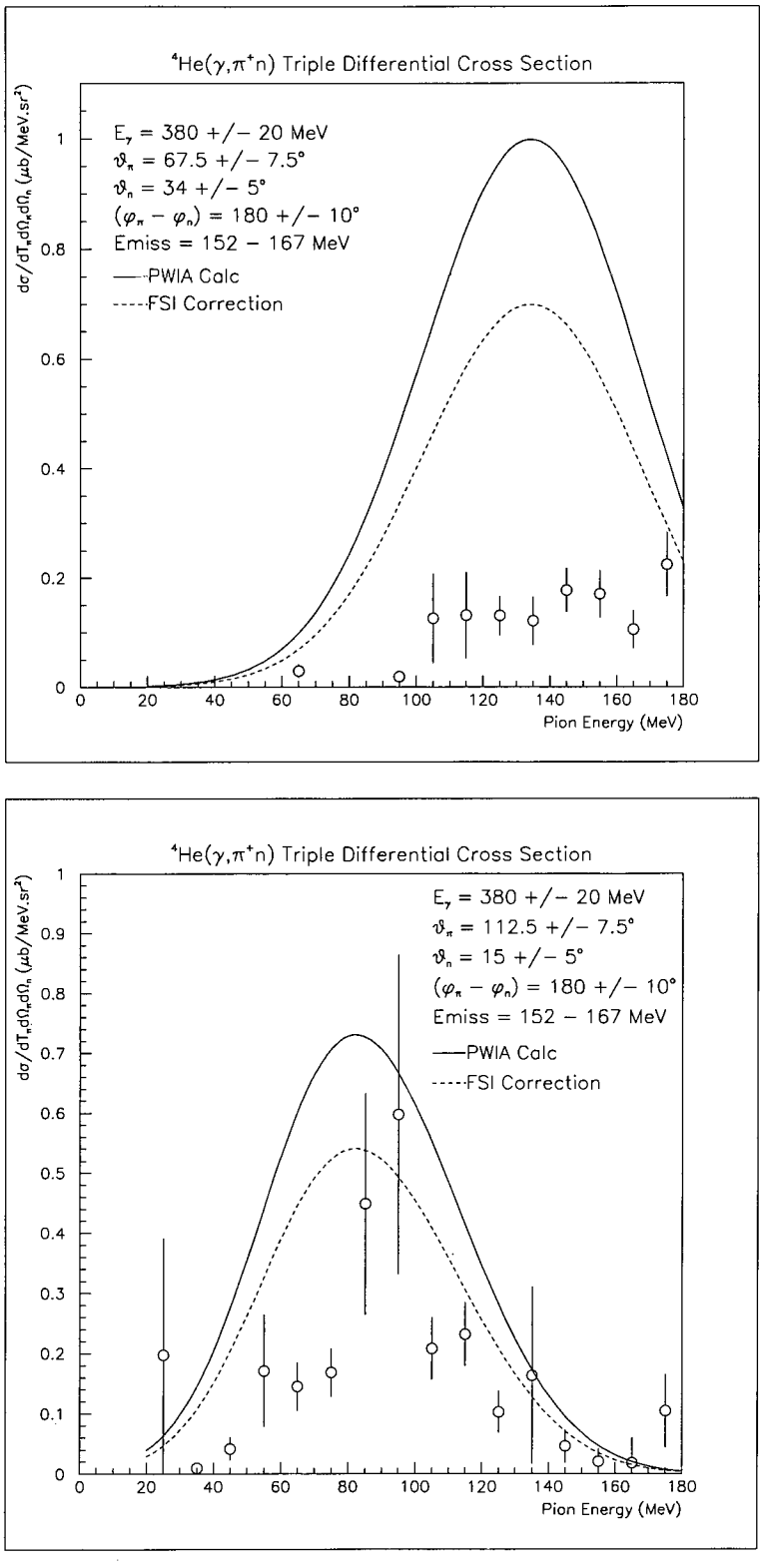

Figure 6.12: *Triple Differential Cross Section Data.*

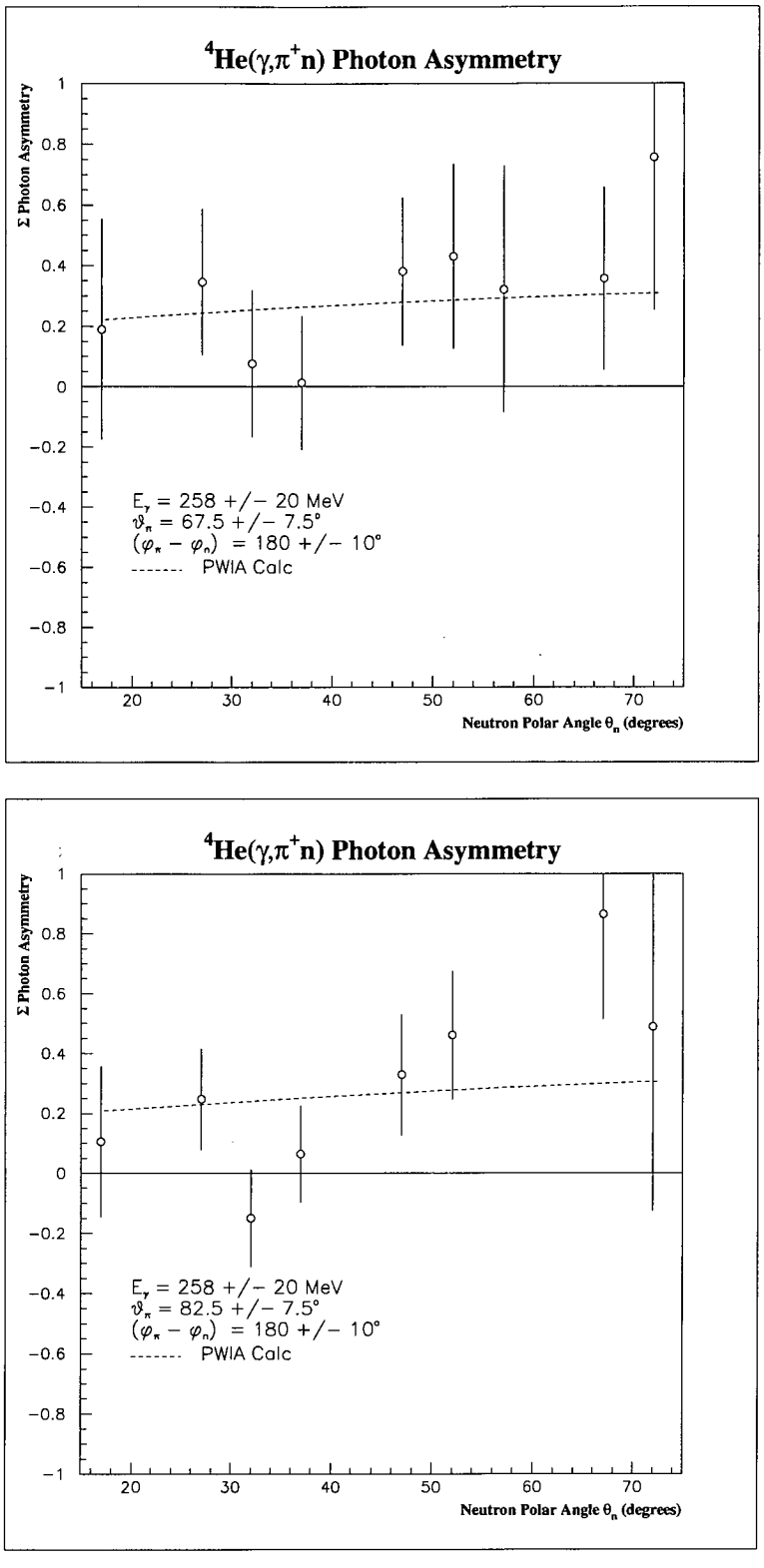

Figure 6.13: *Photon Asymmetry Data.*

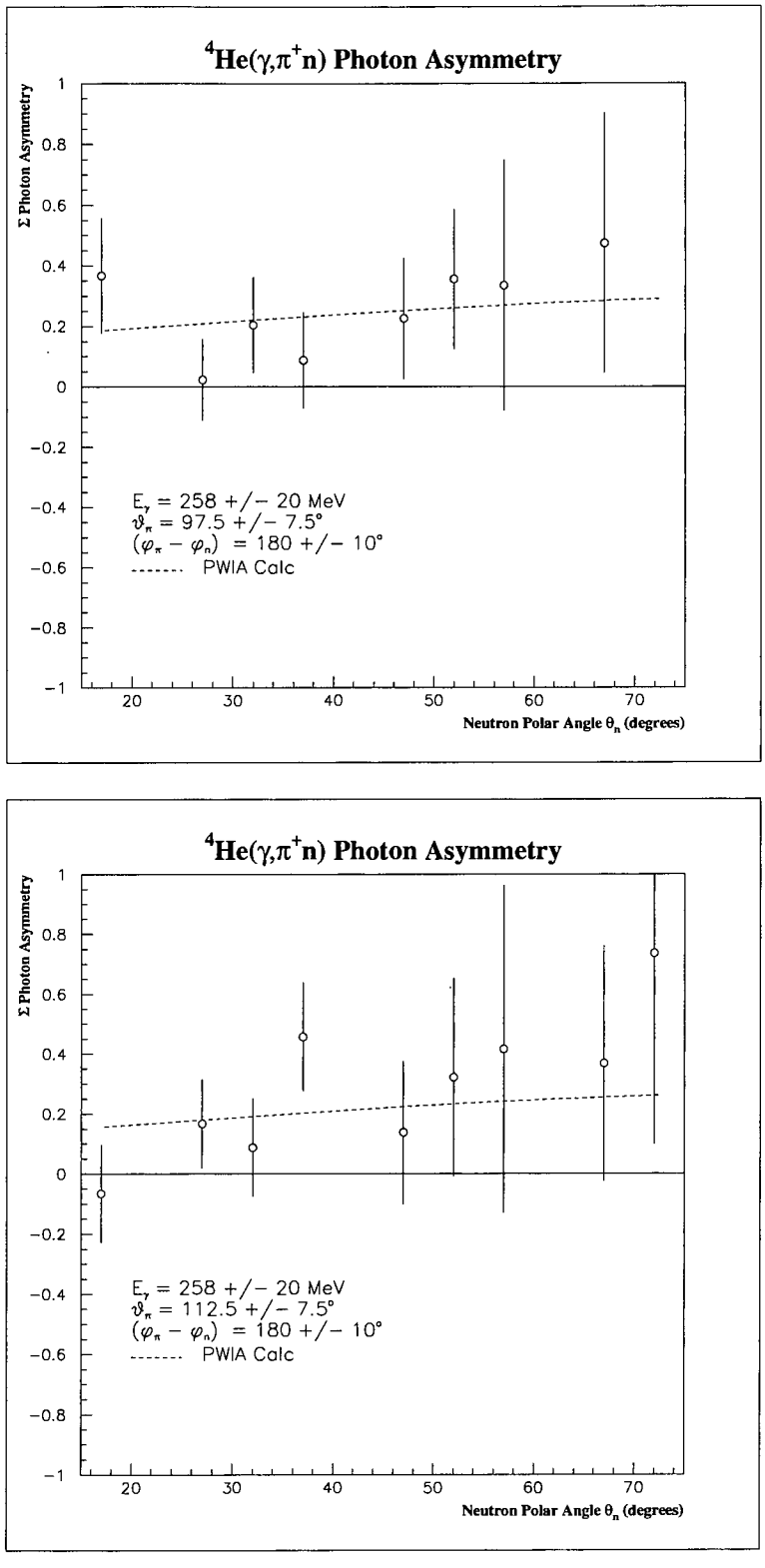

Figure 6.14: *Photon Asymmetry Data.*

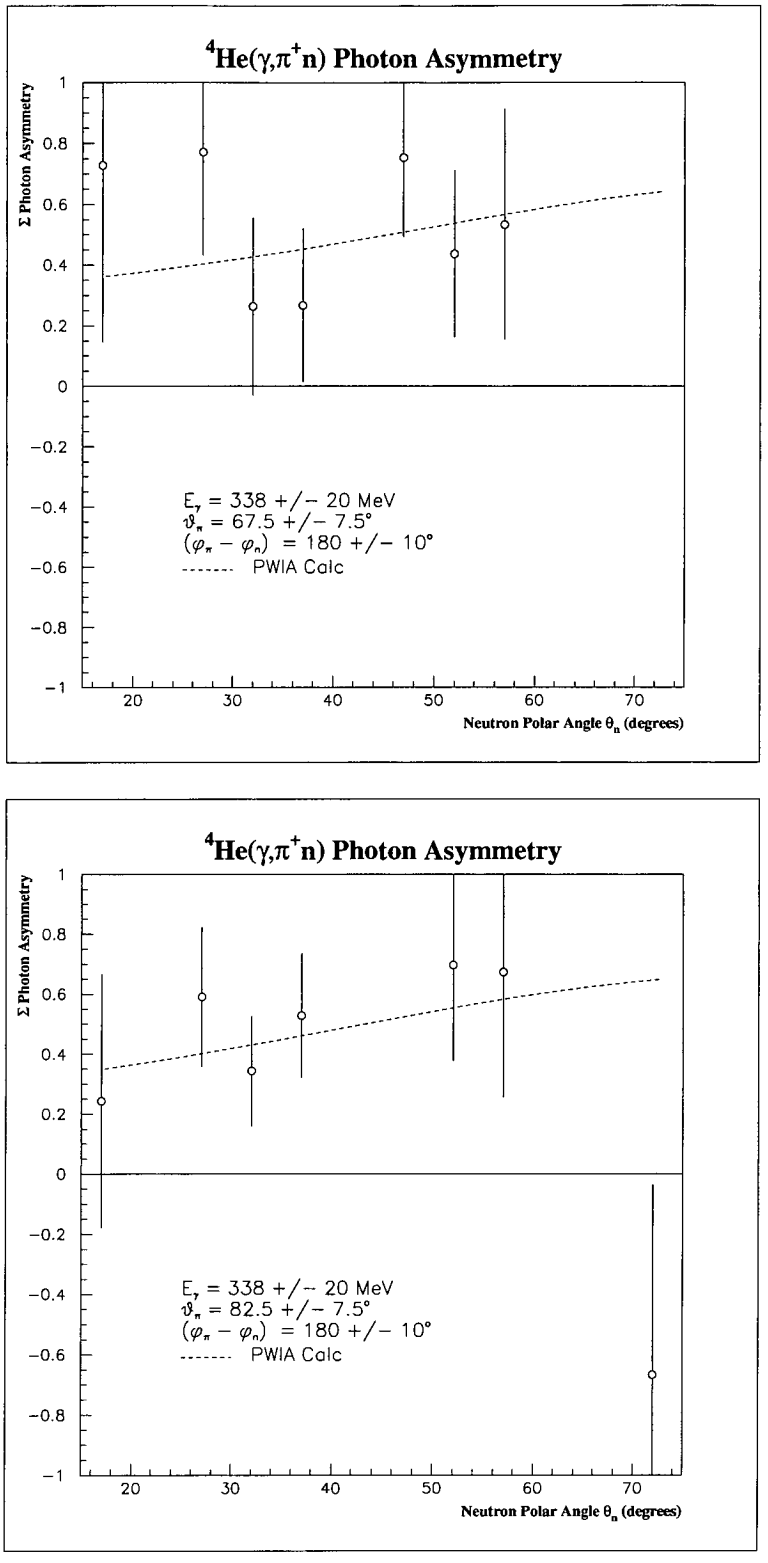

Figure 6.15: *Photon Asymmetry Data.*

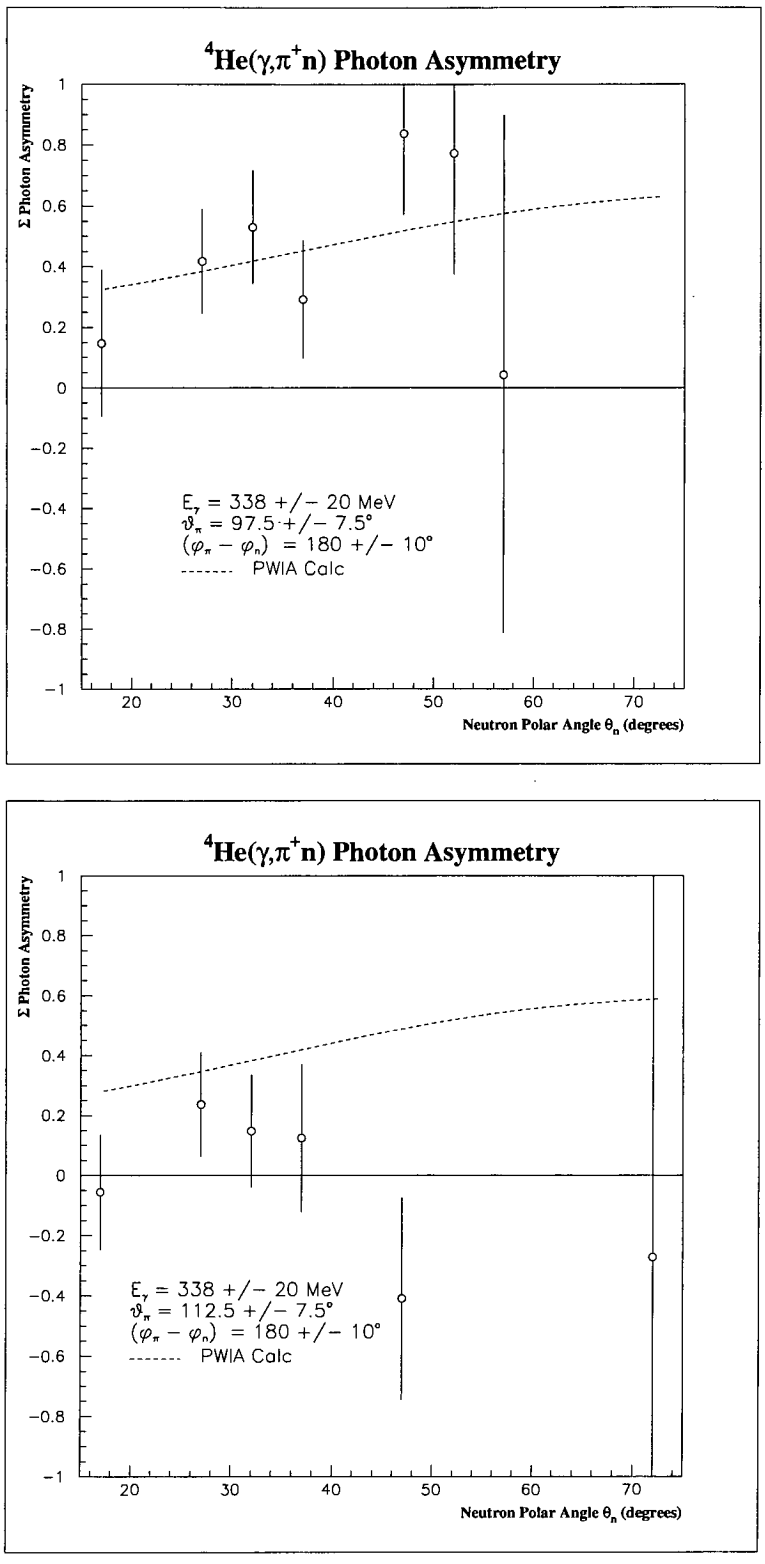

Figure 6.16: *Photon Asymmetry Data.*

Chapter 7

Conclusions

There are essentially two main categories of conclusions that can be drawn from the work presented in this thesis; those relating to the cross sections and those relating to the photon asymmetries. In making these conclusions certain possible experimental improvements are suggested.

7.1 Cross Sections

The cross section measurements significantly increase the amount of available data. This new data set is particularly valuable in that it provides a comprehensive set of measurements of nuclear pion photoproduction on an extremely interesting and important nucleus, namely Helium-4. The differential cross sections were compared with PWIA predictions with and without corrections for FSI. Although these were able to correctly predict the shape of the pion kinetic energy distributions and the angular distributions, the experimental cross sections fell on average significantly below the theoretical predictions. Of particular note was the comparitive differences in strength of the forward and backward pion angle cross sections, which although did not show up in the previous $^{12}C(\gamma,\pi^+n)$ Edinburgh work did appear in the work of [Pha92]. This may indicate the possiblility of in-medium effects, in particular a reduction of the in-medium Δ mass produces changes to the calculated cross sections that are consistent with the data. However for this to be investigated further the FSI would need to be more fully understood.

The cross sections thus provide a stern test and hopefully fresh impetus to pion photoproduction theorists. In particular it shows the need for the development of a more sophisticated theory applicable to few-body nuclei.

7.2 Photon Asymmetries

The major innovation of this work was the use of a polarised photon beam to determine photon asymmetries. This was the first time the PiPTOF system has been used in the measurement of a photon asymmetry and is in fact one of the first measurements anywhere of a nuclear pion photoproduction photon asymmetry. A photon asymmetry measurement, due to the fact that it is a ratio, is free from uncertainties caused by final state interactions and as such is a sensitive test of the pion photoproduction process.

Although reasonable agreement was found between the PWIA calculations and the data, clearly the size of the statistical errors make a detailed comparison impossible. In retrospect this could have been avoided if a less ambitious experimental programme had been undertaken so more beam time could have been expended on perhaps making a photon asymmetry measurement at just one energy. The statistical errors are also not helped by the fact that the polarisation of the beam has to be changed to get both horizontally and vertically polarised photons. A definite improvement would be the use of a detector that covered the whole azimuthal range as this would negate the need to change the beam polarisation.

Certainly the fact the asymmetry measurements are insensitive to FSI suggests that it would be worthwhile to perform further asymmetry measurements, with the proviso that suitable statistics are gained. A particularly good reaction to study would be the photoproduction of neutral pions which proceeds almost entirely through the Δ resonance term and thus modifications of the Δ should show up more strongly.

This work provides an important contribution to the existing data set in the field and it is hoped it will thus further our understanding of the processes involved in nuclear pion photoproduction.

Bibliography

[Ana90] P. S. Anan'in *et al.*, *Sov. J. Nucl. Phys.* 52 (1990) 205

[Ann95] J.R.M Annand, I. Anthony, A. Sibhald, *ACQU Manual* Kelvin Lab Internal Report (1995)

[Ann93] J. R. M. Annand and B. Oussena, *NIM* A330 (1993) 220

[Ann96] J. R. M. Annand *et al.*, *NIM* A368 (1996) 385

[Ant91] I. Anthony *et al*, *NIM* A301 (1991) 230

[Are82] J. Arends *et al.*, *Z. Phys. A* 305 (1982) 205

[Are91] J. Arends *et al.*, *Nucl. Phys. A* 526 (1991) 479

[Bet34] H. Bethe and W. Heitler, *Proc. Roy. Soc. (London)* A146 (1934) 83.

[Bet68] C. Betourne *et al. Phys. Rev.* 172 (1968) 1342

[Ber68] F. A. Berends, *et al.*, *Nucl. Phys. B* 4 (1967) 1

[Bia94] N. Bianchi *et al.*, *Phys. Lett.* B325 (1968) 333

[Bjo64] J. D. Bjorken and S. D. Drell, *Relativistic Quantum Mechanics*, Wiley, (1964)

[Blo77] I. Blomqvist and J. M. Laget, *Nucl Phys. A* 280 (1977) 405

[Boe95] W. Boeglin, *The Mainz Microtron: A Status Report* Mainz Internal Report (1995)

[Bra91] D. Branford (Ed.), *Future Detectors for Photonuclear Experiments* (1991).

[Bru82] R, Brun, M. Hansroul and J. C. Lassalle, *GEANT User's Guide* DD/EE/82 CERN (1982)

[Byc73] E. Byckling and K. Kajantie, *Particle Kinematics*, Wiley, (1973)

[Car82] J. A. Carr *et al. Phys. Rev. C* 25 (1982) 952

[Car92a] R. Carrasco and E. Oset, *Nucl. Phys. A* 536 (1992) 445

[Car92b] R. Carrasco and E. Oset, *Nucl. Phys. A* 541 (1992) 585

[Car92c] R. Carrasco and E. Oset, *Phys. Rev. C* 45 (1992) 764

[Car94] R. Carrasco and E. Oset, *Nucl. Phys. A* 570 (1994) 701

[Cec79] R. A. Cecil *et al.*, *NIM* A161 (1979) 439

[Cha77] N. S. Chant and P. Roos, *Phys. Rev C* 15 (1977) 15

[Che57] G. F. Chew, *et al.*, *Phys. Rev.* 106 (1957) 1345

[Die90] A. E. L. Dieperink and P. K. A. de Witt Huberts *Ann. Rev. of Nucl. & Part. Science* 40 (1990) 239

[Gaa91] C. Gaarde, *Ann. Rev. Nucl. Part. Sci.* 41 (1991) 187

[Gar81] M. Gari and H. Hebach, *Physics Reports* 72 (1981) 1

[Gla79a] I. V. Glavanokov, *Sov. J. Nucl. Phys.* 29 (1979) 746

[Gla79b] I. V. Glavanokov, *Sov. J. Nucl. Phys.* 30 (1979) 465

[Gla89] I. V. Glavanokov, *Sov. J. Nucl. Phys.* 49 (1989) 58

[Gra98] P. Grabmayr *et al.*, *NIM* A402 (1998) 85

[Hal96] S. J. Hall *et al.*, *NIM* A368 (1996) 698

[Han97] O. Hanstein *et al.*, *Phys Lett. B* 399 (1997) 13

[Pec69] R. D. Peccei, *Phys. Rev.* 181 (1969) 1902

[Pha92] L. D. Pham *et al.*, *Phys. Rev. C* 46 (1992) 621

[Sat93] T. Sato and T. Takaki, *Nucl. Phys. A* 562 (1993)

[Sch82] P. Schwandt *et al.*, *Phys. Rev. C* 26 (1982) 55

[Sha74] A. Shalit & H. Feshbach *Theoretical Nuclear Physics Vol 1*, Wiley, (1974)

[Sin81] M. K. Singham and F. Tabakin, *Annals of Physics* 135 (1981) 71

[Van95] M. Vanderhaeghen *et al.*, *Nucl. Phys. A* 595 (1995) 219

[Wat54] K. Watson, *Phys. Rev.* 95 (1954) 228

[Wri98] L. E. Wright, *Private Communication.*

[Wun97] S. Wunderlicht and F. A. Natter *Simulation of Coherent Bremsstrahlung* Tübingen Internal Report (1997) 1/97

[Heh96] T. Hehl and S. Oberkirsch, *The Helium Cryotarget Manual*, Tübingen Internal Report (1996) 3/96

[Hic97] K. Hicks, *et al. Phys. Rev. C* 55 (1997) 31

[Joh95] D. Johnstone, *PhD Thesis*, University Of Edinburgh, (1995)

[Kis73] L. Kisslinger, W. Wang, *Phys. Rev. Lett.* 30 (1973) 1071

[Koc84] J. H. Koch, E. J. Moniz, N. Ohtsuka, *Annals of Physics* 154 (1984) 99

[Kra96] I. Krahn *PhD Thesis, Institut für Kernphysik*, Universität Mainz, (1996)

[Kra97] A. Kraus, *et al.*, *Phys. Rev. Lett.* 79 (1997) 3834

[Lag72] J. M. Laget, *Nucl. Phys. A* 194 (1972) 81

[Li93] X. Li, L. E. Wright and C. Benhold, *Phys. Rev. C* 48 (1993) 816

[Lo94] D. Lohmann *et al. NIMS* A343 (1994) 494

[Mac95] J. A. MacKenzie, *PhD Thesis*, University Of Edinburgh, (1995)

[Mac96a] J. A. MacKenzie *et al., Phys Rev C* 54 (1996) R6

[Mac96b] I. J. D. MacGregor *et al.*, *NIM* A382 (1996) 479

[Mer70] E. Merzbacher, *Quantum Mechanics*, Wiley, (1970)

[Nag91] A. Nagl, V. Devanathon, H. Überall, *Nuclear Pion Photoproduction* (1991)

[Noz90] S. Nozawa *et al.*, *Nucl. Phys. A* 513 (1990) 459

[Omn58] R. Omnès, *Nuovo Cim* 8 (1958) 316

[Ols74] M. G. Olsson, *Nucl. Phys. B* 78 (1974) 55

[Owe90] R. O. Owens, *NIMS A* 288 (1990) 574

[Paw95] Physics Analysis Workstation, *CERN Program Library entry Q121*, (1995)